CALIBRATED LOCALIZATION RELATIONSHIPS FOR ELASTIC POLYCRYSTALLINE AGGREGATES

A Dissertation
Presented to
The Academic Faculty

by

Yuksel C. Yabansu

In Partial Fulfillment
of the Requirements for the Degree
Doctor of Philosophy in the
George W. Woodruff School of Mechanical Engineering

Georgia Institute of Technology
May 2017

CALIBRATED LOCALIZATION RELATIONSHIPS FOR ELASTIC POLYCRYSTALLINE AGGREGATES

Approved by:

Prof. Surya R. Kalidindi, Advisor
George W. Woodruff School of Mechanical Engineering
Georgia Institute of Technology

Prof. Hamid Garmestani
School of Materials Science and Engineering
Georgia Institute of Technology

Prof. Antonia Antoniou
George W. Woodruff School of Mechanical Engineering
Georgia Institute of Technology

Prof. Richard W. Neu
George W. Woodruff School of Mechanical Engineering
Georgia Institute of Technology

Prof. Olivier Pierron
George W. Woodruff School of Mechanical Engineering
Georgia Institute of Technology

Date Approved: February 15, 2017

To my father, Kaya Yabansu,

my mother, Jale Yabansu,

my brother Erdem B. Yabansu

ACKNOWLEDGEMENTS

First, I would like to thank my advisor, Surya Kalidindi for sharing his academic support and guidance throughout my studies in both Drexel and Georgia Tech. None of the experience, wisdom and successes I achieved during my PhD studies would have been possible without him.

I am very thankful to Office of Naval Research (ONR) and program manager Dr. Williams M. Mullins for the financial support of my PhD studies under the award N00014-11-1-0759. I would also like to thank Prof. Richard W. Neu, Prof. Hamid Garmestani, Prof. Olivier Pierron and Prof. Antonia Antoniou for participating in my defense committee and reading my dissertation.

I would like to thank my father, Kaya Yabansu, my mother, Jale Yabansu and my brother, Erdem B. Yabansu for showing patience and support during my studies. At the hardest times of my life, they never stopped giving me their unconditional love and encouragement to pursue my dreams.

I would also like to thank the former and present members of our research group. First of all, I am thankful to Prof. Stephen R. Niezgoda from The Ohio State University for teaching me several aspects of materials science and informatics. I am thankful to Joshua B. Shaffer for his friendship and assistance in coding during my first year in Drexel. I am also thankful to Anne C. Hanna for helping me with derivations about localization relationships shown in this dissertation. Lastly, I would like to thank all other former and present group members who have supported me during my PhD studies.

TABLE OF CONTENTS

LIST OF TABLES

LIST OF FIGURES

x

LIST OF SYMBOLS AND ABBREVIATIONS

$Q_L(n)$	Orthonormal basis function
Z	Zener ratio
$\boldsymbol{p}_s$	Local response
$\boldsymbol{A}_t^L$	Fourier representation of influence function
M_s^L	Fourier representation of local microstructure descriptor
$\boldsymbol{\alpha}(r,n)$	Influence function
$m(x,n)$	Microstructure function
$P_n()$	n^{th} order Legendre polynomial
σ_{ij}	Stress tensor
ε_{ij}	Strain tensor
$t_i^{(e_i)}$	Surface tractions
u_i	Displacement
b_i	Body forces
C_{ij}	Elastic stiffness tensor
$\boldsymbol{I}$	Fourth rank identity tensor
$\boldsymbol{\Gamma}$	Symmetrized derivative of Green's function
$\boldsymbol{C}^{eff}$	Effective stiffness tensor
χ	Indicator function
δ_{ij}	Kronecker delta
Δ	Volume of spatial bin
$\boldsymbol{a}(x)$	Localization tensor

g	Crystal lattice orientation
s	Spatial bin
L	Local state index
T_l^{mn}	GSH functions
C_l^{mn}	GSH coefficients
φ_1	First Bunge-Euler angle
Φ	Second Bunge-Euler angle
φ_2	Third Bunge-Euler angle
$\mathfrak{I}()$	Fourier transform operator
$*$	Conjugate
$f(g)$	Orientation distribution function
$\langle\,\rangle$	Volume average
MKS	Materials Knowledge System
GSH	Generalized Spherical Harmonics
FE	Finite Element
FEM	Finite Element Method
MVE	Microscale Volume Element
RVE	Representative Volume Element
OLS	Ordinary Least Squares
ICME	Integrated Computational Materials Engineering
MGI	Materials Genome Initiative
P-S-P	Process-Structure-Property
PCA	Principal Component Analysis
DFT	Discrete Fourier Transform

FFT	Fast Fourier Transform
IDFT	Inverse Discrete Fourier Transform
RREF	Reduced Row Echelon Form
ODF	Orientation Distribution Function
MSD	Microstructure Sensitive Design
FZ	Fundamental Zone
MASE	Mean Absolute Strain Error

SUMMARY

Multiscale modeling of material systems demands novel solution strategies to simulating physical phenomena that occur in a hierarchy of length scales. Majority of the current approaches involve one way coupling such that the information is transferred from a lower length scale to a higher length scale. To enable bi-directional scale-bridging, a new data-driven framework called Materials Knowledge System (MKS) has been developed recently. The remarkable advantages of MKS in establishing computationally efficient localization linkages (e.g., spatial distribution of a field in lower length scale for an imposed loading condition in higher length scale) have been demonstrated in prior work. In prior work, the viability and computational advantages of the MKS approach were demonstrated in a number of case studies involving multiphase composites, where the local material state in each spatial bin of the volume element was permitted to be any one of a limited number of material phases (i.e., restricted to a set of discrete local states of the material). As a major extension, the MKS framework has been extended for polycrystalline aggregates which need to incorporate crystal lattice orientation as a continuous local state. Another important extension of the MKS approach that permits calibration of the influence kernels of the localization linkages for an entire class of low to moderate contrast material systems will also be presented. This major extension of the MKS framework for elastic deformation of polycrystals is achieved by employing compact Fourier representations of functions defined in the crystal orientation space. The viability of this new formulation will be presented for several case studies involving single and multi-phase polycrystals.

CHAPTER 1

INTRODUCTION

Most advanced material systems exhibit multiple length and temporal scales that play an important role on the material property which is strongly connected to multifunctional performance characteristics of the material system. It is very well acknowledged that chemical composition alone has a tremendous value in determining the performance characteristics. However, it is not only the chemical composition that control these characteristics, but the details of three dimensional hierarchical structure of the material that spans several length scales. Below in Figure 1, the atomistic scale, mesoscale and macroscale of a component can be seen. Even though the relationships between the material structure at multiple length scales shown in Figure 1, its evolution through different manufacturing processes and the macroscale properties are acknowledged to exist, the traditional approaches used in materials development has proven to be slow, expensive and effort-intensive. These efforts are heavily based on experimental approaches and they are slow, customized and not extensible to other material systems. For instance, it takes roughly 20 years from discovering an advanced material system to deploy it in a product in aerospace industry [1].

Indeed, the example above does not indicate that modeling and simulation are not included in design and discovery of new material systems. The modeling and simulation cover a big area of modern materials science research. However, optimization of material systems through modeling and simulation has not progressed as fast as the design of

components. For this manner, Integrated Computational Materials Engineering (ICME) approach was published in 2008 [2]. It aims to optimize the materials systems, manufacturing processes and component design before the material system is deployed in the product. Of course this approach is not limited to simple exchange of information between component design, manufacturing processes and computational materials science tools but it can also include open science tools, materials infrastructure, database and knowledgebase management, etc.
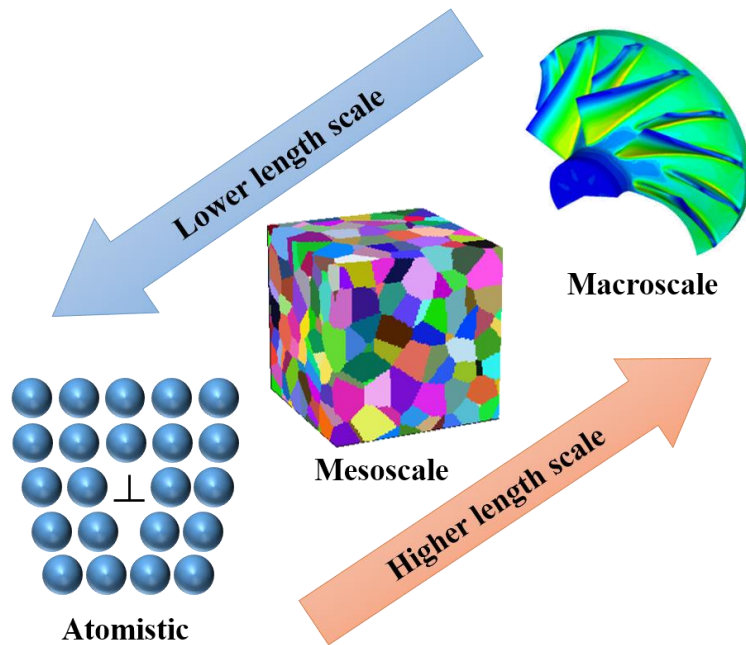
Figure 1: Some selected material length scales (from atomistic scale to macroscale)

Other than ICME, an initiative called Materials Genome Initiative (MGI) was launched in 2011 [1]. The initiative aims to integrate computational tools, experimentation and data informatics for accelerated materials development and design by bringing materials innovators, researchers and industry partners together through a materials innovation infrastructure. With this infrastructure, it is desired to deploy advanced

materials systems in half the time at a reduced cost than the traditional materials development approaches.

It should be noted that all these efforts focus on building/identifying processing-structure-property (P-S-P) linkages. Even though there has not been a rigorous and generic framework that can extract these linkages efficiently, in the past decades, materials scientists found out that not all details in multiple scales play an important role on a selected property (e.g. only crystal lattice orientation and thermodynamic phase identifier have significant effect on elastic properties). Hence, the efforts are directed to extract myriad details of material internal structure that are important to selected technology application. In other words, based on the experiences and insights on the relationships between the manufacturing processes, material internal structure and the performance characteristics, the focus is now on extracting and building the P-S-P linkages for advanced materials development.

1.1 Process - Structure - Property Linkages

The crux of the knowledge required to accelerate materials design and development lies in process-structure-property (P-S-P) relationships (see Figure 2). Process space defines all the possible manufacturing processes related to that material system in interest. These processes can involve machining, casting, forming, sintering, annealing, etc. One should keep in mind that all these different processes make a point in process space as well as the permutations of these processes [3]. These are called hybrid process routes and different routes essentially leads to distinct structures. Hence, the number of process routes that can be realized in process space for a material system is essentially infinite. Similarly,

3

structure space contains all the possible structures that can theoretically be defined for a selected material system. On the other hand, property measure is directly connected to performance characteristics and in our case, it indicates physical properties of a material structure (yield strength, elastic stiffness, thermal conductivity, etc).

Initial efforts were focused on linking a manufacturing process to a property measurement of the material system (simply linking process space to property space). These efforts involved extremely expensive and time consuming experimental techniques. The challenge in this approach lies in the fact that process space is not a continuous space. Following a different hybrid route or changing the sequences of a combination of multiple processes does not correspond to a change with an interpretable pattern in property space. In other words, the interpolation in process space is not a meaningful task, rendering every single hybrid route in this space a discrete point. With the inclusion of structure in the connection between the process and property spaces, there is a tremendous potential to actually build these linkages in a more generic and extensible way. Since any point in structure space can be defined in a statistical (or probabilistic) manner, the interpolation between properties becomes possible.

P-S-P relationships have been usually formulated with a flow from processing to structure and from structure to property [4]. As stated before, there is no direct obvious link between the process and property space. Hence, the quantification of structure plays in important role in exploring the P-S-P relationships [5-7]. In Figure 2 shown the P-S-P spaces. The conventional approach in exploring these relationships involved a bottom-up flow of information. Olson [4] explains this flow of information as the deductive cause-and-effect logic of science. On the other hand, the top-down flow of information is seen as

the inductive goal-means relations of engineering flow. The top-down flow of information is realized through considered invertible linkages which essentially constitute materials design.
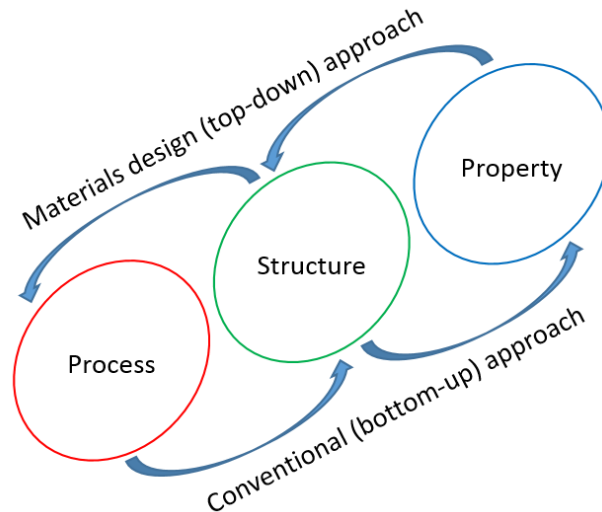
Figure 2: Process, structure and property spaces.

1.2 Hierarchical Multiscale Modeling

The successful design and manufacture of new/improved materials with vastly enhanced properties or performance characteristics are contingent on the availability of a computational framework that efficiently bridges the relevant hierarchical length/structure scales in the material (also referred to as hierarchical multiscale modeling) [4, 8-12]. In most hierarchical multiscaling approaches, the focus has thus far been in communicating the effective properties to the higher length scales, i.e. on homogenization. On the other hand, communicating the information from higher length scale to a lower length scale is called localization. As an example, localization may involve the spatial distribution of the response field of interest (e.g. stress or strain rate fields) at the microscale (on a representative volume element) for an imposed loading condition at the macroscale. In

conventional hierarchical multiscale models, homogenization is handled by solving the governing field equations in a lower length scale. Then, the effective property of the volume in lower length scale is transferred to a higher length scale as a single (homogenized) property, which is the representative property of the material neighborhood in the lower length scale. However, localization is as important as homogenization if not more important. The difficulty in implementing localization in a hierarchical multiscale model lies in solving the governing field equations at a lower length scale. This becomes computationally inefficient if the space of microstructures that have to be explored is too large. Hence, there is often very little information passed from higher length scale to lower length scale in hierarchical multiscale modeling. Historically, the multiscale materials modeling efforts have focused on only one way of transfer of information (either homogenization or localization). Even though both homogenization and localization have been incorporated to physics-based hierarchical multiscale modeling [13-16], it was shown in previous studies that employing data-based approaches have tremendous advantages in terms of computational efficiency [17-26].

1.3 Materials Knowledge System

In recent years, a novel, computationally efficient, bi-directional, scale-bridging framework called materials knowledge systems (MKS) has been formulated [19, 22-25, 27]. In the MKS framework, the focus is on expressing the localization relationships of interest in the form of a simple algebraic series whose terms capture systematically the individual contributions from a hierarchy of local microstructure descriptors. The specific form of the algebraic series used in the MKS approach is adopted from the well-established statistical continuum theories [28, 29]. In both of these approaches (MKS and the statistical

continuum theories), the localization linkage takes the form of a series where each term is expressed as a convolution product of a physics-capturing kernel with a higher-order local microstructure descriptor. However, the main difference between the two approaches is that the localization linkage in the MKS approach is calibrated to datasets obtained from established numerical approaches for the materials phenomena of interest. For example, in studies of micromechanical phenomena, the physics-capturing kernels in the MKS linkages are calibrated to results obtained from finite element models for a diverse set of example microstructures. The most impressive benefit of the MKS approach lies in the dramatic reduction of the computational cost, often by several orders of magnitude compared to numerical approaches typically employed in microstructure design problems. The MKS methodology has thus far been successfully applied to capturing thermo-elastic stress (or strain) distributions in composite representative volume elements (RVEs), rigid-viscoplastic strain rate fields in composite RVEs and the evolution of the composition fields in the spinodal decomposition of binary alloys [19, 23, 24].

Almost all of the case studies explored thus far have been restricted to composite material systems with a limited set of discrete local material states (i.e. two-phase or three-phase microstructures). However, most materials of interest in emerging technologies exhibit local states that are much more complicated. For example, most advanced structural materials exhibit polycrystalline microstructures, where the spatial distribution of the crystal lattice orientations at the microscale plays an important role in controlling their effective properties. High throughput evaluation of the responses of a large set of microstructures (as one might need in optimizing the material performance in a selected application) with such complex local states requires a major extension of the MKS

7

framework that allows efficient treatment of tensorial local states (e.g. crystal lattice orientation) and their associated continuous local state spaces. In this regard, it should be recognized that it is possible to treat continuous local states simply by binning the continuous local state space (as described in our earlier work [19]). However, a primitive binning of the local state space is expected to prove highly inefficient, computationally, in capturing accurately the localization linkages of interest, especially in situations where the microscale response in the material microstructure shows high sensitivity to the local state (e.g. plastic response of crystalline states).

1.4 Problem Statement and Motivation

The localization in hierarchical multiscale modeling is a computationally inefficient task due to solving governing field equations in lower length scale. The motivation behind this dissertation is to accelerate the localization in hierarchical multiscale modeling for polycrystalline aggregates through data-driven MKS approach. It is presented in this dissertation that recently developed novel generalized MKS framework allows a rigorous treatment of the complex local state variable, crystal lattice orientation through compact GSH basis functions. It should be noted that GSHs have already been demonstrated to produce highly efficient and compact spectral descriptions of functions defined on the orientation space in other applications in prior literature [11, 30-44]. It will be shown MKS approach predict the local response field orders of magnitudes faster than conventional physics based models. The viability of the new MKS formulation presented in this dissertation is demonstrated with case studies of both single phase [17, 20] and multiphase polycrystals.

Chapter 2 summarizes some fundamental mathematical concepts that are required to follow the derivations and formulations employed in this dissertation. In Chapter 3, a generalized MKS framework will be derived from Kroner's expansion and a templated workflow of MKS approach will be presented. In Chapter 4, 5 and 6, MKS case studies for single phase polycrystalline materials, a broad class of single phase polycrystalline materials and multiphase polycrystalline materials are presented, respectively. In Chapter 7, the results of the new generalized MKS framework is discussed and in Chapter 8, the potential new directions for MKS are discussed.

CHAPTER 2

REVIEW OF FUNDAMENTAL CONCEPTS

This chapter includes the review of some fundamental concepts that are required to follow the derivation and expressions used in the case studies. Even though this section summarizes the most important properties of the fundamental mathematical concepts in interest, readers should keep in mind that the information shared about these concepts in this thesis is far from being comprehensive. Fortunately, these concepts are utilized on a daily basis by a very large number of scientists from a wide range of disciplines. Hence, there are numerous online references and textbooks which includes these theories in a systematic and detailed manner. As quick references, readers can find detailed information about these concepts in [45-50].

2.1 Fourier Series

Fourier series are sum of sine and cosine series to represent periodic functions. If a function, $f(x)$, is periodic, then:

$$f(x) = f(x + p) \tag{1}$$

where p is a positive number which represents the period such that the function repeats itself after every interval of p. This also implies that the function is also periodic on the intervals of multiples of this number (i.e. $f(x) = f(x + np)$ where n is any integer). Let us assume the period, p, of the function $f(x)$ is 2π. Then, this function can be represented with Fourier series as below:

$$f(x) = a_0 + \sum_{n=1}^{\infty} a_n \cos(nx) + b_n \sin(nx) \tag{2}$$

where a_n and b_n are the coefficients of the series (can be called Fourier coefficients as well). On the other hand, a_0 term is the constant term of the representation (in some literature it is also called bias). From Eq. (2), it can be seen that each monomial in these series has a period of 2π. Theoretically, if one keeps infinite number of terms in the Eq. (2), the right side of the equality is an exact representation.

The most important part of the Fourier series is the coefficients which characterize the representation of the function. These coefficients can be found from orthogonality of trigonometric functions. Two functions are called orthogonal if their integral (or inner product) over a period p is zero for $f \neq g$:

$$\langle f.g \rangle = \int_{-p/2}^{p/2} f(x)g(x)dx = 0 \ \ where \ f \neq g \tag{3}$$

The orthogonality rule holds for sine and cosine functions. By taking the equality in Eq. (3) in consideration, similar expressions can be written for trigonometric functions:

$$\int_{-\pi}^{\pi} \cos(nx) \cos(mx) = 0 \ \ , \ \ (n \neq m)$$

$$\tag{4}$$

$$\int_{-\pi}^{\pi} \sin(nx) \sin(mx) = 0 \ \ , \ \ (n \neq m)$$

It should be kept in mind that the limits of integral are taken as from $-\pi$ to π as an example. The expression holds for any set of limits as long as the period is kept as 2π. To obtain the definitions of Fourier coefficients in Eq. (2), we multiply each side of Eq. (2) with 1,

11

$sin(mx), cos(mx)$, then take integral of both sides for all 3 cases. Then, we can reach the expressions below:

$$a_0 = \frac{1}{2\pi} \int_{-\pi}^{\pi} f(x)dx$$

$$a_n = \frac{1}{\pi} \int_{-\pi}^{\pi} f(x) \cos(nx) \, dx \tag{5}$$

$$b_n = \frac{1}{\pi} \int_{-\pi}^{\pi} f(x) \sin(nx) \, dx$$

The Fourier representation in Eq. (2) can be repeated for any arbitrary period p:

$$f(x) = a_0 + \sum_{n=1}^{\infty} a_n \cos\left(\frac{n\pi x}{p}\right) + b_n \sin\left(\frac{n\pi x}{p}\right) \tag{6}$$

where the Fourier coefficients a_0, a_n and b_n can be written as:

$$a_0 = \frac{1}{p} \int_{-p/2}^{p/2} f(x)dx$$

$$a_n = \frac{2}{p} \int_{-p/2}^{p/2} f(x) \cos\left(\frac{n\pi x}{p}\right) dx \tag{7}$$

$$b_n = \frac{2}{p} \int_{-p/2}^{p/2} f(x) \sin\left(\frac{n\pi x}{p}\right) dx$$

From this point on, orthogonality will play a major role in the utilization of different basis functions in the localization relationships of MKS framework. The readers are strongly encouraged to follow the derivation of Fourier coefficients from a detailed source as it will be shown that in all of the case studies shown in this dissertation will involve Fourier

coefficients in the representation of functions. Hence, employing orthogonality and Fourier coefficients have the utmost importance in deriving the expression used in MKS framework.

2.2 Fourier Transform

Fourier transform is a very common tool in analyzing the signals in frequency domain. It is a remarkable tool that by simply applying the transform to a signal, we can extract or identify information about the signal as well as manipulating it in a way that we cannot achieve in time domain. Let $f(x)$ be a function in time domain with an input signal of x which represent time, then $f(x)$ can be written in frequency domain as:

$$F(k) = \int_{-\infty}^{\infty} f(x)e^{-2\pi ikx}dx \qquad (8)$$

where k is the frequency and i is $\sqrt{-1}$. The operation in Eq. (8) is called Fourier transform (or forward Fourier transform) and $F(k)$ indicates how much amplitude $f(x)$ has at frequency k. It should be expressed strongly that there is one-to-one mapping between signal in time domain, $f(x)$ and signal in frequency domain, $F(k)$. Thus if we know a frequency response of a signal, $F(k)$, then we can obtain the signal in time domain with inverse Fourier transform and it can be written as:

$$f(x) = \int_{-\infty}^{\infty} F(k)e^{2\pi ikx}dk \qquad (9)$$

Another way of expressing forward and inverse Fourier transforms is through angular frequency. In Eq. (8) and (9), k is the ordinary frequency which is measured in Hz.

If the frequency response is defined in terms of angular frequency, ω (which is $2\pi k$ and measured in *rad/s*), then Eq. (8) can be rewritten as:

$$F(\omega) = \frac{1}{\sqrt{2\pi}} \int_{-\infty}^{\infty} f(x)e^{-i\omega x}dx \tag{10}$$

The way Fourier transform is written depends on the choice. But historically, physicists preferred using angular frequency as an independent variable in frequency domain, while mathematicians usually preferred ordinary frequency. For consistency from this point on, the functions in frequency domain will be defined in terms of ordinary frequency, k.

Fourier transform is the central tool for scientists involved in digital signal processing. Hence, the input domain is usually called the time domain. However, today Fourier transform is employed by scientists from a wide range of disciplines and its utilization is not limited to signals in time domain. In our case, Fourier transform is applied in spatial domain. If $f(x)$ is a periodic function with a period of T, the expressions in Eq. (8) and (9) can be rewritten as below:

$$F(k) = \frac{1}{T} \int_{-T/2}^{T/2} f(x)e^{-\frac{2\pi ikx}{T}}dx \tag{11}$$

$$f(x) = \frac{1}{T} \sum_{k=-\infty}^{\infty} F(k)e^{2\pi ikx} \tag{12}$$

Attention must be paid to Eq. (12). If T goes to infinity, this expression yields to Eq. (9). These formulations are especially important in representation of aperiodic signals with Fourier series. Even though these expressions are very general and extensible to any real function, we are particularly interested in the discrete format of signals. Since a very large

14

percentage of existing data is stored today in a digitized environment, discrete representations and transforms have been heavily utilized in the MKS framework.

2.3 Discrete Fourier Transform (DFT)

As stated in the previous subsection, all of the data generated and used in this thesis is represented as digital signals and stored in accordingly suitable digitized environments. Hence, discrete Fourier transform (DFT) plays a major role in calibrating influence functions.

Let f_x be a discrete signal where of $x = 0, 1, \ldots, N-1$ and is assumed to be periodic over an interval of $[a, b]$, then the discrete Fourier transform (DFT) of f_x can be written as:

$$F_k = \Im(f_x) = \sum_{x=0}^{N-1} f_x e^{-\frac{2\pi ikx}{N}} \tag{13}$$

where $\Im(\ )$ represents the DFT operation and F_k are the Fourier coefficients of signal f_x. Indeed, one-to-one mapping between the signals in spatial domain and spatial frequency domains holds for DFT as well, like in the Fourier transform of continuous functions (or signals). Thus the inverse discrete Fourier transform (IDFT) can be written as:

$$f_x = \Im^{-1}(F_k) = \frac{1}{N} \sum_{x=0}^{N-1} f_x e^{-\frac{2\pi ikx}{N}} \tag{14}$$

where $\Im^{-1}(\ )$ represents the IDFT operation. From Eq. (13) and (14), it can be seen that if one knows frequency response F_k, any point in f_x can be recovered individually as there is

no dependence between the values of f_x in IDFT expression (this holds for vice versa as well).

There are several important features of DFT (and IDFT) that can be deduced from Eq. (13) and (14):

1) The formulations are completely independent of sampling window size (i.e. $(b - a)/N$). Hence, the periodicity can be assumed according to the spatial frequency index $(x = 0, 1, ..., N - 1)$ without including sampling window size in the calculations as long as there is a consistency between multiple data sets (or signals).

2) Uniformly discretized grid in spatial domain is exactly the same as in spatial frequency domain $(x = 0, 1, ..., N - 1$ and $k = 0, 1, ..., N - 1)$.

3) F_k are the Fourier coefficients of f_x, and they are analogous to the Fourier coefficients discussed in previous subsection about Fourier transform of continuous signals. F_k indicates the amplitude of signals at discrete frequency of k.

4) F_k has a special meaning at frequency $k = 0$. It can be seen from Eq. (13) that the exponential term becomes 0 at this value. Thus, F_k has the sum of all terms in f_x and the average of f_x can be found by simply dividing this term by the number of points in the signal, N. This feature is considered the most important feature in this thesis as it will play a major role in calibration of localization kernels and defining the average macroscopic response.

DFT operation yields some very important properties. Some of these properties will be an integral part of the approaches used in this study. It is also reminded again that the content shared here is not comprehensive and readers are strongly encouraged to go

through a digital signal processing textbook to have a full grasp of these features and properties.

2.3.1 Symmetry of DFT

DFT operation produces a symmetric set of Fourier coefficients, F_k (under the assumption that all points in f_x are real valued). An example real valued signal f_x and its frequency response F_k can be seen in second and third columns of **Error! Reference source not found.**, respectively. The first column is for indices of both spatial location and spatial frequency (recall that both spatial and frequency domains are on the same discretized grid).

Table 1: An example input signal (second column) and its frequency response (third column)

k or x	f_x	F_k
0	1	14
1	3	$-2.58 + 0.49i$
2	4	$1.15 - 1.69i$
3	0	$-2.07 - 5.16i$
4	2	$-2.07 + 5.16i$
5	3	$1.15 + 1.69i$
6	1	$-2.58 - 0.49i$

It can be seen that the frequencies from $k = 1$ to $k = 3$ is redundant with the frequencies from $k = 4$ to $k = 6$. It is clear that the first half of the frequency response is simply the complex conjugate of the other half. This can be formulated as below:

$$F_{N-k} = F_k^*$$ (15)

where * represents the complex conjugate. There are two important aspects about this property. First of all, attention must be paid to the indexing for frequency, k. Since there is no frequency N, this equality does not hold for $k = 0$ frequency. Second of all, the symmetry property in Eq. (15) does not hold for complex input signals. However, this will not be a difficulty in the case studies here as the input signals will always be real valued. It will be shown in following sections that this property is very crucial in saving computational times in calibration of localization linkages and will be utilized in all of the case studies.

2.3.2 Linearity of DFT

DFT has a property of linearity. This states that DFT of a sum of two input signals is equal to the sum of DFT of each signal. This can be written as below:

$$\Im(f_x + g_x) = \Im(f_x) + \Im(g_x) \tag{16}$$

where f_x and g_x are two separate signals in spatial domain. This property enables us to add, subtract and modify information in both frequency and input domains. Also if the input signal can be decomposed into multiple signals, then this decomposition can be done in frequency domain as well.

2.3.3 Convolution property of DFT

Convolution property of DFT is the major property that enables the tremendous computational efficiency of MKS. Convolution can be expressed as the sum that expresses the overlap of a function, g_x as it is shifted over another function f_x. In discrete format, the convolution of f_x and g_x for discrete points of $x = 0, 1, \ldots, N-1$ can be expressed as:

$$f * g = \sum_{x=0}^{N-1} f_x g_{k-x} \tag{17}$$

The operation in Eq. (17) can be performed by employing DFT operations. It turns out that by applying IDFT operation to the pointwise multiplication of frequency responses of two functions f_x and g_x, the same expression on the left hand side of Eq. (17) can be obtained.

$$f * g = \mathfrak{I}^{-1}(F_k G_k) = \sum_{x=0}^{N-1} f_x g_{k-x} \tag{18}$$

The expression in Eq. (18) is particularly important due to the number of operations involved in calculation of the convolution. The convolution in Eq. (17) requires N^2 number of operations while the calculation in frequency domain requires on N operations. This is a remarkable reduction in computational operations and it is used in several image processing and feature extraction operations such as image resizing, dilation, sharpening, filtering, etc. Convolution property will be exploited in all of the case studies in this dissertation. Even though the tools and expressions used here are open to utilization of other spectral operations, so far DFT proved itself indispensable due its convolution property.

Another important concept is fast Fourier transform (FFT). FFT operation produces the same result as DFT operation within machine precision. The difference comes from the fact that FFT does the Fourier transform by factorizing the DFT matrix into a product of sparse factors. The benefit of applying FFT lies in its computational efficiency. The standard DFT operation has a complexity of N^2, while the complexity of FFT operation is only $N \log N$ (i.e. this computational gain is one of the key reasons why the localization

19

relationships and microstructure quantification tools are utilized in frequency space). Hence, it is acknowledged here that DFT operation refers to the fundamental concept of representation of discrete functions, while FFT will be referred to as a specific computational algorithm to reach abovementioned representations. In all of the case studies involved in this thesis, the functions (or discrete spatial signals) are cast into spatial frequency space by employing FFT algorithms. However, DFT term will be used explicitly for all transformations from spatial domain to spatial frequency domain.

2.4 Legendre Polynomials

Legendre polynomials are a set of polynomials which are commonly used in the solutions to physical problems and they are found from Legendre differential equation:

$$(1 - x)\frac{d^2y}{dx^2} - 2x\frac{dy}{dx} + n(n + 1)y = 0 \tag{19}$$

When Legendre differential equation is solved according to series method, it has only convergence for $|x| < 1$ with singularities at $x = \pm 1$ (there is no convergence for series solution beyond these points). Since Legendre polynomials is a well-established mathematical concept, the derivation of Legendre polynomials will not be included here. The derivation can be found in several fundamental calculus and mathematical methods books. Legendre polynomials can be found once the series solution below is achieved:

$$P_n(x) = \sum_{m=0}^{M} (-1)^m \frac{(2n - 2m)!}{2^n m! (n - m)! (n - 2m)!} x^{n-2m} \tag{20}$$

where M is $n/2$ for even n and $(n-1)/2$ for odd n. From here it can be deduced that the polynomials with even degree, the coefficients are also even and vice versa. This can be clearly seen in Eq. (21), where Legendre polynomials up to degree $n = 5$ are listed.

$$P_0(x) = 1$$

$$P_1(x) = x$$

$$P_2(x) = \frac{1}{2}(3x^2 - 1)$$

$$P_3(x) = \frac{1}{2}(5x^3 - 3x) \tag{21}$$

$$P_4(x) = \frac{1}{8}(35x^4 - 30x^2 + 3)$$

$$P_5(x) = \frac{1}{8}(63x^4 - 70x^2 + 15)$$

Another feature of these polynomials is that the polynomials with an even degree are even functions. The polynomials in Eq. (21) are visualized in the interval of $[-1,1]$ in Figure 3. It can be seen that values of the polynomials with an even degree are symmetric with respect to $x = 0$ line, while the polynomials with an odd degree are symmetric with respect to origin (i.e. $(x, y) = (0,0)$). In other words, $P_n(x) = P_n(-x)$ for even n and $P_n(x) = -P_n(-x)$ for odd n.
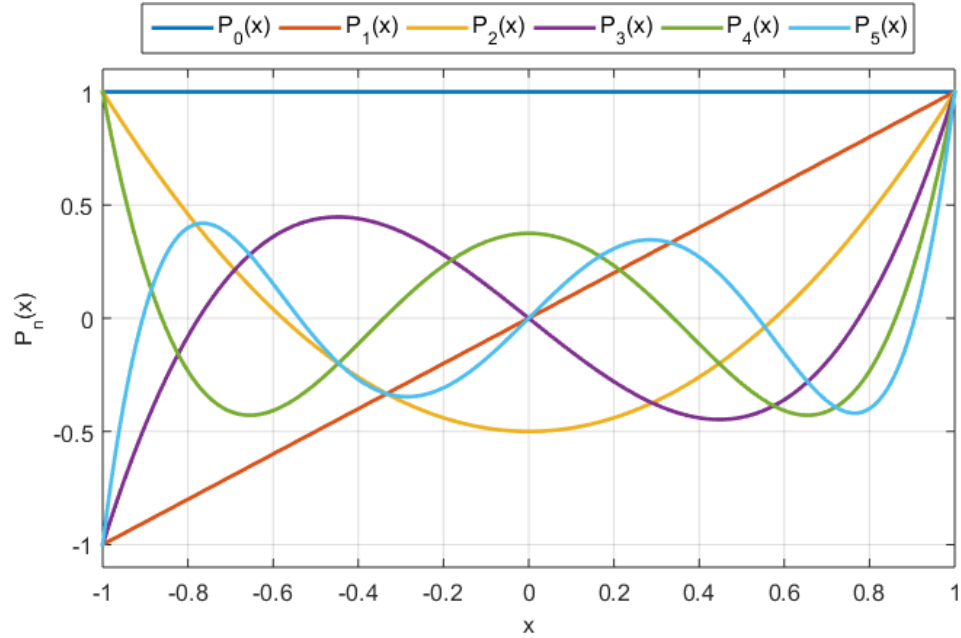
Figure 3: Plot of the Legendre polynomials up to 5th degree in the interval of $[-1, 1]$.

The most important property of Legendre polynomials is the orthogonality and they form an orthogonal basis in the interval of $[-1,1]$. This orthogonality can be expressed as:

$$\int_{-1}^{1} P_n(x)P_m(x)dx = \frac{2}{2n+1}\delta_{mn} \tag{22}$$

where δ_{mn} is Kronecker delta and it is equal to 1 if $m = n$ and to 0 otherwise. Orthogonality is the main motivation behind the utilization of these polynomials in the local state description. It will be shown in one of the following sections that Legendre polynomials will be integrated into the localization relationships for tensorial variables and they will form a suitable Fourier basis with other basis functions due to its orthogonality property.

2.5 Multiple Linear Regression

Linear regression is a machine learning approach that forms the core of calibration process involved in obtaining influence functions in this dissertation. Although the fundamentals of regression methods have been well established, today there are numerous advanced methods that are used to solve problems in wide range of areas such as artificial intelligence, finance, physics, etc. The method used in this dissertation is multiple linear regression. In all of the case studies presented here, multiple linear regression will be the central part of calibration process. Readers should keep in mind that the calibration process that will be covered in the next sections is not limited to multiple linear regression. In fact, advanced regression methods involving constrained optimization techniques [51], nonlinear regression [52], Bayesian regression [46], etc. might lead to more efficient calibration process and more accurate linkages. However, these methods are beyond the scope of this dissertation, since the focus is on calibration of influence functions that constitute MKS and multiple linear regression proved its performance in present case studies explained here.

Let y_n be the nth observation (or dependent variable) based on the kth input variable $x_{n,k}$ (or independent variable) where $n = 1, 2, ..., N$ and $k = 1, 2, ..., K$. Then, the linear relationship between $x_{n,k}$ and y_n can be expressed as:

$$y_n = \beta_K x_{n,K} + \beta_{K-1} x_{n,K-1} + \cdots + \beta_1 x_{n,1} + \beta_0 + \varepsilon_n \tag{23}$$

where β_k are regression coefficients and ε_n are the error terms. Attention must be paid to coefficients β_0. This term is not multiplied with any independent variable. Thus, it stands

as the constant term (or bias). The expression in Eq. (23) can be expressed in matrix notation as well.

$$y = X\beta + \varepsilon \tag{24}$$

where

$$y = \begin{bmatrix} y_1 \\ y_2 \\ \vdots \\ y_N \end{bmatrix}, \quad X = \begin{bmatrix} 1 & x_{1,1} & x_{1,2} & \cdots & x_{1,K} \\ 1 & x_{2,1} & x_{2,2} & \cdots & x_{2,K} \\ \vdots & \vdots & \vdots & & \vdots \\ 1 & x_{N,1} & x_{N,2} & \cdots & x_{N,K} \end{bmatrix}, \quad \beta = \begin{bmatrix} \beta_0 \\ \beta_1 \\ \vdots \\ \beta_K \end{bmatrix}, \quad \varepsilon = \begin{bmatrix} \varepsilon_1 \\ \varepsilon_2 \\ \vdots \\ \varepsilon_N \end{bmatrix} \tag{25}$$

Regression coefficients characterizes the model between input and output and can be found by ordinary least squares (OLS) method. The derivation of OLS formulation will not be shown here, however readers are encouraged to follow it through a machine learning or statistics book. If we differentiate the sum of the squares of error terms with respect to each regression coefficient, we can reach the expression below:

$$X^T X \beta = Xy \tag{26}$$

where T in the superscript represents the matrix transpose. From Eq. (26), the predictors can be found:

$$\beta = (X^T X)^{-1} Xy \tag{27}$$

There are a few points that can be made about the formulation in Eq. (27):

1) The matrix $X^T X$ is called the covariance matrix. It is a symmetric and square matrix with the dimensions of $K \times K$.

2) If there is linear dependency between the rows of covariance matrix, there is not a unique solution (i.e. the covariance matrix is singular). There are several methods to deal with the linear dependency such as reducing the matrix to reduced row echelon form (RREF) to find pivot points and find a solution according to these by assuming the others zero.

3) If there are more regression coefficients in the model than the number of unique observations, then the covariance matrix becomes singular and there is no unique solution for regression coefficients.

2.6 Principal Component Analysis

Principal component analysis (PCA) is a method that transforms the coordinate system in which a set of observations exists in, in such a way that it is viewed from the most informative way. PCA performs a linear transformation of the original coordinate system to a new orthogonal space where the axes are ordered according to the eigenvalues that result from the eigenvalue decomposition employed. First principal component contains the largest variance in the data which is reflected by the first eigenvalue and so on.

Principal components can be found from eigenvalue decomposition applied on the covariance of the data matrix. Consider a data matrix X where rows and columns represent the observations and dimensions, respectively. If we define the principal components with a matrix U, then the data set can be projected to principal component space by:

$$\tilde{X} = XU^T \tag{28}$$

The columns of U denote the principal components and $\widetilde{X}$ is the data matrix in the principal component space. Since the principal components are orthogonal to each other the covariance matrix of the data in principal component space is a diagonal matrix and can be written as:

$$S_{\widetilde{X}} = \widetilde{X}^T \widetilde{X} \tag{29}$$

The expression in Eq. (28) can be rewritten in terms of the data matrix defined in original space as:

$$S_{\widetilde{X}} = (XU)^T(XU) = U^T X^T X U = U^T S_X U \tag{30}$$

The term S_X at the right hand side of Eq. (30) is the covariance matrix of the data in original space (i.e. $S_X = X^T X$). The trick is to find a set of eigenvectors for this covariance matrix so that $S_{\widetilde{X}}$ becomes a diagonal matrix. Since S_X is a symmetric matrix, it can be written in terms of its eigenvalues D and eigenvectors E as below:

$$S_X = EDE^T \tag{31}$$

If we set the eigenvalues E equal to U, the right hand side of Eq. (30) can be written as:

$$S_{\widetilde{X}} = U^T(UDU^T)U = (U^T U)D(U^T U) = D \tag{32}$$

From the expression in Eq. (32), it is evident that U makes a diagonal $S_{\widetilde{X}}$ matrix. It is obvious that the principal components of X are the eigenvectors of covariance matrix S_X and the first diagonal value of S_X (assuming the diagonal values are in an ascending order) indicates the variance of first principal component U_1. In practice, PCA simply involves two steps; mean centering the data and extracting the eigenvectors of covariance matrix

$X^T X$. In most cases, the eigenvalues start decaying to zero values very quickly and usually a less number of principal components than the dimensions are actually required to retain the variance information of the data. The percentage of variance captured by the first R principal components can be written as:

$$J = \frac{(\sum_{i=1}^{R} \boldsymbol{D}_i)}{tr(\boldsymbol{D})} \times 100 \tag{33}$$

PCA is visualized through a simple example shown in Figure 4. A set of observations with 2 dimensions (x_1 and x_2) is seen on the left side of the figure along with the Gaussian distribution of points for each dimension. These data points are generated based on the covariance shown at the bottom left corner. From the off-diagonal elements of covariance matrix and the distribution of points in $x_1 \; vs \; x_2$ space, 2 dimensions are strongly correlated to each other. As we go further in x_1 direction, x_2 values of data points increase as well. When we apply PCA to this ensemble, we can obtain the principal component space shown at the right side of the plot. In principal component space, the data points have high variance in PC1 direction and PC2 values of data points are not correlated to PC1 values. This is also evident in the covariance matrix of data points in principal component space. The off-diagonal elements of covariance matrix are zero (i.e. there is no correlation between PC1 and PC2). On the other hand, the variance in PC1 is 30 times of PC2, rendering the information in PC2 insignificant. This insignificance can also be seen in the Gaussian distributions shown on the side and bottom of both plots. In original space, the data has strong variance in both dimensions while PC1 has much more variance than any other distribution with the distribution of PC2 has very low variance and a sharp peak at the mean value. To analyze the data points in new space, we only need the information

from PC1 as PC2 does not contain any important information about the nature of the data hence it can be considered as noise. Indeed, this is a grossly simplified example. However, even from this example we can see that PCA does not only extract the strong evident information from the data sets, it also helps us to reduce the dimensions in defining the points.
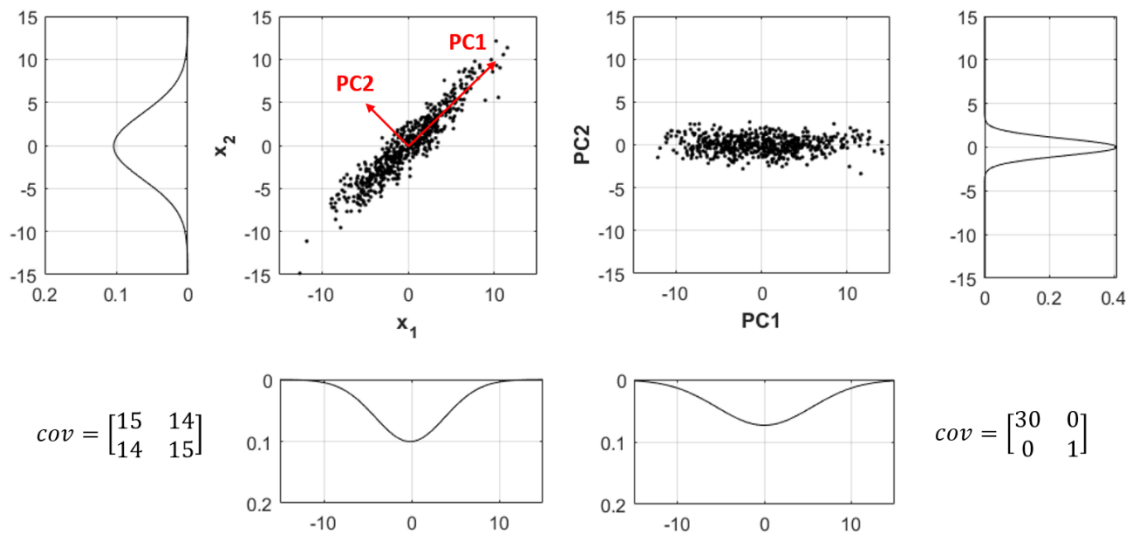
Figure 4: Visualization of PCA with a set of observations with two dimensions.

CHAPTER 3

GENERALIZED MKS FRAMEWORK

The localization relationships of MKS are derived from the homogenization relationships mainly developed by Kroner [28, 29] and Torquato [53, 54]. Homogenization theory simply focuses on finding an effective property value that is representative of the averaged or macroscopic property of the volume in interest. The theories that were started decades ago are based on perturbation expansions and higher order microstructure statistics. The present protocols to measure effective property for heterogeneous materials heavily depends on primitive measures such as grain size [55], volume fraction [56], nearest neighbors [57], etc. These basic measures can be misleading in building reliable P-S-P linkages. Hence, the heterogeneity of the structure must be accounted for to reach the effective property in in interest. It is well known that myriad details of the microstructure can only be captured by higher order functions (or statistics) and abovementioned perturbation expansions are completely based on the expansion of these functions.

Even though homogenization theories try to predict the effective properties of a material volume in interest, theory is formulated in such a way that a macroscopic loading or boundary condition is mapped to a lower level by localization terms. In this section, this part of the formulation will be exploited to derive the localization relationships of MKS. Indeed, some assumptions have to be made to derive the localization relationships from the homogenization theories mentioned in the first paragraph. Two length scales, macroscale and mesoscale that we are interested in can be seen in Figure 5. The first assumption is that

there is a significant difference (preferably several orders of magnitude) between the length scales that are implemented in the theories ($L \gg l$). If the length scale in lower level, l is in vicinity of the order of average particle (or grain) size, the local microstructure properties will change significantly when we move from one point to another with this length. However, the effective (or averaged) properties will decay to similar values for different volumes of the material system due to significant difference between the length scales of two levels. In other words, the fluctuations of the property in higher level must be very slow (or small) while the fluctuations in the lower level must be fast. These are also called global and local fluctuations of property in two different levels of a material system [54].

(a) Macroscale   (b) Mesoscale
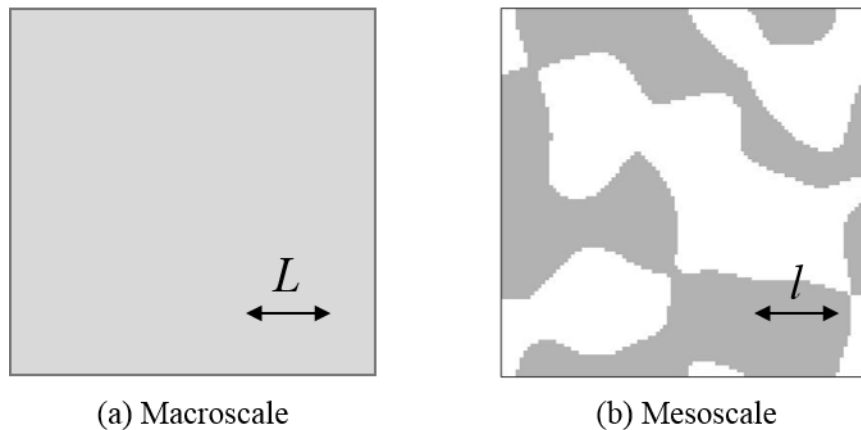
Figure 5: Two different length scales of a hypothetical material system (Macroscale (a) and Mesoscale (b))

   The second assumption is the eligibility of field equations and constitutive theories at both length scales. The localization relationships are derived from the homogenization theories under the assumption that the constitutive behavior of the material system is the same in both length scales. Since the constitutive behavior in interest is elastic behavior of polycrystalline aggregates, same linear elastic field equations can be applied in both macroscale and mesoscale.

This chapter includes the perturbation expansions used in homogenization theories, derivation of MKS localization relationships from these theories and the detailed explanation of the end result (MKS series expansion) obtained from the derivation. Since elasticity is the main material constitutive behavior we are interested in, a brief review of elasticity is included before the derivation and detailed explanation of localization relationships.

3.1 Theory of Linear Elasticity

The material constitutive behavior in interest in this dissertation is linear elastic behavior. Hence, understanding the basic concepts of linear elasticity such as stress, strain, material symmetry are means to an end in understanding the content here. It should be noted that the concepts about linear elasticity shared in this subsection is only for review purposes for people who are already confident in theory of linear elasticity. Readers who are not familiar with these concepts are strongly encouraged to follow the basics and details through a standard elasticity or continuum mechanics textbook.

Another crucial point is the indicial (Einstein) notation used in both this section and following sections where case studies are presented. If an index appears twice in a monomial, summation is meant over that index unless it is stated otherwise. Hence, the summation signs are omitted in the following content. The fundamentals of indicial notation can be found in several textbooks and online sources.

3.1.1 Stress

In the center of elasticity theory lies the state of stress. Stress is usually defined as the ratio between the average force applied per unit area, ΔF and a selected surface element, ΔS.

$$t = \frac{\Delta F}{\Delta S}$$
(34)

The definition given in Eq. (34) is valid for only the selected surface ΔS. The number of surfaces that can pass through a point defined in space is essentially infinite and the stress is different for each of these surfaces. Thus, having the definition in Eq. (34) as a general stress description is a meaningless task. Considering the above argument, we can generalize the stress definition as a vector as below:

$$t_i^{(n)} = \sigma_{ij}.n_j$$
(35)

where $t_i^{(n)}$ is the stress vector defined on a surface with a unit normal vector, n. The stress vector is illustrated with blue arrows in Figure 6. Let us assume the body shown in Figure 6 as an infinitesimal cubic element whose face normals coincide with the components of sample frame x_1, x_2 and x_3. The state of stress of this infinitesimal element is represented by stress tensor σ_{ij} which is a second rank tensor. This tensor consists of nine components where 3 components represent the normal stresses while other 6 components are shear stresses. Stress tensor can be written in matrix format as below:

$$\sigma_{ij} = \begin{bmatrix} \sigma_{11} & \sigma_{12} & \sigma_{13} \\ \sigma_{21} & \sigma_{22} & \sigma_{23} \\ \sigma_{31} & \sigma_{32} & \sigma_{33} \end{bmatrix} \tag{36}$$

where normal stresses are the diagonal components and the shear components are the off diagonal components. Stress tensor relates the stress vector $t_i^{(n)}$ to the unit normal n for a selected surface which is perpendicular to this normal. There are several important points that can be said about stress tensor:

1) According to principal of conservation of angular momentum, equilibrium of a body requires that the sum of all moments with respect to an arbitrary point is zero. From this argument, it can be shown that stress tensor is symmetric (i.e. $\sigma_{ij} = \sigma_{ji}$).

2) Stress tensor obeys the rule of transformation laws under a change in coordinate system. In other words, the stress state in one coordinate system can be defined in terms of the components of another coordinate system.

3) According to principal of conservation of linear momentum, the stress tensor in every point of selected infinitesimal body satisfies the equilibrium equations (it will be covered in this subsection).

4) The stress definition covered in this thesis is Cauchy stress tensor which is used for stress analysis involving small deformations. There are other stress definitions (e.g. Piola-Kirchhoff stress tensor) in the literature used in other material constitutive behaviors (e.g. finite deformations).
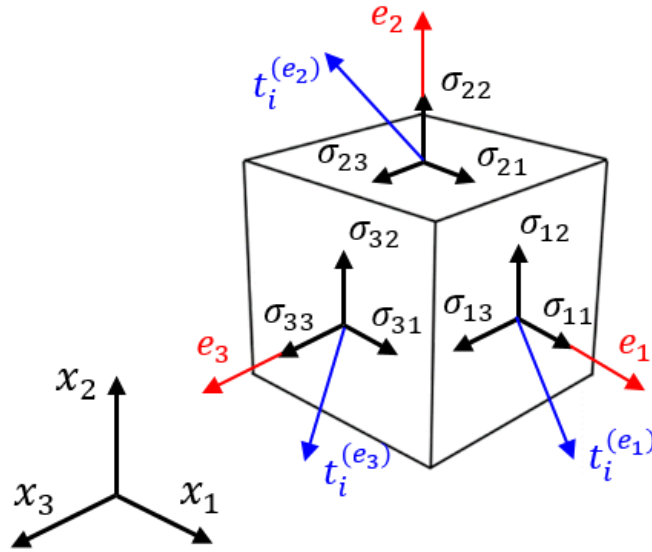
Figure 6: Illustration of stress tensor and stress vector of an infinitesimal cubic element whose face normals coincide with the directions of sample frame x_1, x_2 and x_3.

In Figure 6, it can be seen that stress vector does not necessarily coincide with the directions of sample frame. When the components of the stress vectors coincide with the directions of sample frame, we find the principal stress state where off diagonal stress components in stress tensor disappear. Calculation of principal stresses play a major role in several materials phenomena. Principal stress state and the calculation of principal stresses are not covered in this dissertation; however, readers can read through a solid mechanics reference to get a full understanding of these concepts.

3.1.2 Strain

In this subsection, the deformation of a solid body will be studied in terms of strain. Even though in classical mechanics, a body under forces is assumed rigid, there is no such thing as rigidity in reality. If there are any forces acting on a selected body, it goes under deformation up to a certain extent (depending on the magnitude and direction of the force).

34

The rigidity can only be treated as an assumption if the rigid body approximations are within the precision desired for calculation of body motions.
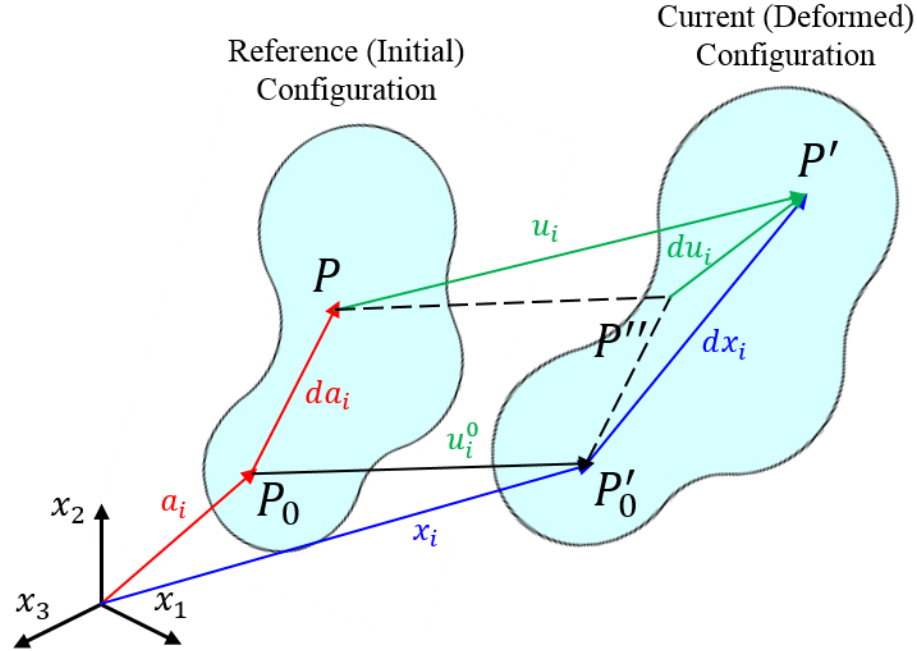
Figure 7: A hypothetical body going under deformation. On the left is the reference (initial) configuration and on the right is the current (deformed) configuration.

Deformation can be regarded as the mapping of a body from a reference configuration (or initial) at time t to a current configuration at time $t + \Delta t$ (or deformed configuration). The illustration of the deformation can be seen in Figure 7. a_i and da_i determine the locations of two material points P_0 and P in initial configurations. On the other hand, x_i and dx_i determine the locations of the material points P_0' and P' in current configuration. From these definitions, we can also state that the points at P_0 and P in initial configuration are deformed to points P_0' and P' in current configuration. Hence, the displacement of point P_0 can be written as:

$$u_i^0 = x_i - a_i \tag{37}$$

Similar expressions can be written for the other points (i.e. P'). For an infinitesimal deformation, the displacements around point P_0 can be written as a Taylor expansion:

$$u_i = u_i^0 + \frac{\partial u_i}{\partial x_i} dx_j + \frac{1}{2} \frac{\partial u_i}{\partial x_i \partial x_k} dx_j dx_k + \cdots \tag{38}$$

Under the assumption of infinitesimal deformations, it can be said that the derivative in the second monomial of right hand side of Eq. (38) is very small. Hence, the second order derivative and higher order derivatives (terms that follow the second monomial) will be even smaller and they can be neglected. From here, the first derivative can be decomposed into symmetric and antisymmetric part:

$$u_i = u_i^0 + \frac{1}{2}\left(\frac{\partial u_i}{\partial x_j} + \frac{\partial u_j}{\partial x_i}\right) dx_j + \frac{1}{2}\left(\frac{\partial u_i}{\partial x_j} - \frac{\partial u_j}{\partial x_j}\right) dx_j dx_k \tag{39}$$

Then, the infinitesimal strain tensor can be defined as:

$$\varepsilon_{ij} = \frac{1}{2}\left(\frac{\partial u_i}{\partial x_j} + \frac{\partial u_j}{\partial x_i}\right) \tag{40}$$

The strain tensor ε_{ij} is also called Cauchy strain tensor in several references. It can be written in matrix format as below:

$$\varepsilon_{ij} = \begin{bmatrix} \varepsilon_{11} & \varepsilon_{12} & \varepsilon_{13} \\ \varepsilon_{21} & \varepsilon_{22} & \varepsilon_{23} \\ \varepsilon_{31} & \varepsilon_{32} & \varepsilon_{33} \end{bmatrix} \tag{41}$$

where the components on the diagonal are normal strain components, while the off diagonal components are called shear strain components.

The derivations explained in this content are based on variables defined in terms of coordinates in current configuration (or spatial coordinates). It should be reminded that all of the variables and material points in Figure 7 can be defined in terms of coordinates in

reference configuration (or material coordinates). If the derivation included here is done without the assumption of infinitesimal deformation, we can reach two different strain tensor definitions, Lagrangian and Eulerian strain tensor. Lagrangian strain tensor defines the state of strain in terms of material coordinates, while Eulerian strain tensor defines the state of strain in spatial coordinates. When the higher order derivatives in Eq. (38) are neglected under the assumption of infinitesimal deformation, Lagrangian and Eulerian strain tensors become the same and lead to Cauchy strain tensor. The assumption of removing higher order derivatives made in reaching Eq. (39) from Eq. (38) is only valid for infinitesimal deformations. When the deformations are not infinitesimal, one must employ Lagrangian or Eulerian strain tensor definitions to accommodate the accurate deformations (i.e. finite deformations). The derivation of these strain tensors are not included here since finite deformations are beyond the scope of this dissertation.

There are a few points that can be made about the abovementioned assumptions and the Cauchy strain tensor:

1) The strain tensor is the symmetric part of the first derivative in Eq. (38). Hence, the strain tensor is a symmetric tensor like the stress tensor ($\varepsilon_{ij} = \varepsilon_{ji}$).

2) The second parenthesis on the right hand side of Eq. (39) is the antisymmetric part of the first derivative in Eq. (38) and it is called infinitesimal rotation tensor, ω_{ij}. It accounts for the rigid body rotations.

3) The normal strain components represent the change of length per unit length of a line element initially parallel to the selected coordinate direction.

The arguments about principal stresses given in previous subsection can be made for strain tensor as well. If the coordinates axes coincide with principal directions of a state of strain,

37

then we reach principal strain tensor where off diagonal components (i.e. shear strains) vanish.

3.1.3 Governing Equations of Linear Elasticity

There are several factors that affect the relationship between deformation of the body and the forces acting on it such as loading rate, load history, temperature, etc. In most of the loading conditions, after the deformation the body cannot recover to its original shape. However, if the deformations are infinitesimal and temperature has negligible effect, then the relationship between stress and strain is covered in Theory of Linear Elasticity. Governing equations of linear elasticity are based on three tensorial partial differential equations; equilibrium conditions, strain-displacement equation and elastic constitutive equations. Beyond this point, all deformations are assumed infinitesimal and the temperature has no effect on them.
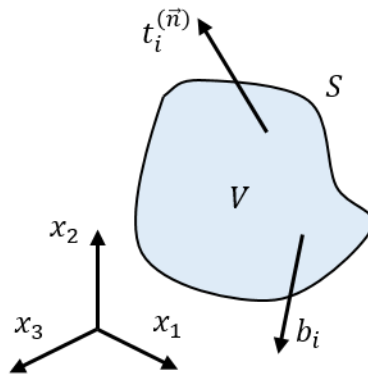
Figure 8: A hypothetical body in equilibrium under body forces b_i and surface tractions $t_i^{(\vec{n})}$.

First governing equation is equilibrium conditions for zero acceleration. Consider the body in Figure 8 with a volume V and surface S is subjected to surface tractions, $t_i^{(n)}$ and body forces, b_i. If this body is in equilibrium (or has zero acceleration), then the sum

of all forces acting on the body is zero. From the equations of motion, the sum of all forces can be written in terms of body forces and surface tractions:

$$\sum F_i = \int_V b_i dV + \int_S t_i^{(n)} dS = 0 \tag{42}$$

The second integral on the right hand side of Eq. (42) is an integral over the surface S and can be written as an integral over the volume V by using Gauss theorem:

$$\sum F_i = \int_V b_i dV + \int_S \sigma_{ij} n_j dS = \int_V b_i dV + \int_V \sigma_{ij,j} dV = 0 \tag{43}$$

At this stage, both of the integrals on the right hand side are volume integrals. Hence the total forces can be shortly written as:

$$\sum F_i = \int_V (\sigma_{ij,j} + b_i) dV = 0 \tag{44}$$

From here equilibrium conditions can be written as:

$$\sigma_{ij,j} + b_i = 0 \tag{45}$$

Second governing field equation is strain-displacement equations for infinitesimal deformations and it can be written as:

$$\varepsilon_{ij} = \varepsilon_{ij} = \frac{1}{2}\left(\frac{\partial u_i}{\partial x_j} + \frac{\partial u_j}{\partial x_i}\right) \tag{46}$$

It can be seen in Eq. (46) that there are 6 strain-displacement equations where each accounts for one strain component in the strain tensor written in matrix format in Eq. (41). The derivation and properties of these equations are summarized in previous subsection.

Third governing field equation is the linear elastic constitutive equation (also known as Hooke's Law). It is expressed as:

$$\sigma_{kl} = C_{ijkl}\varepsilon_{kl} \tag{47}$$

where C_{ijkl} is the elastic stiffness tensor and relates the state of strain to state of stress. There are 2 important aspects of the linear elastic constitutive relationship shown in Eq. (47).

1) There is one-to-one correspondence between the states of stress and strain. In other words, there is only one unique solution that satisfies the governing field equations of linear elasticity. Hence if the state of stress is known, the calculation of strain is trivial.

2) All of the governing field equations are indeed linear due to having only first order terms in the dependent variables and derivatives. Thus, the components of strain and stress can be calculated independently by superposing the loads acting on the body. This is called superposition principle and it plays an important role in building elastic localization linkages for any arbitrary loading condition.

Elastic stiffness tensor is a fourth rank tensor with 81 components where each index (i.e. *i, j, k, l*) runs from 1 to 3. However, not all 81 components are independent. The symmetries of fourth rank elastic stiffness tensor can be written as:

$$C_{ijkl} = C_{jikl} = C_{ijlk} = C_{klij} \tag{48}$$

With these symmetries, the number of independent elastic stiffness components become 21 for a generalized anisotropic material system. Since we have only 21 independent

components, the constitutive equation in Eq. (47) can be written in matrix format by using Voigt notation:

$$
\begin{bmatrix} \sigma_1 \\ \sigma_2 \\ \sigma_3 \\ \sigma_4 \\ \sigma_5 \\ \sigma_6 \end{bmatrix} = \begin{bmatrix} C_{11} & C_{12} & C_{13} & C_{14} & C_{15} & C_{16} \\ C_{12} & C_{22} & C_{23} & C_{24} & C_{25} & C_{26} \\ C_{13} & C_{23} & C_{33} & C_{34} & C_{35} & C_{36} \\ C_{14} & C_{24} & C_{34} & C_{44} & C_{45} & C_{46} \\ C_{15} & C_{25} & C_{35} & C_{45} & C_{55} & C_{56} \\ C_{16} & C_{26} & C_{36} & C_{46} & C_{56} & C_{66} \end{bmatrix} \begin{bmatrix} \varepsilon_1 \\ \varepsilon_2 \\ \varepsilon_3 \\ \varepsilon_4 \\ \varepsilon_5 \\ \varepsilon_6 \end{bmatrix}
\tag{49}
$$

where stress and strain components with indices 4, 5 and 6 correspond to stress and strain components with Einstein notation 23, 13 and 12, respectively. It should be kept in mind that the components ε_4, ε_5 and ε_6 are engineering strains γ_{23}, γ_{13} and γ_{12} where:

$$
\gamma_{23} = 2\varepsilon_{23} \ , \ \ \gamma_{13} = 2\varepsilon_{13} \ , \ \ \gamma_{23} = 2\varepsilon_{23}
\tag{50}
$$

The symmetry mentioned in Eq. (48) for elastic stiffness tensor is a symmetry that defines the stiffness of a generalized anisotropic material. However, most materials exhibit a symmetry in their crystal structure. The symmetry in crystal structure defines the number of independent components in fourth rank elastic tensor. There are several crystal symmetries such as isotropic, cubic, hexagonal (transversely isotropic), orthotropic, monoclinic symmetries. In this thesis, we are only interested in isotropic, cubic and hexagonal symmetries since all of the case studies included material systems with one of these crystal symmetries. However, the concepts are completely extendable to material systems with other crystal symmetries as well.

3.1.3.1 Isotropic Symmetry

Isotropic materials do not depend on the arrangement of crystal structure. When there is no dependence on coordinate system, the number of independent elastic stiffness tensor components reduce to only 2. The Voigt notation of isotropic elastic stiffness tensor can be seen below:

$$\begin{bmatrix} C_{11} & C_{12} & C_{12} & 0 & 0 & 0 \\ C_{12} & C_{11} & C_{12} & 0 & 0 & 0 \\ C_{12} & C_{12} & C_{11} & 0 & 0 & 0 \\ 0 & 0 & 0 & \dfrac{(C_{11} - C_{12})}{2} & 0 & 0 \\ 0 & 0 & 0 & 0 & \dfrac{(C_{11} - C_{12})}{2} & 0 \\ 0 & 0 & 0 & 0 & 0 & \dfrac{(C_{11} - C_{12})}{2} \end{bmatrix} \tag{51}$$

As an example, tungsten is a metal which exhibits isotropic symmetry. Even though the main focus is on building localization relationships for polycrystalline aggregates in this thesis, two-phase isotropic composites will be used for demonstration of fundamental aspects of calibration aspects.

3.1.3.2 Cubic Symmetry

Cubic materials have three mutually orthogonal planes of reflection symmetry and 90-degree rotation symmetry with respect to those planes. The fourth rank elastic stiffness tensor has only 3 independent components and it can be written as:

$$\begin{bmatrix} C_{11} & C_{12} & C_{12} & 0 & 0 & 0 \\ C_{12} & C_{11} & C_{12} & 0 & 0 & 0 \\ C_{12} & C_{12} & C_{11} & 0 & 0 & 0 \\ 0 & 0 & 0 & C_{44} & 0 & 0 \\ 0 & 0 & 0 & 0 & C_{44} & 0 \\ 0 & 0 & 0 & 0 & 0 & C_{44} \end{bmatrix} \tag{52}$$

As an example, copper is a metal which exhibits cubic crystal structure. Case studies in this thesis will heavily involve cubic metals.

3.1.3.3 Hexagonal (Transversely Isotropic) Symmetry

Hexagonal crystal structure has one plane of symmetry and one axis of symmetry perpendicular to the plane of symmetry. The number of independent elastic stiffness tensor components reduce to 5. The Voigt notation of hexagonal elastic stiffness tensor can be seen below:

$$\begin{bmatrix} C_{11} & C_{12} & C_{13} & 0 & 0 & 0 \\ C_{12} & C_{11} & C_{13} & 0 & 0 & 0 \\ C_{13} & C_{13} & C_{33} & 0 & 0 & 0 \\ 0 & 0 & 0 & C_{44} & 0 & 0 \\ 0 & 0 & 0 & 0 & C_{44} & 0 \\ 0 & 0 & 0 & 0 & 0 & \dfrac{(C_{11} - C_{12})}{2} \end{bmatrix} \tag{53}$$

Magnesium is an example for a material system with a hexagonal crystal structure. In one of the case studies, hexagonal crystal structure will be included in localization relationships.

3.2 Homogenization Theory

The mechanical response of material systems with multiple hierarchical length scales with significant heterogeneities has been addressed rigorously in prior literature

using generalized composite and homogenization theories [28, 29, 40, 54, 58-65]. Inherent to these theories is the concept of a scale-bridging localization tensor that relates the local fields of interest at the microscale to the macroscale (typically averaged) fields. For example, the fourth-rank localization tensor for elastic deformation, $\boldsymbol{a}$, can be defined to relate the local elastic strain at any location of interest in the microstructure to the macroscale strain imposed on the composite material system as:

$$\boldsymbol{\varepsilon}(x) = \boldsymbol{a}(x)\langle\boldsymbol{\varepsilon}(x)\rangle \tag{54}$$

$$\boldsymbol{a}(x) = (\boldsymbol{I} - \langle\boldsymbol{\Gamma}(x, x')\boldsymbol{C}'(x')\rangle + \langle\boldsymbol{\Gamma}(x, x')\boldsymbol{C}'(x')\boldsymbol{\Gamma}(x', x'')\boldsymbol{C}'(x'')\rangle - \cdots) \tag{55}$$

In Eq. (55), $\boldsymbol{I}$ is the fourth-rank identity tensor, $\boldsymbol{C}'(x)$ is the deviation in the local elastic stiffness at spatial location $\mathbf{x}$ with respect to that of a selected reference medium, $\boldsymbol{\Gamma}$ is a symmetrized derivative of the Green's function defined using the elastic properties of a selected reference medium [28, 54, 66], and $\langle\,\rangle$ brackets denote an ensemble average over a representative volume element (RVE) of the material microstructure.

The main problem in Eq. (55) lies in the localization tensor. This term depends on the reference medium, rendering it very difficult to calculate analytically. There are certain iterative approaches which uses an initial guess of strain field and a symmetrized derivative of Green's function, $\boldsymbol{\Gamma}$ based on specific bounds of the selected reference medium. Even though the iterative methods based on the Green's function established its success in predicting local response fields [62, 63, 67], it is highly important that an approach which does not require the analytical calculation of influence functions has to be developed for computationally efficient localization relationships. In the next section, the derivation to formulate these relationships is shown in detail.

3.3 Derivation of Localization Relationships

As stated before, the higher order theory has to be implemented for more accurate estimates for effective properties. The theory involves the correlations between the local states at different locations of the reference medium. By following the perturbation expansion given in Eq. (54) and (55), we can decompose a local strain field into two parts as:

$$\boldsymbol{\varepsilon}(x) = \bar{\boldsymbol{\varepsilon}} + \boldsymbol{\varepsilon}'(x) \quad , \quad \bar{\boldsymbol{\varepsilon}}' = \mathbf{0} \tag{56}$$

where $\bar{\boldsymbol{\varepsilon}}$ is the average strain and $\boldsymbol{\varepsilon}'$ represents the strain fluctuations from the average strain. From this additive decomposition in Eq. (56), an expression similar to Eq. (54) can be written as below:

$$\boldsymbol{\varepsilon}'(x) = \boldsymbol{a}(x)\bar{\boldsymbol{\varepsilon}} \quad , \quad \bar{\boldsymbol{a}} = \mathbf{0} \tag{57}$$

The difference between the Eq. (54) and (57) is the lack of average terms on the left hand side in Eq. (57). Indeed, these expressions are in accordance with general effective stiffness equation. If a selected volume element has an average strain $\langle \boldsymbol{\varepsilon}(x) \rangle$ resulting from a heterogeneous strain distribution $\boldsymbol{\varepsilon}(x)$, then the average strain corresponds to an average stress distribution, $\langle \boldsymbol{\sigma}(x) \rangle$ through an effective stiffness tensor C^{eff}:

$$\bar{\boldsymbol{\sigma}} = \boldsymbol{C}^{eff}\bar{\boldsymbol{\varepsilon}} \tag{58}$$

Expressions similar to Eq. (58) are widely used to calculate effective properties for several phenomena such as thermal conduction [68], electrical conduction [69], permeability [70], etc.

Same additive decomposition in Eq. (56) can be repeated for Eq. (58) and it can be shown that average stress is equal to the average of tensorial product of local strain and stiffness:

$$\overline{\sigma} = C^{eff}\overline{\varepsilon} = \overline{C\varepsilon} \tag{59}$$

Readers should keep in mind that for clarity, the functional dependence of the spatial location are not shown explicitly. The definition on the right side of Eq. (59) can be decomposed according to average strain and strain fluctuations:

$$\overline{C\varepsilon} = \overline{C(\varepsilon' + \overline{\varepsilon})} = \overline{C\varepsilon'} + \overline{C\overline{\varepsilon}} \tag{60}$$

Then, we can insert the definition in Eq. (57) to the right hand side of Eq. (60):

$$\overline{C\varepsilon'} + \overline{C\overline{\varepsilon}} = \overline{Ca\overline{\varepsilon}} + \overline{C\overline{\varepsilon}} \tag{61}$$

At this stage all terms in the right hand side of the Eq. (61) have $\overline{\varepsilon}$. If we cancel this term from both average stress definition and Eq. (57), then we can find:

$$\overline{\sigma} = C^{eff}\overline{\varepsilon} = \overline{Ca}\overline{\varepsilon} + \overline{C}\overline{\varepsilon} \ \Rightarrow \ C^{eff} = \overline{Ca} + \overline{C} \tag{62}$$

As the next step, we apply the additive decomposition to local stiffness as well to get reference and fluctuation terms.

$$C = C(x) = C^r + C'(x) \tag{63}$$

If we take the average of both sides in Eq. (63), the average of stiffness fluctuations can be found as:

$$\overline{C}' = \overline{C} - C^r \tag{64}$$

Then, by substituting Eq. (64) into Eq. (62), the effective stiffness can be found as:

$$\boldsymbol{C}^{eff} = \overline{\boldsymbol{C}\boldsymbol{a}} + \overline{\boldsymbol{C}}' + \boldsymbol{C}^r \tag{65}$$

It is shown in Eq. (65) that a localization tensor is required to find an effective property by using perturbation expansions. A derivative of this localization tensor will be the integral part of the localization relationships used in this thesis.

To derive the localization relationships, we go back to stress-strain relationship in Eq. (59) and additive decompositions applied to it in Eq. (60). For a framework that is comprehensive for any elastic material (isotropic or anisotropic), we include the indices of all tensors. The right hand side of the equation can be rewritten as:

$$\sigma_{ij} = \left(C^r_{ijkl} + C'_{ijkl} \right)\left(\bar{\varepsilon}_{kl} + \varepsilon'_{kl} \right) \tag{66}$$

$$\sigma_{ij} = C^r_{ijkl}\bar{\varepsilon}_{kl} + C^r_{ijkl}\varepsilon'_{kl} + C'_{ijkl}\bar{\varepsilon}_{kl} + C'_{ijkl}\varepsilon'_{kl} \tag{67}$$

Now like the standard elastic constitutive behavior in Eq. (47), this relationship must meet the equilibrium conditions (see Eq. (46)) as well. If we apply the divergence operation on expression in Eq. (67) to meet equilibrium conditions, we get:

$$\sigma_{ij,j} = C^r_{ijkl}\varepsilon'_{kl,j} + C'_{ijkl,j}\bar{\varepsilon}_{kl} + \left(C'_{ijkl}\varepsilon'_{kl} \right)_{,j} = 0 \tag{68}$$

Attention must be paid to the expression in Eq. (68). The first monomial in Eq. (67) became zero after the derivative due to the fact that both variables are constant terms. The second monomial had 2 variables with only the first one being a constant term, hence leading to a derivative on the second term and third monomial is vice versa. On the other hand, fourth monomial had the derivative outside the parenthesis as neither of the variables are constant.

If we take the last two monomials in Eq. (68) as the body forces, F_i, the expression can be rewritten as:

$$C^r_{ijkl}\varepsilon'_{kl,j} + F_i = 0 \tag{69}$$

$$F_i = C'_{ijkl,j}\bar{\varepsilon}_{kl} + \left(C'_{ijkl}\varepsilon'_{kl}\right)_{,j} \tag{70}$$

The approach that will be derived from the above equations is based on the definition of strain in terms of displacements. We can write ε'_{kl} terms in terms of displacement u:

$$\varepsilon'_{kl} = \frac{1}{2}\left(u'_{k,l} + u'_{l,k}\right) \tag{71}$$

where (,) represents the partial derivative with respect to distance. Then, Eq. (69) becomes:

$$\frac{C^r_{ijkl}\left(u'_{k,l} + u'_{l,k}\right)_{,j}}{2} + F_i = 0 \tag{72}$$

Now that there are displacement terms, we can have a strategy involving Green's functions in the solution of u'_i. To do this, first we treat Eq. (72) as a nonhomogeneous partial differential equation for unit body force. Then, we solve for displacement u'_i by a convolution of Green's function and body force per unit volume. The strategy can be summarized as:

$$C^r_{ijkl}G_{km,lj}(x - x') + \delta(x - x')\delta_{im} = 0 \tag{73}$$

$$u'_k(x) = \int_V G_{ki}(x - x')F_i(x')dx' \tag{74}$$

where G_{ki} is the Green's function. An illustration of Green's function is given in Figure 9. Green's function is related to the displacement u'_k at location x due to the application of a body force F_i at location x'. Eq. (74) is the fundamental Green's function solution, G_{km} as the component k of the displacement field at location x.
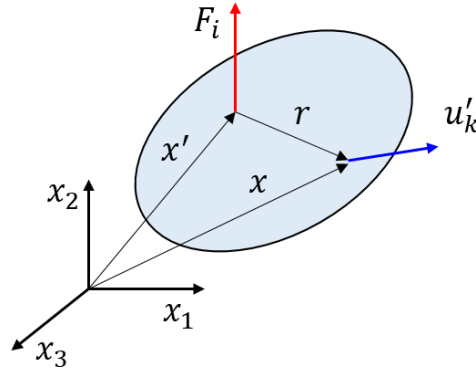
Figure 9: Illustration of Green's function

The expression in Eq. (74) can be reformulated with an integral over $r = x - x'$ and the displacements given in Eq. (71) can be expressed in terms of Green's function and body forces:

$$u'_k(x) = \int_V G_{ki}(r)F_i(x')dx' \tag{75}$$

$$u'_l(x) = \int_V G_{li}(r)F_i(x')dx' \tag{76}$$

If we substitute the expression for F_i (see Eq. (70)) into Eq. (75) and (76), displacements can be rewritten as:

$$u'_k(x) = \int_V G_{ki}(r)\left[C'_{ijmn}(x')\bar{\varepsilon}_{mn} + \left(C'_{ijmn}(x')\varepsilon'_{mn}(x')\right)_{,j}\right]dx' \tag{77}$$

$$u'_l(x) = \int_V G_{li}(r) \left[C'_{ijmn}(x')\bar{\varepsilon}_{mn} + \left(C'_{ijkl}(x')\varepsilon'_{mn}(x') \right)_{,j} \right] dx' \qquad (78)$$

These displacement expressions can be differentiated with respect to x and then can be inserted in Eq. (71).

$$\varepsilon'_{kl} = \int_V \frac{G_{ki,l}(r) + G_{li,k}(r)}{2} \left[C'_{ijmn,j}(x')\bar{\varepsilon}_{mn} + \left(C'_{ijmn}(x')\varepsilon'_{mn}(x') \right)_{,j} \right] dx' \qquad (79)$$

From here the localization tensor $\boldsymbol{a}_{klmn}$ can be extracted by simply substituting Eq. (54) into Eq. (79).

$$\boldsymbol{a}_{klmn}(x) = \int_V \frac{G_{ki,l}(r) + G_{li,k}(r)}{2} \left[C'_{ijmn}(x') + C'_{ijmn}(x')a_{pqmn}(x') \right]_{,j} dx' \qquad (80)$$

The Green's function in Eq. (80) goes to infinity as $x - r$ approach to zero. Hence, the integral has a principal value around $x - r = 0$. This integral can be evaluated with integration by parts. However due to the singularity, the integration is done over a volume between two spherical surfaces corresponding to $x - r = 0$ and $x - r = \infty$.

$$\boldsymbol{a}_{klmn}(x) = \left[\int_S \frac{G_{ki,l}(r) + G_{li,k}(r)}{2} \left[C'_{ijmn}(x') \right. \right.$$
$$\left. \left. + C'_{ijpq}(x')\boldsymbol{a}_{pqmn}(x') \right] n_j dS \right]_{r \to 0}^{r \to \infty} \qquad (81)$$
$$- \int_{\tilde{V}} \frac{G_{ki,lj}(r) + G_{li,kj}(r)}{2} \left[C'_{ijmn}(x') + C'_{ijpq}(x')\boldsymbol{a}_{pqmn}(x') \right] dx'$$

If we consider only the terms without localization tensors in Eq. (81), the weak contrast expansion can be written as:

$$-\boldsymbol{\Gamma C'} = \left[\int_S \frac{G_{ki,l}(r) + G_{li,k}(r)}{2}[\boldsymbol{C'}_{ijmn}(x')]n_j dS\right]_{r\to 0}^{r\to\infty}$$

$$-\int_{\widetilde{V}} \frac{G_{ki,lj}(r) + G_{li,kj}(r)}{2}[\boldsymbol{C'}_{ijmn}(x')] dx' \tag{82}$$

The expression above can be summarized as:

$$\boldsymbol{\Gamma}_{klij}(r) = \boldsymbol{E}_{klij}(r)\delta(r) + \boldsymbol{I}^\infty_{klij}\delta(r) + \boldsymbol{\Phi}_{klij}(r) \tag{83}$$

where $\boldsymbol{\Phi}_{klij}$ are the Green's function terms. $\boldsymbol{E}_{klij}$ and $\boldsymbol{I}^\infty_{klij}$ are the contributions from surface terms. These terms are expressed as below:

$$\boldsymbol{\Phi}_{klij} = \frac{G_{ki,lj}(r) + G_{li,kj}(r)}{2} \tag{84}$$

$$\boldsymbol{E}_{klij} = \lim_{r\to 0}\left(\int_S \frac{G_{ki,l}(r) + G_{li,k}(r)}{2}n_j dS\right) \tag{85}$$

$$\boldsymbol{I}^\infty_{klij} = \lim_{r\to\infty}\left(\int_S \frac{G_{ki,l}(r) + G_{li,k}(r)}{2}[\boldsymbol{C'}_{ijmn}(x-r)]n_j dS\right) \tag{86}$$

The intermediate steps and detailed information about the integration by parts operation can be found in [54]. If we plug in $\boldsymbol{\Gamma}_{klij}$ to expression in Eq. (81), we get:

$$\boldsymbol{a}_{klmn}(\boldsymbol{x}) = -\int_V \boldsymbol{\Gamma}_{klij}(r)[\boldsymbol{C'}_{ijmn}(x') + \boldsymbol{C'}_{ijpq}(x')\boldsymbol{a}_{pqmn}(x')]dx' \tag{87}$$

We can substitute the entire expression to the last term recursively to reach the general expression for localization tensor. Readers should be reminded as we recursively insert the

expression to itself, we reach the higher order localization terms and they account for the nonlinearities in series expansion.

$$a_{klmn}(x) = -\int_V \boldsymbol{\Gamma}_{klij}(r)\left[\boldsymbol{C}'_{ijmn}(x') + \boldsymbol{C}'_{ijpq}(x')\right.$$

$$\left(-\int_V \boldsymbol{\Gamma}_{pquv}(r')\left[\boldsymbol{C}'_{uvmn}(x'') + \boldsymbol{C}'_{uvrs}(x'')\int_V \dots\right]dx''\right)\right]dx' \tag{88}$$

Now, we can use the localization tensor back in Eq. (57) to reach the general expression of perturbation strain.

$$\varepsilon'_{kl} = -\int_V \boldsymbol{\Gamma}_{klij}(r)\boldsymbol{C}'_{ijmn}(x')\bar{\varepsilon}_{mn}dx'$$

$$-\int_V \int_V \boldsymbol{\Gamma}_{klij}(r)\boldsymbol{C}'_{ijpq}(x')\boldsymbol{\Gamma}_{pquv}(r')\boldsymbol{C}'_{uvmn}(x')\bar{\varepsilon}_{mn}dx''dx' + \cdots \tag{89}$$

This expression is a sum of series that goes to infinity due to the perturbation expansions and it is very close to localization relationships that we are seeking. Eq. (89) can be transformed into a more computationally useful form by taking advantage of the concept of spatially resolved microstructure function $m(x, n)$ [71] that reflects the probability density associated with finding the local state n (to within an invariant measure dn) at the spatial location x (note that $m(x, n)dn$ reflects the corresponding probability). The local state identifies the specific combination of local features (including phase identifiers, elemental compositions, crystal lattice orientations, etc.) needed to uniquely define the relevant local physical properties at the spatial location x. Furthermore, the complete set of all distinct local states that are possible in a given material system is referred to as the local state space, denoted by H (i.e., $n \in H$). From here the first step is to introduce local

microstructure descriptor to the expression. We start by describing the perturbation stiffness as:

$$\boldsymbol{C}'(x - r) = \int_H \boldsymbol{C}'(n)\, m(x - r, n)dn \tag{90}$$

where $\boldsymbol{C}'(n)$ represents the deviation in elastic stiffness of the local state n from the effective stiffness. The summation (or integral in this case) of the perturbation stiffness term that comes from each local state bin contributes to total perturbation stiffness at spatial location x (left hand side of Eq. (90)).

With the introduction of Eq. (90), we removed the dependence of stiffness term to spatial location x and transferred it to microstructure function. We also know that symmetrized derivative of Green's function only depends on the relative distance r. From these two arguments, we can define a new term called influence function, $\boldsymbol{\alpha}$.

$$\boldsymbol{\alpha}(r, n) = -\boldsymbol{\Gamma}(r)\boldsymbol{C}'(n) \tag{91}$$

$$\boldsymbol{\alpha}(r, r', n, n') = -\boldsymbol{\Gamma}(r)\boldsymbol{C}'(n)\boldsymbol{\Gamma}(r')\boldsymbol{C}''(n') \tag{92}$$

where $\boldsymbol{\alpha}(n, r)$ and $\boldsymbol{\alpha}(n, n', r, r')$ in Eq. (91) and (92) are first order and second order influence functions, respectively. Higher order influence functions can be defined in a similar manner. Now if we plug these terms into Eq. (89) and remove the indices for clarity, we reach the final form of localization relationships:

$$\varepsilon'(x) = \left(\int_V \int_H \boldsymbol{\alpha}(r,n)\, m(x-r,n)\, dn dr \right.$$

$$\left. + \int_V \int_V \int_H \int_H \boldsymbol{\alpha}(r,r',n,n') m(x-r,n) m(x-r',n') dn dn' dr dr' + \cdots \right) \bar{\varepsilon}$$

(93)

The structure of Eq. (93) offers many computational advantages. First, the terms $\boldsymbol{\alpha}(r,n)$ and $\tilde{\boldsymbol{\alpha}}(r,r',n,n')$ are independent of the microstructure function. In other words, they capture the microstructure-independent physics governing the local response of a composite material [71]. Second, the terms in Eq. (93) can be calibrated to physics based models efficiently using discrete Fourier transforms (DFTs). Note that Eq. (93) represents an infinite series expansion of a highly nonlinear function, where each term of the series captures a linearized contribution from a specific spatial feature in the microstructure.

3.4 Generalized MKS Framework

Even though the expression in Eq. (93) defines the true localization relationships, it has two minor difficulties in employing it in P-S-P linkages. First difficulty stems from the fact that the expression is defined in continuous local state space and spatial domain. It has to be converted to a discrete format in such a way that it can be handled in digitized environment. The other difficulty is the way the local microstructure is included in the expression. A generic local microstructure descriptor must be defined to describe the localization relationships in Eq. (93) so that it can hold for several materials systems and physics based phenomena. For this manner, we seek a computationally efficient form of Eq. (93) using spectral representations.

3.4.1 Spectral Representations

Specifically, we seek representations of the following type for the influence functions $\boldsymbol{\alpha}(r, n)$ and microstructures functions $m(x, n)$ in Eq. (93).

$$m(x, n) = \sum_L \sum_s M_s^L Q_L(n) \chi_s(x) \tag{94}$$

$$\boldsymbol{\alpha}(r, n) = \sum_L \sum_t A_t^L(n) Q_L(n) \chi_t(r) \tag{95}$$

where L denotes the index for numbers defined in the local state space. In Eq. (94) and (95), $Q_L(n)$ is a suitably selected Fourier basis for functions defined on the local state space with the following orthonormal properties:

$$\int_H Q_L(n) Q_{L'}^*(n) dn = \frac{\delta_{LL'}}{N_L} \tag{96}$$

where the superscript * denotes a complex conjugate, $\delta_{LL'}$ is the Kronecker delta, and N_L is a constant that might depend on L. $\chi_s(x)$ in Eq. (94) defines an indicator basis which essentially tessellates the spatial domain into a uniform grid [71]. This function is defined such that its value is one for all points belonging to spatial bin s, and zero for all points outside. The choice of the indicator basis for the spatial variables in Eq. (94) is primarily motivated by the fact that it allows for the use of DFTs in carrying out the integrals in Eq. (93). Using the orthogonal properties of both bases, we can show:

$$M_s^L = \frac{N_L}{\Delta} \int_{H,V} m(x, n) Q_L^*(n) \chi_s(x) dn dx \tag{97}$$

$$\boldsymbol{A}_t^L = \frac{N_L}{\Delta} \int_{H,R} \boldsymbol{\alpha}(r,n) Q_L^*(n) \chi_t(r) dn dr \tag{98}$$

where Δ is the volume of the spatial bin. By using Eq. (97) and (98), the first order terms in expression in Eq. (93) can be rewritten in a new format:

$$\boldsymbol{p}_s = \left(\sum_t \int_H \left[\sum_L \boldsymbol{A}_t^L Q_L(n) \right] \left[\sum_{L'} M_{s+t}^{L'} Q_L(n) \right] dn \right) \langle \boldsymbol{p} \rangle \tag{99}$$

where $\boldsymbol{p}_s$ is the response at the spatial bin s and it can represent any response field based on the phenomena in interest (stress, strain, strain rate, composition field, etc). On the other hand, $\langle \boldsymbol{p} \rangle$ is average response field imposed on the macroscale. In all applications of MKS so far, $\langle \boldsymbol{p} \rangle$ is indeed the volume average of $\boldsymbol{p}_s$ over the entire spatial domain of the microstructure. In other words, the localization linkages in the expression shown in Eq. (96) are aimed at capturing the spatial distribution of the quantity imposed at the higher length scale. We can take the summations and terms which are independent of local state n outside the integral:

$$\boldsymbol{p}_s = \left(\sum_t \sum_L \boldsymbol{A}_t^L \sum_{L'} M_{s+t}^{L'} \int_H Q_L(n) Q_{L'}(n) dn \right) \langle \boldsymbol{p} \rangle \tag{100}$$

The integral in Eq. (100) is almost identical to Eq. (96), except the conjugate. If the basis functions have imaginary parts, then the second basis function needs a conjugate for the orthonormality condition (see Eq. (96)). This problem can be solved by taking the conjugate of the local microstructure descriptor expression in Eq. (94). This does not affect the expression as local microstructure descriptor, $m(x,n)$ is a real-valued function. With the conjugate, Eq. (100) can be rewritten as:

$$\boldsymbol{p}_s = \left(\sum_t \sum_L \boldsymbol{A}_t^L \sum_{L'} M_{s+t}^{L'*} \int_H Q_L(n) Q_{L'}^*(n) dn \right) \langle \boldsymbol{p} \rangle \tag{101}$$

If we plug Eq. (96) into (105), we obtain:

$$\boldsymbol{p}_s = \left(\sum_t \sum_L \sum_{L'} \boldsymbol{A}_t^L M_{s+t}^{L'*} \frac{\delta_{LL'}}{N_L} \right) \langle \boldsymbol{p} \rangle \tag{102}$$

Due to Kronecker delta, the terms can only be non-zero when $L = L'$. Hence, one of the summations can be removed and the localization relationships can be written in terms of first order terms:

$$\boldsymbol{p}_s = \left(\sum_t \sum_L \frac{\Delta}{N_L} \boldsymbol{A}_t^L M_{s+t}^{L'*} \right) \langle \boldsymbol{p} \rangle \tag{103}$$

The phenomena we are interested in is linear elastic deformation of polycrystalline aggregates. However, a discrete version of the expression in Eq. (93) was utilized for other physics based phenomena [23, 72]. From Eq. (103), the generalized localization relationships with higher order terms can be written as:

$$\boldsymbol{p}_s = \left(\sum_L \sum_t \frac{\Delta}{N_L} \boldsymbol{A}_t^L M_{s+t}^{L*} + \sum_L \sum_{L'} \sum_t \sum_{t'} \frac{\Delta^2}{N_L N_{L'}} \boldsymbol{A}_t^{LL'} M_{s+t}^{L*} M_{s+t+t'}^{L'} + \cdots \right) \langle \boldsymbol{p} \rangle \tag{104}$$

It is pointed that if $Q_L(n)$ were selected to be the indicator functions (i.e., a simple binning of the local state space), we would recover the simpler MKS formulation utilized in our prior studies involving multiphase composites [18, 22-25]. Likewise, if the local state was selected to the crystal lattice orientation and the Fourier basis was selected to the generalized spherical harmonics (GSH) [73], we would recover the localization relationships

formulation demonstrated for elastic deformations in single phase polycrystalline microstructures [20]. We believe that the formulation presented above is the most general and practical MKS formulation that will be applicable for a very broad range of advanced material systems.

3.4.2 Influence Functions

There have been essentially two main difficulties in the computation of the localization kernels defined in Eq. (55). The first difficulty stems from the fact that $\Gamma(r)$ (embedded in the localization kernels; see Eq. (55)) exhibits a singularity at $r = 0$. The second difficulty is that the convergence of the series is quite sensitive to the selection of the reference medium (e.g., [74]). These difficulties are handled with the generalized MKS framework shown in Eq. (104). A diagram of how influence functions are obtained and utilized for prediction of local response of a microstructure can be seen in Figure 10. The influence functions that constitute the knowledge in the MKS framework in Eq. (104) are fit to the results obtained from physics based models through regression methods. To calibrate the influence coefficients, first we need calibration microstructures. Calibration microstructures are usually generated from a wide range of volume fractions and topological features. These microstructures would serve as the microstructure function, M_s^L in Eq. (104). In other words, they are the input for the calibration. The selection of calibration microstructures will be explained in detail for the case studies presented in the next sections. Next, we run physics based models to produce the local response fields, $\boldsymbol{p}_s$ which serves as the output. The calibration of influence functions at this stage requires only regression methods. By simply calibrating them to the results obtained from physics based models, we overcome the problem of singularity encountered in $\Gamma(r)$.
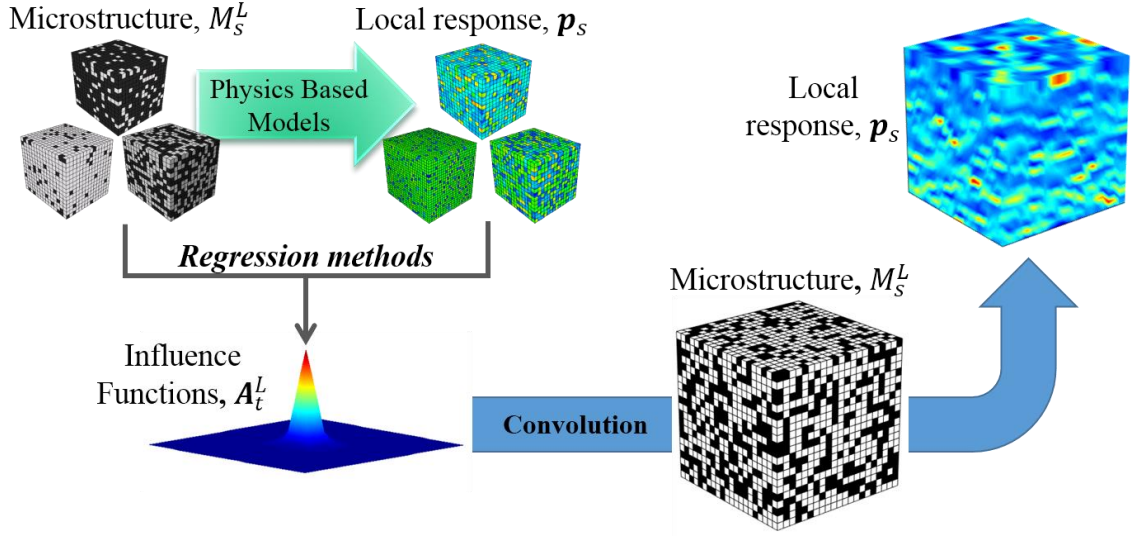
Figure 10: A diagram showing the main strategy in calibration of the influence functions and the prediction of response field through convolution of microstructure and influence functions

A_t^L and $A_t^{LL'}$ are referred to as first and second order influence functions, respectively. A_t^L captures the influence of local state L in spatial bin separated by a vector t from spatial bin s. On the other hand, $A_t^{LL'}$ capture the combined contribution of local state L and L' in the spatial bins separated by vectors t and t'. Higher order influence functions can be described in the same manner. Influence functions are on the same spatial grid as microstructure function. However, the most important difference of influence functions, A_t^L is that they are independent of the local microstructure descriptor (see that the subscript depends on the relative distance between points, t, not on the spatial location, s). This indicates that we do not need to define a reference localization tensor for each microstructure. From this perspective, one might consider the computational time required to execute physics based models as a disadvantage. However, since influence functions are completely independent of the local microstructure descriptor, the calibration process is a one-time computational cost. Once the influence functions are obtained, the response field

of any microstructure that can be realized in the material system in interest can be predicted in a very computationally efficient manner. Often times, MKS can achieve this task with orders of magnitude faster than physics based models. This will be demonstrated in detail with both of the case studies.

3.4.3 Workflow for Establishing Localization Linkages

The similarity of the generalized MKS framework presented here to the versions in prior localization work [18, 19, 24, 25, 27] suggests the use of the same overall strategy for calibrating the influence functions (such as A_t^L) in Eq. (104). The overall workflow involved in building the MKS databases is shown in Figure 11 as a broadly usable template. This procedure involves four different main tasks (color coded in Figure 11) with several subtasks. These tasks involve: 1) generation of a calibration data set, 2) calibration of influence coefficients, 3) generation of validation data set and 4) validation of MKS. Although this template has been presented first time in [17], the protocols described in prior localization case studies essentially followed these protocols. The tasks shown in the template are explained in detail with case studies of MKS.
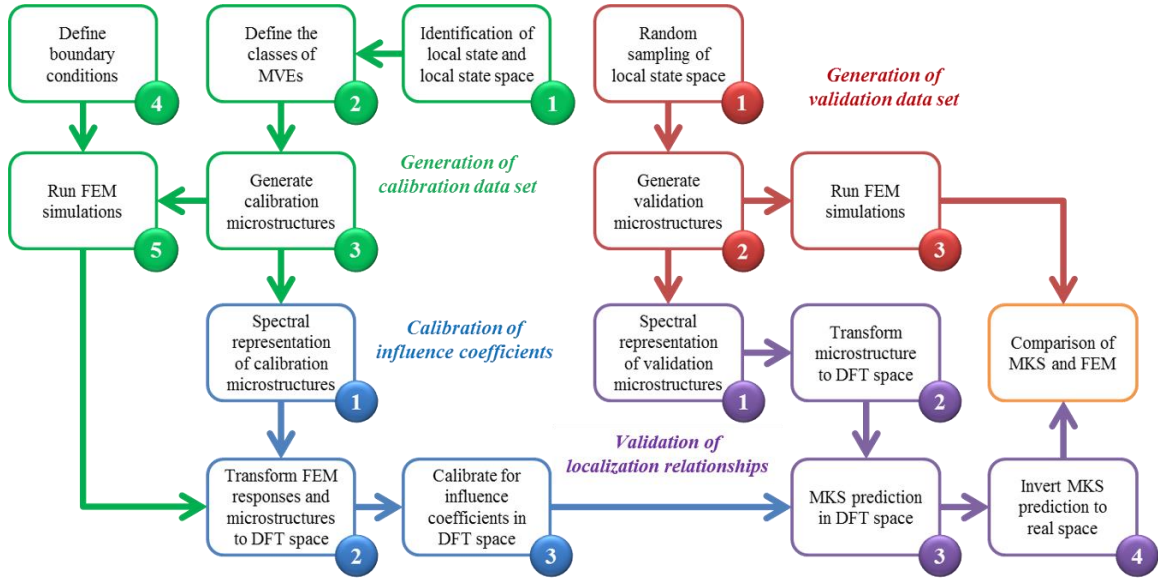
Figure 11: A suggested workflow template for establishing the generalized localization relationships formulation

3.5 MKS for Composite Materials

Even though the focus in this dissertation is to extend the MKS framework to polycrystalline aggregates, the details about the calibration of influence functions will be explained through composite materials. The localization relationships of MKS for composite materials were implemented in prior work for two-phase material systems [19, 23-25]. To obtain the suitable localization linkages for composite material systems, an appropriate Fourier basis function should be selected. The local microstructure descriptor and the procedure for calibration of influence coefficients are explained in this section.

3.5.1 Local Microstructure Descriptor for Multiphase Composites

Since we defined a generalized expression for MKS framework, we can recover the specific formulation for multiphase material system by selecting indicator functions as Fourier basis function, $\chi_L(n)$. If we plug the indicator function in Eq. (97), we obtain:

$$m(x,n) = \sum_L \sum_S M_S^L \chi_L(n) \chi_S(x) \tag{105}$$

$$M_S^L = \frac{N_L}{\Delta} \int_{H,V} m(x,n) \chi_L(n) \chi_S(x) dn dx \tag{106}$$

The local microstructure descriptor shown in Eq. (106) acts as a digital signal in discrete format and it denotes the probability of finding the local state L in the spatial bin s. Based on the definition made above, there are some constraints which are given as below:

$$\sum_L M_S^L = 1 \ , \ \ 0 \le M_S^L \le 1 \ , \ \ \sum_S M_S^L = V^L S \tag{107}$$

where S is the total number of spatial bins and V^L is the volume fraction of the local state L in the volume of interest. For a two-phase material system, the local state space has only 2 discrete local states (i.e. $L = \{1,2\}$). An example of M_S^L for two-phase materials system is shown in Figure 12. A grossly simplified 4×4 microstructure of a two-phase material system is shown at the left side. Spatial bins are numbered from 1 to 16 and each of them are fully occupied either by a white or gray phase. The white and gray phases are indicated by $L = 1$ and $L = 2$, respectively. If we take spatial bin 6 as an example, we can see that $M_6^1 = 1$ as the entire spatial bin is occupied by white phase. From this point, we can easily denote $M_6^1 = 0$. Similar approach is repeated for spatial bin 15 as well and it is shown in the right side of the Figure 12. This is an example of eigen-microstructure [75] where each spatial bin is fully occupied by a one discrete local state. However, the expressions given in Eq. (105) holds for non-eigen microstructures as well where the microstructure function can get fractional values.

1	5	9	13
2	**6**	10	14
3	7	11	**15**
4	8	12	16

Phases: $L = \{1,2\}$

$1 \rightarrow$ white, $2 \rightarrow$ gray

$$M_6^1 = 1 \qquad M_{15}^1 = 0$$
$$M_6^2 = 0 \qquad M_{15}^2 = 1$$
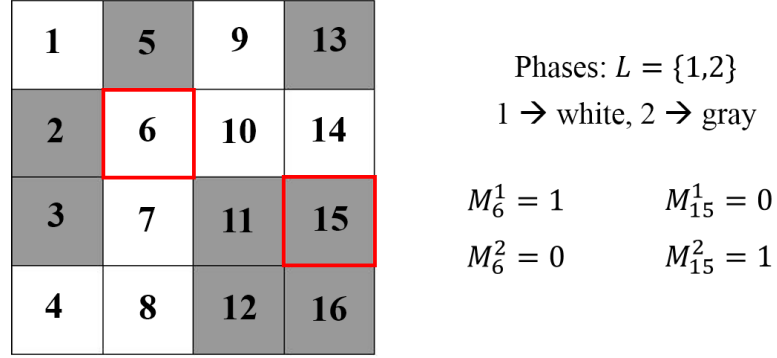
Figure 12: Visualization of local microstructure descriptor for a two-phase materials system

3.5.2 Calibration of Influence Functions

As it was mentioned before, the influence functions are calibrated to the results obtained from physics-based models through regression methods. To demonstrate the calibration procedure in detail, a one-dimensional microstructure is utilized and it can be seen in Figure 13. Each spatial bin is fully occupied either by a gray or white phase and the local microstructure values are given at the right hand side of the figure. The top values are for white phase and the bottom values are for gray phase.

| $s = 1$ | $s = 2$ | $s = 3$ |

M_1^1	M_2^1	M_3^1
1	0	1

M_1^2	M_2^2	M_3^2
0	1	0
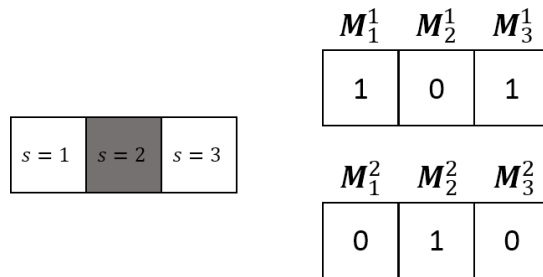
Figure 13: One dimensional microstructure of a two-phase material system. Local microstructure values for both phases are given at the right side of the microstructure

Now, let us write the expression in Eq. (104) for this microstructure in matrix format by considering only the first order terms and assuming the area of the spatial bin is 1.

$$
\begin{bmatrix} p_1 \\ p_2 \\ p_3 \end{bmatrix} = \begin{bmatrix} M_1^1 & M_2^1 & M_3^1 & M_1^2 & M_2^2 & M_3^2 \\ M_2^1 & M_3^1 & M_1^1 & M_2^2 & M_3^2 & M_1^2 \\ M_3^1 & M_1^1 & M_2^1 & M_3^2 & M_1^2 & M_2^2 \end{bmatrix} \begin{bmatrix} A_0^1 \\ A_1^1 \\ A_2^1 \\ A_0^2 \\ A_1^2 \\ A_2^2 \end{bmatrix} \tag{108}
$$

The influence functions at the right hand side of system of equations shown in Eq. (108) can be solved through regression methods. If we call the response, microstructure and influence function matrices as $\boldsymbol{P}, \boldsymbol{M}$ and $\boldsymbol{A}$, then the influence functions can be predicted based on Eq. (27) (i.e. OLS).

$$
\boldsymbol{A} = (\boldsymbol{M}^T \boldsymbol{M})^{-1} \boldsymbol{M} \boldsymbol{P} \tag{109}
$$

The difficulty in solving for influence functions in Eq. (109) lies in the inversion of $\boldsymbol{M}^T \boldsymbol{M}$. This matrix has a size of $(S \times L) \times (S \times L)$ where S is 3 and L is 2 for this microstructure. However, for a microstructure with a realistic size, this number increases dramatically. For a 3-D two-phase microstructure with a spatial grid of $S = 21 \times 21 \times 21 = 9261$ voxels, this number jumps to $S \times L = 21 \times 21 \times 21 \times 2 = 18522$. Even with a small size of volume element and two distinct local states, inverting this matrix is a computationally inefficient task. For a more computationally efficient approach, we solve for the influence functions in DFT space. First, we cast all 3 fields (response field, local microstructure and influence functions) in DFT space.

$$
\mathcal{M}_k^L = \mathfrak{I}(M_s^L) \; , \; \mathcal{A}_k^L = \mathfrak{I}(A_s^L) \; , \; \mathscr{p}_k = \mathfrak{I}(p_s) \tag{110}
$$

where $\mathfrak{I}$ represents the DFT operation and k enumerates the frequency in DFT space. The advantage of solving for influence functions in DFT space comes from the convolution

property of DFT. From the expression in Eq. (104), it can be seen that the right hand side of the equation is comprised of terms which are the convolution of local microstructure descriptors and influence functions. In other words, the influence functions are coupled with spatial and local state variables. In spatial frequency space, the expressions are decoupled due to the fact that DFT takes care of the convolution. This decoupling can be seen below for first order terms:

$$\Im(\boldsymbol{p}_s) = \Im\left(\sum_L \sum_t \boldsymbol{A}_t^L M_{s+t}^L\right) \tag{111}$$

$$\boldsymbol{p}_k = \sum_L \mathcal{A}_k^L \mathcal{M}_k^L \tag{112}$$

When we cast the first order terms in DFT space, DFT operation takes care of the summation over spatial variable. In DFT space, the local response field is defined with only one summation which is over local state variable, L. The spatial variable in Eq. (112) is the frequency index k. Since there is no summation over k, influence coefficients in DFT space, $\mathcal{A}_k^L$ can be solved separately for each unique frequency. The matrix format for OLS solution to Eq. (112) is given as below:

$$\mathcal{A} = (\mathcal{M}^\dagger \mathcal{M})^{-1} \mathcal{M} \boldsymbol{p} \tag{113}$$

where $\dagger$ represents the Hermitian transpose. It is clear from Eq. (112) that the $\mathcal{M}^\dagger \mathcal{M}$ is a $L \times L$ matrix (i.e. 2×2 for two-phase material system). The above solution is repeated for each unique frequency, k to come up with the entire field of influence functions in DFT space. The computational efficiency lies in the inversion of $L \times L$ matrix. If we take a volume with a spatial grid of $S = 21 \times 21 \times 21 = 9261$ voxels, we repeat this operation $S = 9261$

times. However, inverting a 2×2 matrix for $S = 9261$ times is orders of magnitude faster than inverting a 18522×18522 matrix once. DFT operation helps us gather influence coefficients for very large spatial domains and very large number of local states in a very computationally efficient manner which often times it is computationally impossible to do with the brute force way in real space.

However, the computational advantage in calibration procedure is not the main reason in employing DFT operations. The crux of DFT operation lies in the prediction of response field after we obtain the influence coefficients which essentially contains the physics-based knowledge. The convolution of influence functions and local microstructure descriptor in frequency space is a Hadamard product (entrywise product). Once the influence functions are obtained, the response field of any microstructure in the material system in interest can be predicted in a matter of seconds. This is a result of the complexity of DFT operation. For instance, FE simulations have S^3 complexity while DFT operation has a complexity of $S \log S$. This helps us obtain the prediction of a response field often times orders of magnitude faster than FE simulations. This is the central advantage of MKS. In the next sections, the computational advantage of the MKS framework will be demonstrated with two case studies.

CHAPTER 4

MKS FOR SINGLE PHASE POLYCRYSTALLINE MATERIALS

Almost all of the case studies explored thus far have been restricted to composite material systems with a limited set of discrete local material states (i.e., two-phase or three-phase microstructures). However, most materials of interest in emerging technologies exhibit local states that are much more complicated. For example, most advanced structural materials exhibit polycrystalline microstructures, where the spatial distribution of the crystal lattice orientations at the microscale plays an important role in controlling their effective properties. High throughput evaluation of the responses of a large set of microstructures (as one might need in optimizing the material performance in a selected application) with such complex local states requires a major extension of the MKS framework that allows efficient treatment of tensorial local states (e.g., crystal lattice orientation) and their associated continuous local state spaces. In this regard, it should be recognized that it is possible to treat continuous local states simply by binning the continuous local state space (as described in our earlier work [19]). However, a primitive binning of the local state space is expected to prove highly inefficient, computationally, in capturing accurately the localization linkages of interest, especially in situations where the microscale response in the material microstructure shows high sensitivity to the local state (e.g., plastic response of crystalline states).

This section presents the needed extension to the theoretical framework of the MKS approach to allow a rigorous treatment of the crystal lattice orientation as the local state

67

variable. This is accomplished through the use of Generalized Spherical Harmonics (GSH) [73] for capturing the orientation dependence of the influence kernels in the MKS linkages. It should be noted that GSH have already been demonstrated to produce highly efficient and compact spectral descriptions of functions defined on the orientation space in other applications in prior literature [11, 30-44]. The viability of the new MKS formulation developed in this work is demonstrated with case studies on selected cubic and hexagonal polycrystalline material systems.

4.1 Generalized Spherical Harmonics

Extension of MKS formulation to continuous local states requires suitable Fourier basis function, $Q_L(n)$ in the series (Eq. (104)). For single phase polycrystals, where the local state is adequately described by the crystal lattice orientation, the response field can be expressed using the crystal lattice orientation, g, as the local state variable with only the first order terms as follows:

$$\boldsymbol{p}_s = \sum_L \sum_t \frac{\Delta}{N_L} \boldsymbol{A}_t^L M_{s+t}^L = \sum_t \int_{FZ} \alpha_t(g) f_{s+t}(g) dg \qquad (114)$$

where $A_t(g)$ is the influence function which is a function of crystal lattice orientation. In Eq. (114), $f_s(g)$ is generally referred to as the spatially resolved orientation distribution function (ODF) for the spatial bin labeled s. Since $f_s(g)$ is the probability density, $f_s(g)dg$ denotes the volume fraction of material with crystal lattice orientation in the spatial bin s that can be associated with crystal lattice orientations that lie within dg around g. With this reinterpretation, it should be easy to see the correspondence between $f_s(g)dg$ and M_s^L.

Furthermore, the reformulation of the MKS formulation as shown in Eq. (114) is completely consistent with the expressions used in statistical continuum theories [28, 29, 74-76].

Note that the use of crystal lattice orientation in localization relationships demands integration over the fundamental zone of crystal lattice orientations (denoted as *FZ*). This computation can of course be performed numerically (generally corresponds to a suitable binning the *FZ*). However, based on past experience [31, 40, 44], the number of bins needed for sufficiently accurate numerical integration of the integral in Eq. (114) is expected to be substantially large. Note also that a large number of bins would also imply that an equally large number of influence functions will have to be calibrated in the MKS approach. As a result, a direct numerical integration of the integral in Eq. (114) is not very attractive from a computational perspective.

To represent ODF with a suitable Fourier basis function, one needs a definition of the crystal lattice orientation, g is represented. Crystal lattice orientation, g is represented with 3 angles (also known as Euler angles) and they are used to transform the reference (or sample) frame to crystal frame. The angles used in these case studies are called Bunge-Euler angles $(\varphi_1, \Phi, \varphi_2)$ and they are applied to sample frame in 3 successive rotations. This procedure is illustrated in Figure 14. The sample frame is represented by $\{e_1, e_2, e_3\}$. First, the sample frame is rotated with an angle of φ_1 about e_3. Then, the new coordinate system $\{e_1', e_2', e_3'\}$ is rotated with an angle of Φ about e_1'. The last rotation angle is φ_2 and the new coordinate system $\{e_1'', e_2'', e_3''\}$ is rotated with it about e_3''. The resulting directions $\{e_1^c, e_2^c, e_3^c\}$ denote the crystal frame.
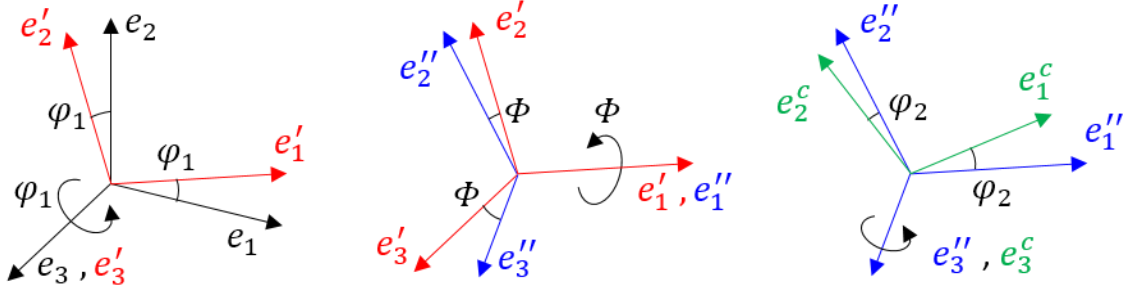
Figure 14: Illustration of the representation of crystal lattice orientation with Bunge-Euler angles, $(\varphi_1, \Phi, \varphi_2)$.

Based on prior work with a mathematical framework called Microstructure Sensitive Design (MSD) [31, 40], it can be hypothesized that the use of Generalized Spherical Harmonics (GSH) [73] as a Fourier basis for functions defined on the orientation space would lead to an efficient computation of the integral in Eq. (114). In particular, we note that in a prior case study [77], the elastic localization terms (very similar to those seen in the MKS series expansion discussed here) in classes of cubic-triclinic polycrystals were captured with only ten GSH coefficients. The ODF can be written in terms of GSH basis functions, $T_l^{mn}(g)$ as below:

$$f(g) = \sum_{l=0}^{\infty} \sum_{m=-l}^{+l} \sum_{n=-l}^{+l} C_l^{mn} T_l^{mn}(g) \tag{115}$$

where

$$T_l^{mn}(g) = T_l^{mn}(\varphi_1, \Phi, \varphi_2) = e^{im\varphi_1} P_l^{mn}(\Phi) e^{in\varphi_2} \tag{116}$$

P_l^{mn} are certain generalizations of associated Legendre function. The derivations of Eq. (115) and (116) are not included in this dissertation. However, the derivations can be found in [78]. GSH functions form a complete orthonormal basis [73]:

$$\oint T_l^{mn} T_l^{m'n'*} dg = \frac{1}{2l+1} \delta_{ll'} \delta_{mm'} \delta_{nn'} \tag{117}$$

where dg is the invariant measure of orientation space and * denotes the complex conjugate. The importance of orthonormality appears in implementing basis functions to MKS series expansion. The expression of ODF in Eq. (115) does not include any symmetries involving the crystal system. GSH functions can be modified to reflect any desired crystal and sample symmetries [40, 73]. For instance, symmetrized GSH functions for cubic-triclinic symmetry are denoted as $\ddot{T}_l^{\mu n}$, and can be found as a linear combination of GSH functions:

$$\ddot{T}_l^{\mu n} = \sum_{m=-l}^{l} \ddot{C}_l^{m\mu} T_l^{mn} \, \delta_{nn'} \tag{118}$$

where $\ddot{C}_l^{m\mu}$ are the coefficients that account for the cubic crystal symmetry and $\ddot{T}_l^{\mu n}$ are the symmetrized GSH functions. Similar approach can be repeated for sample symmetry as well. The double dot above the coefficients denote the crystal symmetry and a single dot denote the sample symmetry. If the coefficients accommodate both of the symmetries, then it is written with 3 dots. In Eq. (118), there are not solution for all possible l. These solutions can be found by singular value composition (SVD) or null space approaches. The number of linearly independent solutions to Eq. (118) are actually enumerated by index μ. It will be shown in this and next case study that for cubic-triclinic symmetry, there are only 2 linearly independent orthogonal solutions from up to $l = 4$. Since index n runs from $-l$ to $+l$, for each solution of l, there are $2l + 1$ functions. For instance, symmetrized GSH functions of cubic-triclinic symmetry has one solution for $l = 0$ and $l = 4$. This makes 10

functions in total for cubic triclinic symmetry up to $l = 4$. Similar comments can be made for the number of functions for hexagonal-triclinic symmetry which has one solution for each of $l = \{0,2,4\}$ leading to 15 functions. The number of solutions for different l values and crystal symmetries are given in [73].

4.2 Derivation of MKS for Single Phase Polycrystalline Aggregates

Symmetrized GSH functions, $\dot{T}_l^{\mu n}$ were selected for as Fourier basis function for the functions defined over the orientation space ($\alpha_t(g)$ and $f_s(g)$). It is anticipated that the influence functions can be represented compactly [31, 40, 44, 75, 77] with a small number of GSH terms. Such representations can be expressed as:

$$f_s(g) = \sum_{\mu,n,l} M_{ls}^{\mu n} \dot{T}_l^{\mu n}(g) \ , \ \ M_{ls}^{\mu n} = (2l+1) \int_{FZ} f_s(g) \dot{T}_l^{\mu n*}(g) dg \tag{119}$$

$$\boldsymbol{\alpha}_t(g) = \sum_{\mu,n,l} \boldsymbol{A}_{lt}^{\mu n} \dot{T}_l^{\mu n}(g) \ , \ \ \boldsymbol{A}_{lt}^{\mu n} = (2l+1) \int_{FZ} \boldsymbol{\alpha}_t(g) \dot{T}_l^{\mu n*}(g) dg \tag{120}$$

where $M_{ls}^{\mu n}$ and $A_{lt}^{\mu n}$ are the Fourier coefficients of the functions $f_s(g)$ and $\alpha_t(g)$, respectively. The number of coefficients in the Fourier representations for each s (or t value) are determined by the combinations of μ, n and l. For simplicity and consistency with the generalized MKS framework shown in Eq. (104), all combinations of these indices will be enumerated by a single index L. By using the Fourier representations above, the MKS series expansion for single polycrystalline aggregates can be derived. If we insert the Fourier representations in Eq. (119) and (120) into (114), we obtain:

$$\boldsymbol{p}_s = \sum_t \int_{FZ} \left[\sum_L \boldsymbol{A}_t^L \dot{T}^L(g) \right] \left[\sum_{L'} M_{s+t}^{L'} \dot{T}^{L'}(g) \right] dg \qquad (121)$$

We can take the summations outside the integral and if we rearrange the terms, we get:

$$\boldsymbol{p}_s = \sum_t \sum_L \sum_{L'} \boldsymbol{A}_t^L M_{s+t}^{L'} \int_{FZ} \dot{T}^L(g) \dot{T}^{L'}(g) dg \qquad (122)$$

Attention must be paid to the terms inside the integral in Eq. (122). These terms are almost identical to the orthonormality condition of GSH functions given in Eq. (117), except the conjugate. To get rid of the integral in Eq. (122), we have to have conjugate on one of the GSH functions inside the integral. We can go around this problem by simply conjugating Fourier representation of ODF (see Eq. (119)) inserted in Eq. (121). This conjugate does not change the result of ODF as ODF is a real valued function (probabilistic measure). With the conjugate, the expression in Eq. (122) becomes:

$$\boldsymbol{p}_s = \sum_t \sum_L \sum_{L'} \boldsymbol{A}_t^L M_{s+t}^{L'*} \int_{FZ} \dot{T}^L(g) \dot{T}^{L'*}(g) dg \qquad (123)$$

where * denotes the conjugate. Now that we have the conjugate term inside the integral, the definition in Eq. (117) can be plugged in Eq. (123).

$$\boldsymbol{p}_s = \sum_t \sum_L \sum_{L'} \boldsymbol{A}_t^L M_{s+t}^{L'*} \frac{\delta_{LL'}}{2l+1} \qquad (124)$$

where $\delta_{LL'}$ is the Kronecker delta. Due to $\delta_{LL'}$, the terms inside the summations only have non-zero values when $L = L'$. Hence, the expression in Eq. (124) can be reduced to:

$$\boldsymbol{p}_s = \sum_t \sum_L \frac{1}{2l+1} \boldsymbol{A}_t^L M_s^{L'*} \tag{125}$$

where $1/(2l+1)$ is the normalization factor resulting from GSH functions and actually corresponds to the normalization factor given in Eq. (104). This result is a testimony to the flexibility and versatility of generalized MKS framework shown in Eq. (104). Generalized MKS framework can be extended for a wide variety of material systems and phenomena given that a suitable Fourier representation function is selected for both the influence function and local microstructure representation.

4.3 Calibration of Influence Functions

Now that the localization relationships for single-phase polycrystalline aggregates are known, the influence functions can be calibrated. In this case study, we will limit our attention to the first term in the MKS series expansion (referred to as first-order influence functions), since our prior work [23, 25] on a range of material systems has demonstrated that this term is adequate in providing accurate MKS localization linkages for low to moderate contrast composite material systems. As mentioned earlier, our overall strategy is to calibrate the influence functions such that the predictions from MKS localization linkages match the corresponding results from micromechanical finite element simulations obtained on selected microstructures [18, 19, 23, 25, 40].

4.3.1 Selection of Microstructures for Training Dataset

The first step in the calibration process is the selection of the ensemble of microstructures for training the localization linkages. The specific volume elements used in the calibration and validation steps have been referred to as microscale volume elements

(MVEs). It was shown that MVEs reflecting "delta" microstructures were adequate to calibrate the first-order influence coefficients for low contrast composite material systems with a small number of distinct phases (i.e., local states) [25]. Delta microstructures are represented using MVEs where one central volume element is assigned one phase, and all other volume elements are assigned another phase (see the MVE at the left of Figure 15). The response of a delta microstructure corresponds to the output of an impulse signal, and makes it trivial to calibrate the influence coefficients [23, 25]. However, as noted earlier, the local state space in polycrystalline materials is comprised of a very large number of distinct crystal lattice orientations, and thereby requires a different strategy. In this case study, three different types of microstructures were used in the training set: (i) delta, (ii) equi-axed, and (iii) random microstructures (see Figure 15). As noted earlier, delta microstructures are very efficient in capturing accurately the fundamental interactions between the two local states represented in them. However, since we can explore only two orientations at a time with each MVE exhibiting a delta microstructure, they are not efficient in quickly exploring the interactions between all possible local states (note that a very large number of local states are possible in the case studies selected in this work). Conversely, the random microstructures (where each volume element is assigned a distinct crystal lattice orientation) permit efficient exploration of the interactions between a large number of crystal lattice orientations. Note also that the random microstructures produce the most heterogeneous stress (and strain) fields in the MVEs. The equi-axed microstructures were added to the calibration dataset as they reflect the type of microstructures encountered in real applications.

| (a) Delta | (b) Equi-axed | (c) Random |
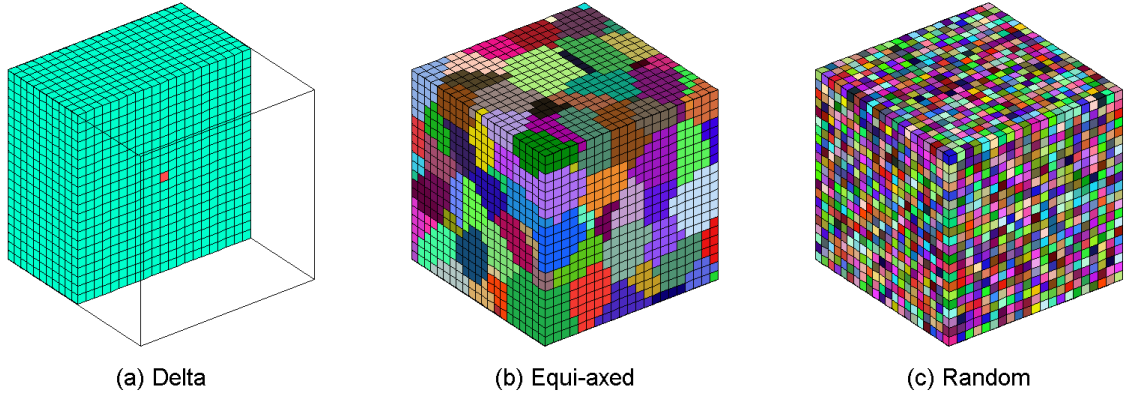
Figure 15: Examples of MVEs (of size $21 \times 21 \times 21$) used for the calibration of influence coefficients for polycrystalline material systems studied in this work: (a) delta microstructures, (b) equi-axed microstructures, and (c) random microstructures.

Taking into account inherent symmetry of the crystal lattice, the local state space for cubic and hexagonal polycrystals studied in this work can be expressed as [40]:

$$FZ_C = \left\{ \begin{array}{c} g = (\varphi_1, \Phi, \varphi_2) | 0 \leq \varphi_1 \leq 2\pi, \\ \cos^{-1}\left(\dfrac{\cos \varphi_2}{1 + \cos^2 \varphi_2}\right) \leq \Phi \leq \dfrac{\pi}{2}, 0 \leq \varphi_2 \leq \dfrac{\pi}{4} \end{array} \right\} \tag{126}$$

$$FZ_H = \left\{ g = (\varphi_1, \Phi, \varphi_2) | 0 \leq \varphi_1 \leq 2\pi, 0 \leq \Phi \leq \dfrac{\pi}{2}, 0 \leq \varphi_2 \leq \dfrac{\pi}{3} \right\} \tag{127}$$

The assignment of crystal orientations to each volume element in the MVE must be accomplished in such a way that it permits efficient exploration of the very large range of potential spatial interactions between all possible local states [79]. Since the local state space for the problems at hand is a continuous space (see Eq. (104)), the number of distinct orientations making up the local state space is essentially infinite. A strategy that has been successfully used in prior studies is to identify a set of *principal orientations* [40] that exhibit the extremes in the local responses (or properties) of interest. The central hypothesis is that using these principal orientations in the calibration process ensures that the localization linkages are employed largely as interpolations as opposed to extrapolations. It was

previously shown that the principal orientations can be identified as the vertices of a texture hull in the GSH space [42, 80], which were also observed to correspond with the orientations on the bounding surfaces of the fundamental zone [79]. In this work, our goal is to demonstrate that the framework described above works well for both cubic and hexagonal polycrystals. We will therefore undertake two separate case studies (one for cubic and one for hexagonal) and demonstrate that in both cases the influence functions need representation only up to $l \leq 4$, as claimed earlier. We therefore generated two calibration datasets, one for each crystal symmetry, while essentially following the same overall approach. In this work, the set of principal orientations were sampled from the bounding surface of the respective fundamental zones (see Figure 16). For the calibration microstructures with hexagonal crystals, the principal orientations were selected only from the surface of FZ_H corresponding to $\varphi_2 = 0$ (see part (b) of Figure 16), because the angle φ_2 has no influence on the local elastic stiffness of the crystal (because of the transverse isotropy implied in the description of the elastic stiffness for hexagonal crystals).
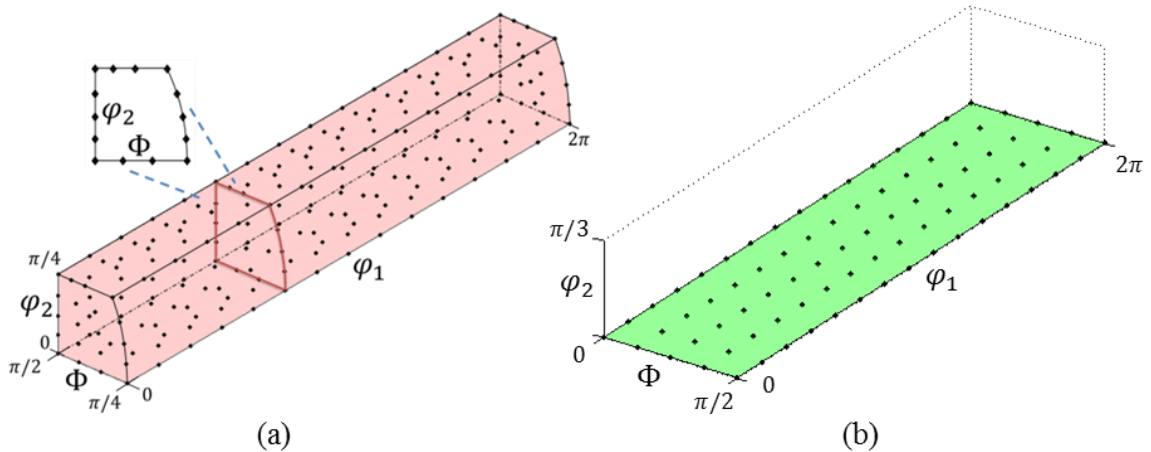
Figure 16: (a) 222 principal crystal lattice orientations used in the calibration of influence coefficients for cubic polycrystals, and (b) 80 principal crystal lattice orientations used in the calibration of the influence coefficients for hexagonal polycrystals.

To prove that the selection of orientations from the surfaces of FZ_C and FZ_H count as principal orientations, we can visualize the GSH coefficients. Since every spatial voxel in the MVE is occupied by one distinct crystal orientation, the ODF if each cell reduces to single crystal ODF. If we call the single crystal orientations in a spatial voxel s as g_0, the GSH coefficients of $f_s(g_0)$ are simply given by:

$$M_s^L = (2l + 1)\dot{T}^{L*}(g_o) \tag{128}$$

For cubic-triclinic symmetry of interest in the present case study, the spectral representation of the elastic stiffness tensor in the orientation space is expected to include all $l \leq 4$ GSH terms [20]. Taking into account the fact that GSH coefficients for real functions have certain interdependencies (some of the coefficients will be complex conjugates of the others), the GSH representations for $l \leq 4$ constitute 10 dimensions. In Table 2 is given GSH coefficients, M_s^L of a cubic-triclinic crystal system for Bunge-Euler angles of $(\varphi_1, \Phi, \varphi_2) = (156, 45, 7)$ in degrees. There is only one term for $l = 0$ and it is always 1. For $l = 4$, there are 9 terms. The coefficients that correspond to even numbers of n are conjugate of their negative counterpart (recall that n is one of the three indices that constitute the general index of L). As an example, the coefficients that correspond to $n = 4$ is the conjugate of the coefficient for $n = -4$. On the other hand, the coefficients that correspond to odd numbers are negative conjugate of their negative counterpart. For each solution there are $2l + 1$ coefficients for a selected l. Hence, the number of coefficients for each solution is an odd number. The center value corresponds to $n = 0$ and it is always real. This is a general characteristic of GSH coefficients for any crystal system, solution index and crystal lattice orientation.

Table 2: GSH coefficients, M_s^l of a cubic-triclinic crystal system for Bunge-Euler angles of $(\boldsymbol{\varphi_1}, \boldsymbol{\Phi}, \boldsymbol{\varphi_2}) = (\mathbf{156}, \mathbf{45}, \mathbf{7})$ in degrees. The first column shows the unified index for all combinations of $(\boldsymbol{\mu}, \boldsymbol{n}, \boldsymbol{l})$. The second column shows the solution number for series index $\boldsymbol{l}$ (fourth column). The third column shows the indices of coefficients for a specific series index $\boldsymbol{l}$. In the fifth column is shown the GSH coefficients, M_s^L

L	μ	n	l	M_s^L
1	1	0	0	1
2	1	-4	4	$0.726 - 2.913i$
3	1	-3	4	$0.686 - 1.057i$
4	1	-2	4	$-4.152 + 3.244i$
5	1	-1	4	$-0.619 + 0.213i$
6	1	0	4	-1.849
7	1	1	4	$0.619 + 0.213i$
8	1	2	4	$-4.152 - 3.244i$
9	1	3	4	$-0.686 - 1.057i$
10	1	4	4	$0.726 + 2.913i$

However, the visualization of cubic-triclinic texture hull in 10 dimensions in order to identify the principal orientations is a major challenge. To visualize the principal orientations in a reduced order space, we utilized principal component analysis (PCA). PCA essentially provides a linear transformation of high dimensional data into a new orthonormal coordinate frame, whose axes are ordered by the amount of the variance observed in the dataset (with the first axis identifying the direction of maximum variance in the dataset). The same idea was used in prior work in a different context [26, 81]. Figure 2 shows PCA representations of the single crystal orientation distributions corresponding to orientations sampled from FZ_C. The sample orientations are color-coded such that the orientations on the surface of FZ_C are marked red, while the orientations inside FZ_C are marked blue. It can be seen from the PCA plots (low dimensional projections) in Figure 17 that the orientations on the surface of FZ_C are indeed the principal orientations of interest.

Based on this observation, 220 principal orientations are selected from the bounding surface of FZ_C for the calibration steps.
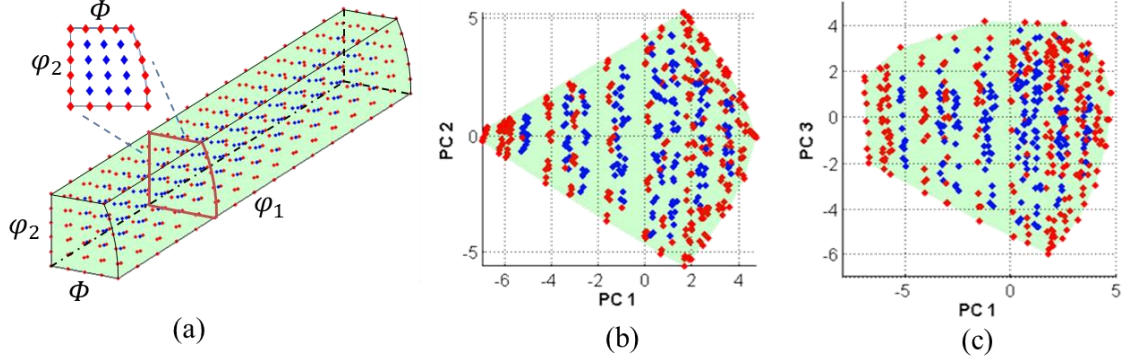
Figure 17: (a) Cubic-triclinic fundamental zone, $\boldsymbol{FZ_C}$. Red points show the orientations on the surface of $\boldsymbol{FZ_C}$ and blue points show the orientations inside the zone. (b) and (c) show the GSH representations for the single crystal orientation distribution functions corresponding to the crystal orientations in (a) in the PCA subspaces.

4.3.2 Micromechanical Finite Element Models

The calibration dataset for the present work was established by executing micromechanical finite element simulations using commercial software ABAQUS [82]. Each MVE was represented by a finite element mesh of uniform cuboids (eight-noded, three-dimensional, solid elements, C3D8 [82]) defined on a $21 \times 21 \times 21$ grid. On this uniformly gridded finite element mesh, different assignments were made for the crystal orientations (see Figure 16) to produce the three different classes of microstructures shown in Figure 15.

All of the MVEs studied here were subjected to a uniaxial strain using periodic boundary conditions. In other words, the loading conditions were such that only the $\langle \varepsilon_{11} \rangle$ (average normal strain component along the 1-axis) was allowed to be non-zero. Two material systems were selected for this study: (i) copper with elastic stiffness constants $C_{11} = 168.4 GPa$, $C_{12} = 121.4 GPa$ and $C_{44} = 75.4\ GPa$ [83] (this corresponds to cubic

anisotropy ratio of $A = 3.21$), (ii) α-Ti with elastic stiffness constants $C_{11} = 154 GPa, C_{12} = 86 GPa, C_{44} = 46\ GPa, C_{13} = 67\ GPa$ and $C_{33} = 183\ GPa$ [84]. Based on these values, we might characterize copper as a moderate contrast composite and α-Ti as a low contrast composite [43].

4.3.3 Calibration of Influence Functions

The calibration dataset was established by executing micromechanical finite element simulations on a total of 3600 microscale volume elements (MVE) using commercial software ABAQUS [82] for each case study presented in this case study. The MVEs were produced as explained in the previous subsection. While there is always the possibility of adding more MVEs to the calibration dataset, it was observed that addition of new MVEs to the calibration set did not contribute significantly to the accuracy and robustness of the localization linkages produced in this study.

As noted earlier, the calibration of the influence functions is best accomplished by casting the linkages in the DFT space [19, 22-25, 40]. Application of this strategy results in the following set of equations in the DFT space by using expressions in Eq. (110):

$$\boldsymbol{p}_k = \left[\left(\sum_L \mathcal{A}_k^{L*} \mathcal{M}_k^L \right) \right] \langle p \rangle \tag{129}$$

where $\mathcal{A}_k^L$ and $\mathcal{M}_k^L$ are the Fourier coefficients of influence functions and the microstructure function in the DFT space. The corresponding linear regression [85] for establishing the influence kernels can be expressed as

$$\sum_r {}_r\boldsymbol{\mathscr{P}}_k \left({}_r\mathcal{M}_k^{L'} \right)^* = \sum_L \boldsymbol{\mathscr{A}}_k^{L*} \left[\sum_r {}_r\mathcal{M}_k^L \left({}_r\mathcal{M}_k^{L'} \right)^* \right] \tag{130}$$

where k denotes the spatial frequency in the DFT space and r indexes the training MVEs used in the calibration process.

One of the important consequences of casting the MKS kernels in a spectral basis for representing the functional dependence on continuous local states is that the number of terms even in the first-order expansion is essentially infinite (see Eq. (125)). We expect only a finite number of these to be dominant. For example, based on our prior experience [31, 77, 79], we anticipate that only ten of the $\boldsymbol{A}_t^L$ terms in Eq. (125) (i.e., $l = (0, 4)$, which is then mapped to $L = 1, \dots, 10$) would have dominant contributions for cubic polycrystals. The number of dominant terms in A_t^L for hexagonal polycrystals is expected to be only fifteen (corresponding to $l = (0, 2, 4)$, which is then mapped to $L = 1, \dots, 15$) [44]. In order to critically evaluate this hypothesis, we systematically computed the average error in the localization linkages as a function of the truncation level (i.e., for different values of the maximum value of L) [18] for a selected ensemble set of microstructures. For each trial truncation level, the error between the MKS and FEM predictions for each MVE in the calibration set is defined as the mean absolute strain error (MASE) E_r [18]:

$$E_r = \sum_{s=1}^{S} \frac{|p_s^{FEM} - p_s^{MKS}|}{S \times \langle p \rangle} \times 100 \tag{131}$$

where p_s^{FEM} and p_s^{MKS} are the values of the response field of interest (here the ε_{11} strain component) in the spatial bin s of FEM and MKS predictions, respectively, and $\langle p \rangle$ is the macroscale average value of the response field. In Figure 18, the effect of increasing the

number of coefficients for the spectral representation of the influence functions on the error in the calibrated localization linkages is shown. The plots show both the average value of MASE as well as the minimum and maximum values of MASE for the entire training set used in the analyses. As hypothesized, it is clearly seen that the terms corresponding to $l > 4$ (i.e., $L > 10$ for cubic and $L > 15$ for hexagonal) do not make any significant contributions to improving the accuracy of the MKS linkages for the elastic deformations in cubic and hexagonal polycrystals. More importantly, it is seen that the average MASE as well as the maximum and minimum MASE for the calibration set are extremely small for the entire datasets in both cubic and hexagonal polycrystals. As expected, the MASE is slightly higher for the moderate contrast Cu polycrystals compared to the low contrast Ti polycrystals. These observations validate the central hypothesis of this approach that the GSH representations of the influence functions over the orientation space are extremely efficient and compact. It is emphasized again that the tremendous dimensionality reduction obtained as a consequence of using the GSH representations results in major computational advantages.
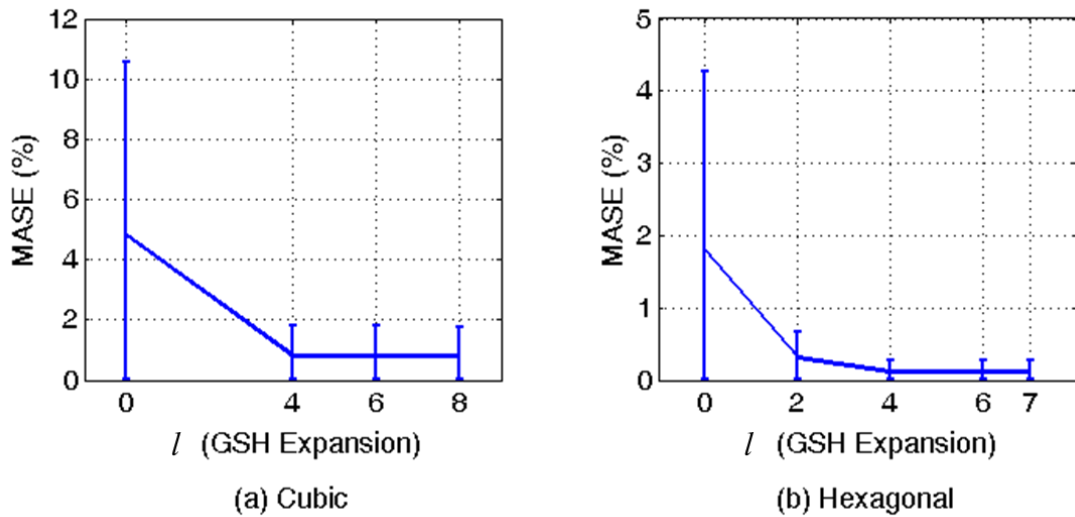
(a) Cubic (b) Hexagonal

Figure 18: Mean absolute strain errors for training sets as a function of the truncation level in the spectral representations of the influence functions: (a) Cubic polycrystals, (b) Hexagonal polycrystals.

The computational advantage of casting the MKS series expansion into the DFT space for calibration can be realized again by examining Eq. (130). Without transforming the localization series into spatial frequency space, the total number of Fourier coefficients of influence functions that needs to be calibrated simultaneously are 92,610 ($= 10 \times 21 \times 21 \times 21$) for cubic polycrystals and 138,915 ($= 15 \times 21 \times 21 \times 21$) for hexagonal polycrystals. However, in the DFT space, the number of coupled variables is only 10 for cubic and 15 for the hexagonal case (established separately for each spatial frequency, k). In other words, in the DFT space, the complete set of 92,610 coefficients for cubic case are established by selecting only 10 at a time, which leads to a remarkable savings in the computational effort involved in the calibration of influence functions.

In our prior work [18, 19, 25], it was shown that the influence coefficients decayed to zero values with increasing distance, t. In the reformulated localization series presented in this case study, the Fourier coefficients of influence functions, A_t^L, are also expected to show the same trend. A few selected Fourier coefficients of the influence functions are shown in Figure 19. It was seen that all of the Fourier coefficients established in this case study decayed to zero or near zero values, attesting to the robustness of calibration procedures used in this work. The decay of the influence coefficients to zero values at large values of t is essential for trivially extending the influence coefficients for larger MVEs by zero-padding. Furthermore, the fast decay of the influence coefficients confirms that the selected size of the MVEs used in the calibration ($21 \times 21 \times 21$) was adequate for the present case studies.
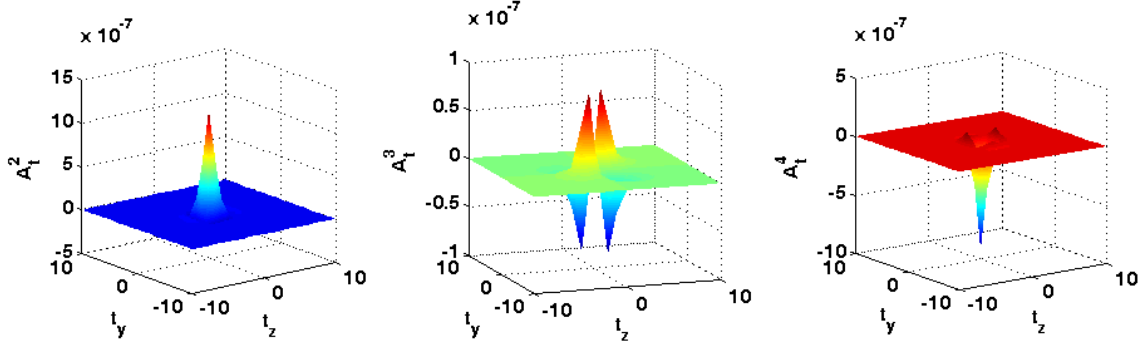
Figure 19: Variation of selected influence functions A_t^L as a function of y and z components of t (the x component of t is set to zero).

4.4 Validation of Localization Linkages

For the critical evaluation of the localization linkages established in this case study, two validation sets of 1800 microstructures comprising 600 delta, 600 equi-axed and 600 random microstructures were generated for each crystal symmetry. The crystal lattice orientations in the validation MVEs were selected randomly from the complete fundamental zones described in Eq. (126) and (127) (recall that only the orientations on the bounding surfaces of the fundamental zone were used in generating the calibration datasets).

The accuracy of the localization linkages established in this work is shown in Figure 1 by plotting the mean, minimum, and maximum errors (defined in Eq. (131)) for the two classes of polycrystals. As expected, the MASE increases with increased contrast (the anisotropy in Copper polycrystals is substantially larger than in α-Titanium). It is also seen that the influence kernels established in this study exhibit remarkable accuracy for both case studies presented (the maximum error of the entire set was less than 0.5% for hexagonal polycrystals, while it was less than 2% for cubic polycrystals). Note also that

the error levels in the validation and calibration datasets were of similar magnitude, further

validating the approach employed in this work.
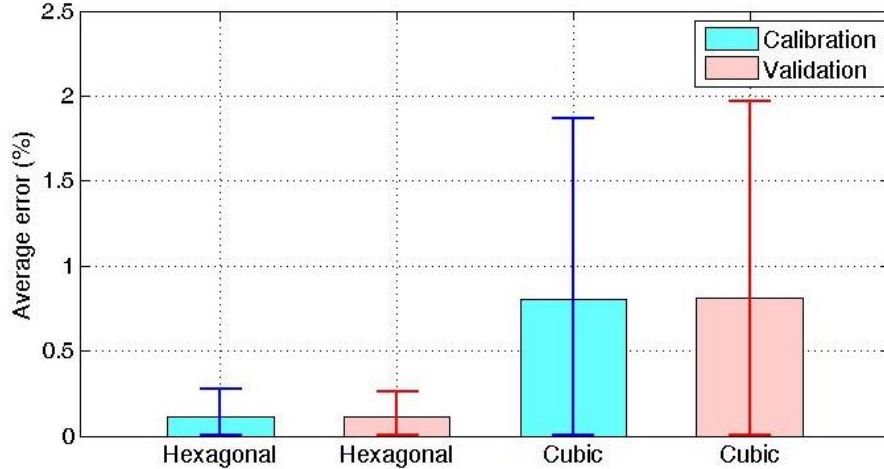
Figure 20: Summary of mean, minimum, and maximum of the absolute errors in the MKS linkages established in this work for elastic responses in cubic and hexagonal polycrystals.

Next, we critically evaluate the accuracy of localization linkages at the level of

individual spatial voxels in the MVEs. In Figure 21, the strain field predicted by the MKS

approach is compared with the corresponding prediction from FEM for a selected equiaxed

microstructure of Copper. The plots shown in Fig. 6(c) and 6(d) correspond to the strain

distributions of a middle slice of the three dimensional RVE shown in Fig. 6(a). Fig. 6(b)

compares the distributions of the strains present in the two predictions (for the entire MVE).

It is seen that there is an excellent agreement between the FEM and MKS predictions. The

value of the MASE for this MVE was only 1.6%. Similar comparisons for α-Ti

microstructures revealed even better agreement (because of the lower contrast) compared to

the results for the Cu polycrystals.
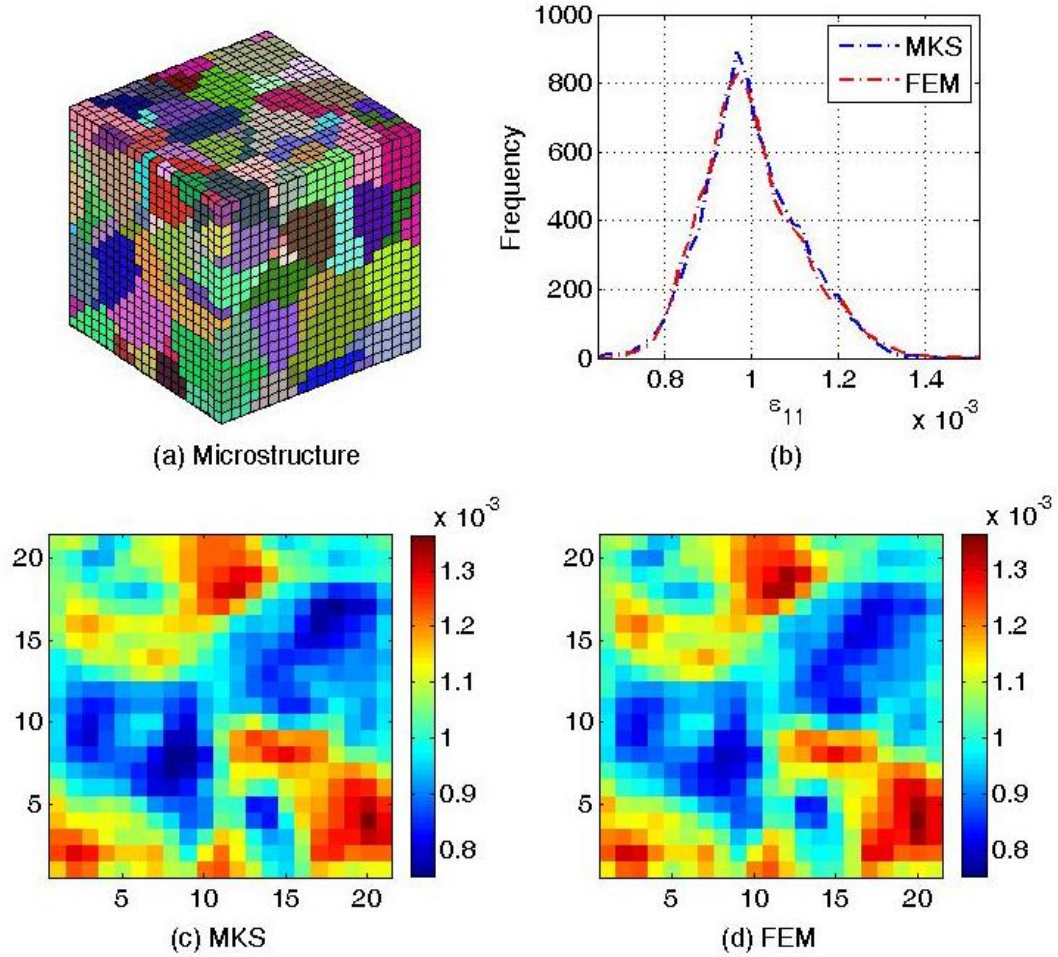
Figure 21: Comparison of strain fields predicted with MKS and FEM approaches. (a) An example Copper polycrystal microstructure selected for the validation. (b) Frequency plots of the predictions of ε_{11} from MKS and FEM. (c) and (d) Middle slices of strain fields predicted by MKS and FEM, respectively.

It is also important to note the computational efficiency of the MKS approach presented in this paper. For example, the FEM prediction of a $21 \times 21 \times 21$ microstructure took 25 seconds with 2 processors (each 3.0 GHz) on a supercomputer, while prediction with MKS took only 2 seconds with only 1 processor (3.0 GHz) on a standard desktop computer.

Scalability is one of the major advantages of localization linkages. As discussed earlier, influence functions are analogous to the Green's function and decay as the distance

t from the spatial cell of interest increases. In prior work, it was demonstrated that the influence functions obtained from smaller size MVEs can be trivially extended to larger domains by padding with zeros [18, 19, 25] to permit their usage on arbitrary-sized MVEs (or RVEs). In order to demonstrate this characteristic for the new localization linkages established in this work, the Fourier coefficients of the influence functions obtained from the $21 \times 21 \times 21$ domain are padded with zeros to acquire the functions for the larger domain of $51 \times 51 \times 51$. An example $51 \times 51 \times 51$ equiaxed microstructure was generated (see the top left plot of Figure 22) and 1255 distinct orientations from the complete cubic-triclinic FZ were assigned to the individual grains in the microstructure. The FEM and MKS predictions for this example microstructure are compared in Figure 22. The excellent agreement between the MKS and FEM predictions validates the scalability of the approach presented here. In terms of computational efficiency, the gain is indeed much more significant for the larger MVEs compared to the smaller MVEs. The FEM simulation of $51 \times 51 \times 51$ MVE took 6 minutes with 8 processors (each 3.0 GHz) on a supercomputer, while the MKS prediction took only 30 seconds with only 1 processor (3.0 GHz) on a standard computer.

Two aspects of the new approach presented in this case study must be paid attention. It is very clear that higher levels of anisotropy demand the consideration of higher-order terms in the localization linkages. In other words, one should not ignore the importance of the second term in Eq. (104) when one applies the approach described here to material systems that exhibit higher levels of anisotropy (which translates to higher levels of contrast). Second, it is also important to recognize that there is a critical need for a more rigorous evaluation of the accuracy of the localization linkages. The error measures used here as well

as the types of microstructures used here are somewhat limited. It would be beneficial to establish the localization linkages on a much larger set of microstructures with much more diversity in their topological features (only three families were used in this study).
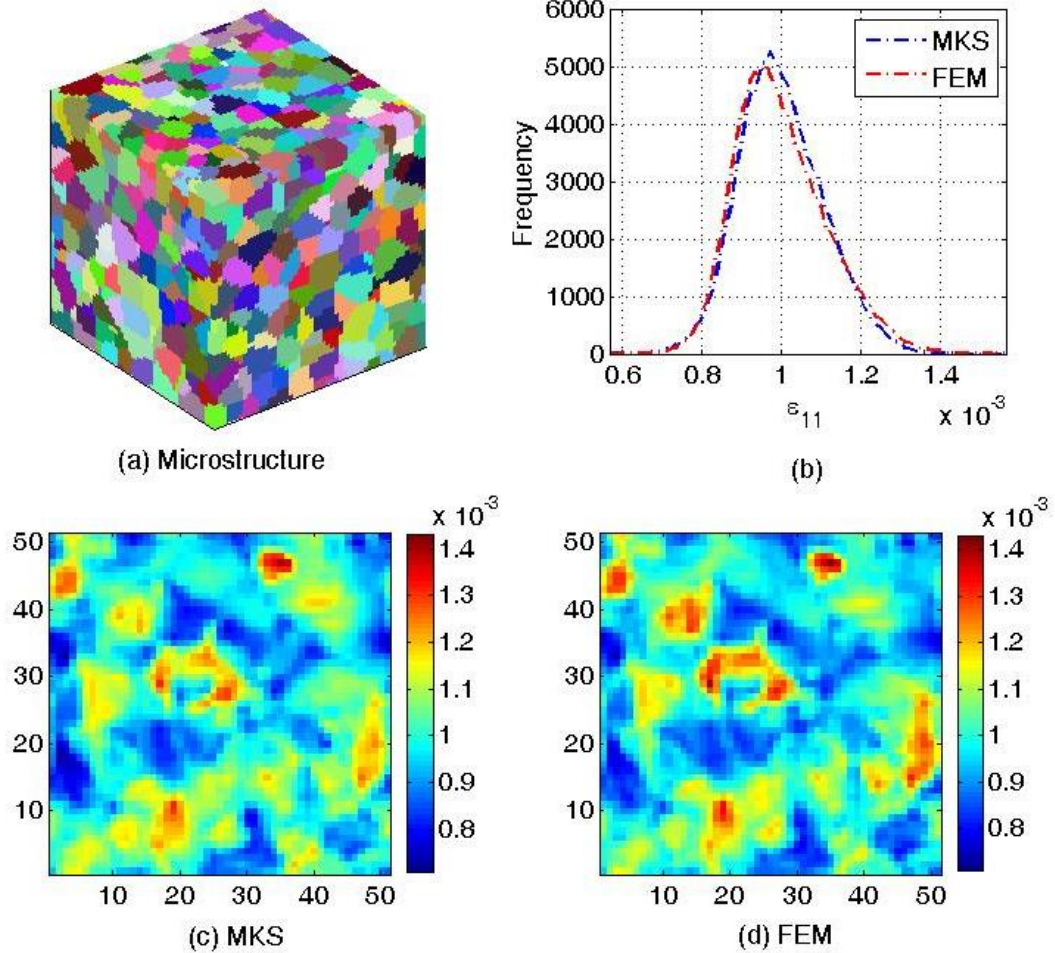
Figure 22: Comparison of strain fields predicted with MKS and FEM approaches. (a) The example $51 \times 51 \times 51$ copper polycrystal microstructure selected for validation. (b) Frequency plots of the predictions of ε_{11} from MKS and FEM. (c) and (d) Middle slices of strain fields predicted by MKS and FEM, respectively.

CHAPTER 5

MKS FOR A BROAD CLASS OF SINGLE PHASE

POLYCRYSTALLINE MATERIALS

In all prior applications of the MKS approach, one material system was considered at a time. In other words, the developed localization linkages databases were applicable only to a broad range of microstructures within a selected material system. In this case study, the viability of the generalized MKS framework is demonstrated to establish databases to elastic deformations in an entire family of cubic polycrystals. In this case study, we focus on the application of the generalized MKS framework introduced in the previous section to a family of cubic polycrystals. For this class of microstructures, the local state description needs to include both the crystal lattice orientation and the single crystal cubic elastic stiffness constants (expressed in the crystal reference frame). The crystal lattice orientation was expressed by a set of ordered Bunge-Euler angles, $g = (\varphi_1, \Phi, \varphi_2)$ in the previous chapter. In prior work [20, 86], it was shown that functions defined on the orientation space can be efficiently represented using symmetrized GSH functions, $\dot{T}_l^{\mu\nu}$, as a Fourier basis. More specifically, it was demonstrated that the elastic localization kernels for single phase cubic material needed only 10 terms in these GSH representations.

In this paper, we seek to establish localization linkages for an entire family of single phase cubic polycrystals (as opposed to doing this for each material system at a time). In order to accomplish this task, it is necessary to include the fundamental cubic single crystal

elastic stiffness constants, (C_{11}, C_{12}, C_{44}), in the local state description. In other words, the complete local state description for this problem can be expressed as $n = (g, C_{11}, C_{12}, C_{44})$. Note that this local state description now has six independent variables (recall that $g = (\varphi_1, \Phi, \varphi_2)$). This compounded local state description is needed to accurately represent the fourth-rank elasticity tensors in the sample reference frame in each spatial bin of the microstructure of interest (which now can correspond to a broad range of cubic polycrystals).

The next task is the selection of the Fourier basis, $Q_L(n)$ (see Eq. (94)). While we already know that $\dot{T}_l^{\mu\nu}$ can serve as a basis for the functional dependence on crystal lattice orientation, it is not clear what basis should be used for the other variables (C_{11}, C_{12}, C_{44}). The main challenge here arises from the fact that these variables are not defined on a periodic domain (unlike g). We selected Legendre polynomials $P(x)$ as a Fourier basis for inclusion of elastic stiffness constants in the local state description. In order to employ these basis functions, we need to rescale the variables such that their domain is mapped to the interval $(-1,1)$. This can be accomplished generically for any variable C by defining a new variable

$$C^r = \frac{2C - C_{min} - C_{max}}{C_{max} - C_{min}} \tag{132}$$

where C_{min} and C_{max} are the respective minimum and maximum values of C. Applying Eq. (132) to (C_{11}, C_{12}, C_{44}) results in rescaled descriptors $(C_{11}^r, C_{12}^r, C_{44}^r)$. We might now describe the extended local state for the material class of interest as $n = (g, C_{11}^r, C_{12}^r, C_{44}^r)$ with the Fourier basis selected as:

$$Q_L(n) = Q_L(g, C_{11}^r, C_{12}^r, C_{44}^r) = \dot{T}_l^{\mu\nu}(g)P_a(C_{11}^r)P_b(C_{12}^r)P_c(C_{44}^r) \tag{133}$$

The new localization relationships in continuous local state space can be written with only first order terms as:

$$\boldsymbol{p}_s = \sum_t \int_{CZ} \int_{FZ} \boldsymbol{\alpha}_t(g, C_{11}^r, C_{12}^r, C_{44}^r) f_{s+t}(g, C_{11}^r, C_{12}^r, C_{44}^r) dg dC_{11}^r dC_{12}^r dC_{44}^r \tag{134}$$

For simplicity, all combinations of the indices related to GSH functions (μ, n and l) can be enumerated by a single index I. The terms inside the integral can be written in terms of the Fourier basis functions shown in Eq. (133) as:

$$f_s(g, C_{11}^r, C_{12}^r, C_{44}^r) = \sum_{I,a,b,c} M_s^{Iabc} \dot{T}^I(g) P_a(C_{11}^r) P_b(C_{12}^r) P_c(C_{44}^r) \tag{135}$$

$$\boldsymbol{\alpha}_t(g, C_{11}^r, C_{12}^r, C_{44}^r) = \sum_{I,a,b,c} \boldsymbol{A}_t^{Iabc} \dot{T}^I(g) P_a(C_{11}^r) P_b(C_{12}^r) P_c(C_{44}^r) \tag{136}$$

If we insert these representations in Eq. (134) by ignoring the function variables to make the equation more compact:

$$\boldsymbol{p}_s = \sum_t \int_{CZ} \int_{FZ} \left[\sum_{I,a,b,c} \boldsymbol{A}_t^{Iabc} \dot{T}^I P_a P_b P_c \right] \tag{137}$$

$$\left[\sum_{I',a',b',c'} M_{s+t}^{I'a'b'c'} \dot{T}^{I'} P_{a'} P_{b'} P_{c'} \right] dg dC_{11} dC_{12} dC_{44}$$

Where CZ stands for the space covering the ranges of elastic stiffness constants. We can take the summations outside the integral and rearrange the terms as:

$$\boldsymbol{p}_s = \sum_t \sum_{I,a,b,c} \boldsymbol{A}_t^{Iabc} \sum_{I',a',b',c'} M_{s+t}^{I'a'b'c'}$$

(138)

$$\int_{CZ} P_a P_b P_c P_{a'} P_{b'} P_{c'} \int_{FZ} \dot{T}^I \dot{T}^{I'} dg dC_{11} dC_{12} dC_{44}$$

There are 2 orthonormality expressions in Eq. (138). First one is the orthonormality of Legendre polynomials and the second one is the orthonormality of GSH functions. However, the orthonormality of GSH functions is missing a conjugate like in the previous case study. We can go around this problem by taking the conjugate of ODF which is a real valued function. With the conjugate and orthonormality conditions, Eq. (138) can be rewritten as:

$$\boldsymbol{p}_s = \sum_t \sum_{I,a,b,c} \sum_{I',a',b',c'} \boldsymbol{A}_t^{Iabc} M_{s+t}^{I'a'b'c'*} \frac{8\delta_{aa'}\delta_{bb'}\delta_{cc'}}{(2a+1)(2b+1)(2c+1)} \frac{\delta_{II'}}{(2l+1)}$$

(139)

where δ is Kronecker delta. Just like in the previous case study, the variables of both summations are tied to each other with Kronecker delta. Hence the expression is only non-zero when the indices from the summations are the same. Based on this constraint and wrapping the combination of indices I, a, b and c to a single index L, we can remove the summation and reach the final form of MKS series expansion for a broad class of single phase polycrystalline aggregates.

$$\boldsymbol{p}_s = \frac{8}{(2a+1)(2b+1)(2c+1)(2l+1)} \sum_t \sum_L \boldsymbol{A}_t^L M_{s+t}^{L*}$$

(140)

where $8/(2a + 1)(2b + 1)(2c + 1)(2l + 1)$ accounts for the normalization factor of N_L in (93). Once again, the expression derived from continuous localization relationships (see Eq. (93)) yielded to the generalized MKS framework shown in Eq. (104).

5.1 Calibration of Influence Functions

The generation of calibration data set starts with the identification of the local state space corresponding to the selected local state descriptors. Since $n = (g, C_{11}^r, C_{12}^r, C_{44}^r)$ the overall local state space is essentially the compounded local state spaces of all the variables involved. The local state space for the crystal lattice orientation is simply the cubic-triclinic fundamental zone, FZ_C, defined in Eq. (126). This essentially means that each spatial bin of the microstructure can be assigned any combination of crystal lattice orientations from FZ_C. Although the framework presented above allows assignment of polycrystals at each spatial bin, we will restrict our attention here to the assignment of only single crystals in each spatial bin. In other words, we will assume that the spatial discretization used is such that only one crystal orientation is assigned in each spatial bin. The same strategy followed in the previous case study was followed here as well for the selection of orientations for calibration MVEs. 220 orientations are sampled from the surface of FZ_C.

Next we decide on the ranges for the elastic stiffness constants (C_{11}, C_{12}, C_{44}). The ranges were selected to include many of the commonly used cubic metals, while covering cubic anisotropy ratios (defined as $Z = 2C_{44}/(C_{11} - C_{12})$ [40]) in the range $Z = [0.5, 1.95]$. This range is expected to cover the range of low to moderate contrast for which the first term in the localization series is deemed adequate based on prior work [19, 20, 23-25]. It is also pointed out that $Z = 1$ corresponds to the isotropic case. Because of the rescaling described

earlier (see Eq. (132)), the range for the rescaled local state variables will be $(-1,1)$ independent of the selection of the ranges for (C_{11}, C_{12}, C_{44}). Within the selected range, a total of 64 distinct sets of (C_{11}, C_{12}, C_{44}) were used in generating the calibration dataset in this work. These sets are identified in Figure 23.
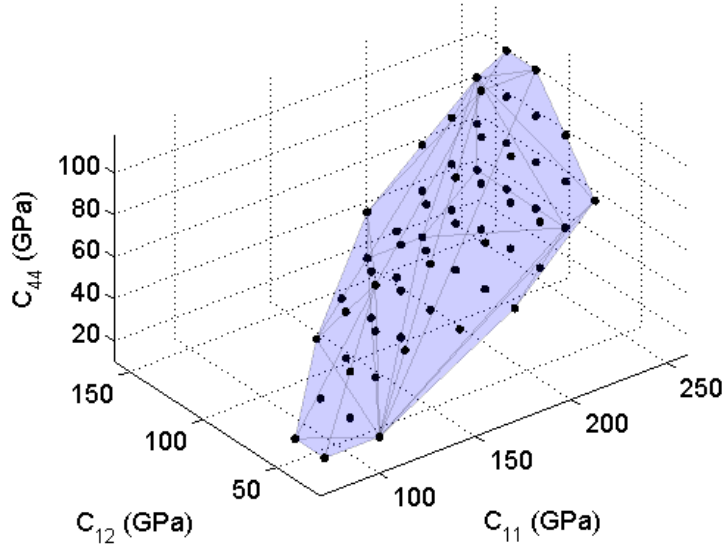
Figure 23: The set of 64 different combinations of the elastic stiffness constants $(\boldsymbol{C_{11}, C_{12}, C_{44}})$ used in the calibration step of the present study.

Once the local state and local state space are identified, next steps in generating the calibration data set are the selection of the classes of representative microstructures of interest. For calibration, same type of calibration MVEs are used and these are shown in Figure 15. It is also reminded again that each MVE is assigned only one set of elastic stiffness constants (i.e. single phase polycrystalline aggregates).

The final step in generating the calibration data set is to execute the micromechanical finite element (FE) simulations using suitable boundary conditions. Periodic boundary conditions were imposed on all MVEs used in the calibration in such a way that all macroscopic strain components other than ε_{11} had zero values. Repeating the simulations

with six different sets of boundary conditions allows us to establish the localization linkages for all components of the fourth rank elastic localization kernels [22, 25, 79]. Just like in the previous case study, we limit our attention to only the ε_{11} strain component. A uniformly discretized grid of $21 \times 21 \times 21$ is used for each MVE. Each spatial bin in the MVE is defined as an 8-noded, three-dimensional, solid element (C3D8) in the finite element mesh. A total of 1800 microstructures (600 of each of the three types of microstructures shown in Figure 15) compounded with 64 different assignments of single crystal elastic constants (shown in Figure 23) produced the calibration dataset used in this work. The finite element simulations were carried out using the commercial software ABAQUS [82].

The next major task in the establishing localization linkages for this case is the estimation of influence coefficients. As mentioned earlier, influence coefficients are calibrated to micromechanical finite element simulations through the application of linear regression methods in the DFT space. The first step in the calibration of influence coefficients is the spectral representation of each of the MVE included in the calibration set. Let $(g_s, C_{11s}^r, C_{12s}^r, C_{44s}^r)$ denote the local state in the spatial bin s. The spectral representation of the microstructure function for single crystal orientation distribution function and a selected set of elastic stiffness constants can then be written as

$$M_s^L = \frac{N_L}{\Delta} \dot{T}_l^{\mu n *}(g_s) P_a(C_{11s}^r) P_b(C_{12s}^r) P_c(C_{44s}^r) \tag{141}$$

Then, the calibration procedure shown in Eq. (130) is followed. However, we need to establish how many terms of the Fourier series we wish to retain (i.e., establish $\mathcal{L}$). In our previous work [20], we found out that we will only need ten of the GSH basis functions (corresponding to $l = (0, 4)$) for accurately representing the influence functions for cubic

96

polycrystals. Since we do not have any prior expectations on how many Legendre basis functions are needed to capture the functional dependence on the elastic stiffness parameters, we have to execute a few trials to establish this number. Using the calibration dataset prepared for this case study, OLS was performed using Eq. (130) for different truncation levels on the Legendre basis, and the average error in each MVE of the calibration set was computed based on the error measure give in Eq. (131). In this case study, it was decided to keep the truncation level the same for all three Legendre representations (one for each elastic stiffness parameter). Let $\mathcal{B}$ denote the number of terms retained in the Legendre series (same for all three elastic stiffness parameters). The value of $\mathcal{B}$ was increased systematically and the computed error using Eq. (131) is plotted in Figure 24. It was observed that truncation beyond $\mathcal{B} = 3$ did not improve the accuracy of the linkage significantly. It is also worth noting that the average error values for $\mathcal{B} = 3$ were extremely low ($<< 1\%$). This result implies that the elastic MKS influence functions can be captured with adequate precision for the family of cubic polycrystals studied here with only $\mathcal{L} = 270$ (i.e., 10 GSH terms and 3 terms for each Legendre basis) spectral coefficients. This is a remarkable compaction of an extremely complex physical phenomenon over a broad class of material systems.
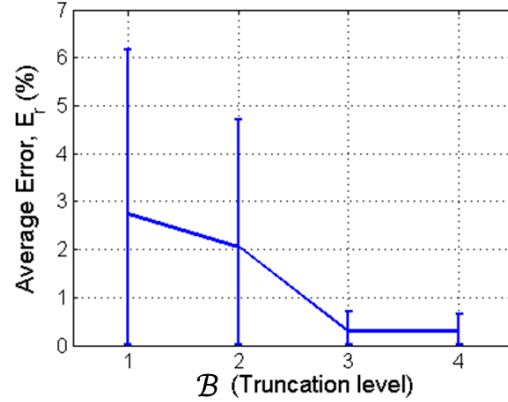
Figure 24: Error in the MKS linkages as a function of the truncation level of Legendre series for the representations over the elastic stiffness space

5.2 Validation of Localization Linkages

In order to evaluate the performance of the localization linkages, a validation data (distinct from the calibration dataset) was generated. For sampling of the local state space, MVEs of the validation set were assigned cubic single crystal elastic stiffness constants from the region shown in Figure 23 that are distinct from the 64 combinations used in the calibration set. For crystal lattice orientations, the entire cubic-triclinic fundamental zone is utilized in generation of the validation set as opposed to the selection of orientations only from the boundary of fundamental zone used in the calibration. As a result of these protocols, the microstructures used in the validation are completely distinct from those used in the calibration. A validation set of 9000 microstructures comprising 3000 delta, 3000 equiaxed, and 3000 random microstructures with assignments of single crystal elastic stiffness constants as described above, were utilized. The ε_{11} strain field for the validation dataset was predicted by executing FE simulations by applying the same boundary conditions used for calibration data set.

The last step of the MKS framework is the validation of the influence functions. This can be achieved simply by comparing directly the predictions from the localization linkages established with the validation dataset. The accuracy and the robustness of the localization linkages established in this case study is shown in Figure 25 by plotting the mean, minimum, and maximum errors for different cubic anisotropy ratios used in both the calibration and validation datasets. As expected, the average error increases with higher levels of anisotropy (results in higher contrast levels in the composite material system). It is also shown that the influence functions established in this study are highly accurate (note that highest average error is well below 1%).
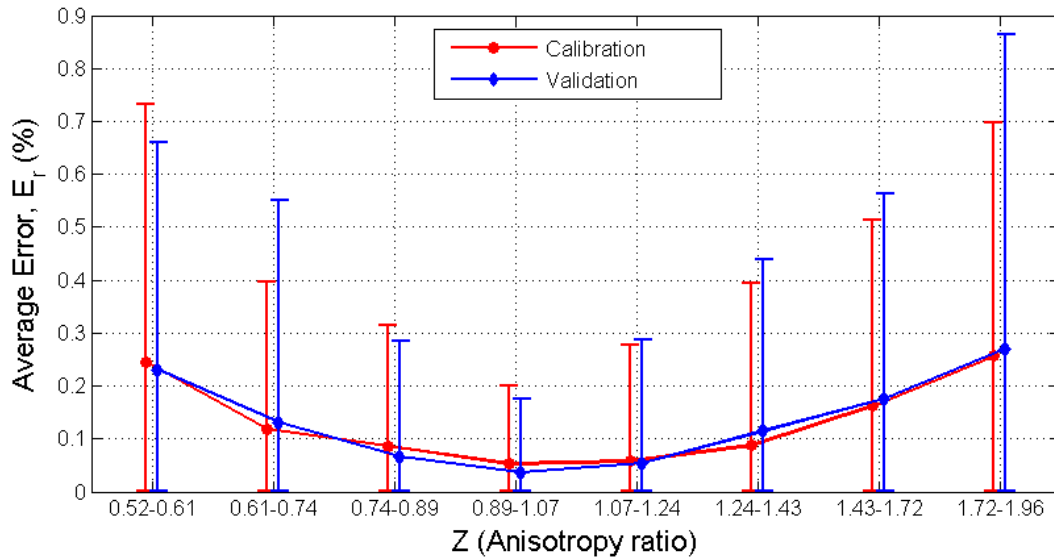
Figure 25: Variation of mean, minimum, and maximum of the absolute strain errors for the MVEs included in both the calibration and the validation datasets as a function of the degree of anisotropy

Figure 25 attests to the high accuracy of the localization linkages established in the present case study based on the average error definition from Eq. (131). Next, we critically evaluate the predictions of the localization linkages at the level of individual spatial bins. In Figure 26, the strain field predicted by the MKS approach for a selected equiaxed

microstructure with an elastic anisotropy ratio of $Z = 1.32$ is compared with the corresponding prediction from the FE simulation. Equiaxed microstructure shown in Figure 26(a) contained 157 distinct orientations randomly picked from the complete cubic-triclinic FZ. The middle slices of strain fields from MKS and FEM predictions are shown in parts (c) and (d) of Figure 26, respectively. Figure 26 shows the frequency plot of the strain distribution of entire MVE for both MKS and FEM predictions. From Figure 26, it can be seen that MKS and FEM predictions are almost indistinguishable from each other. It is noted that the average error for this example microstructure shown was only 0.11%.

(a) Microstructure

(b)

(c) MKS
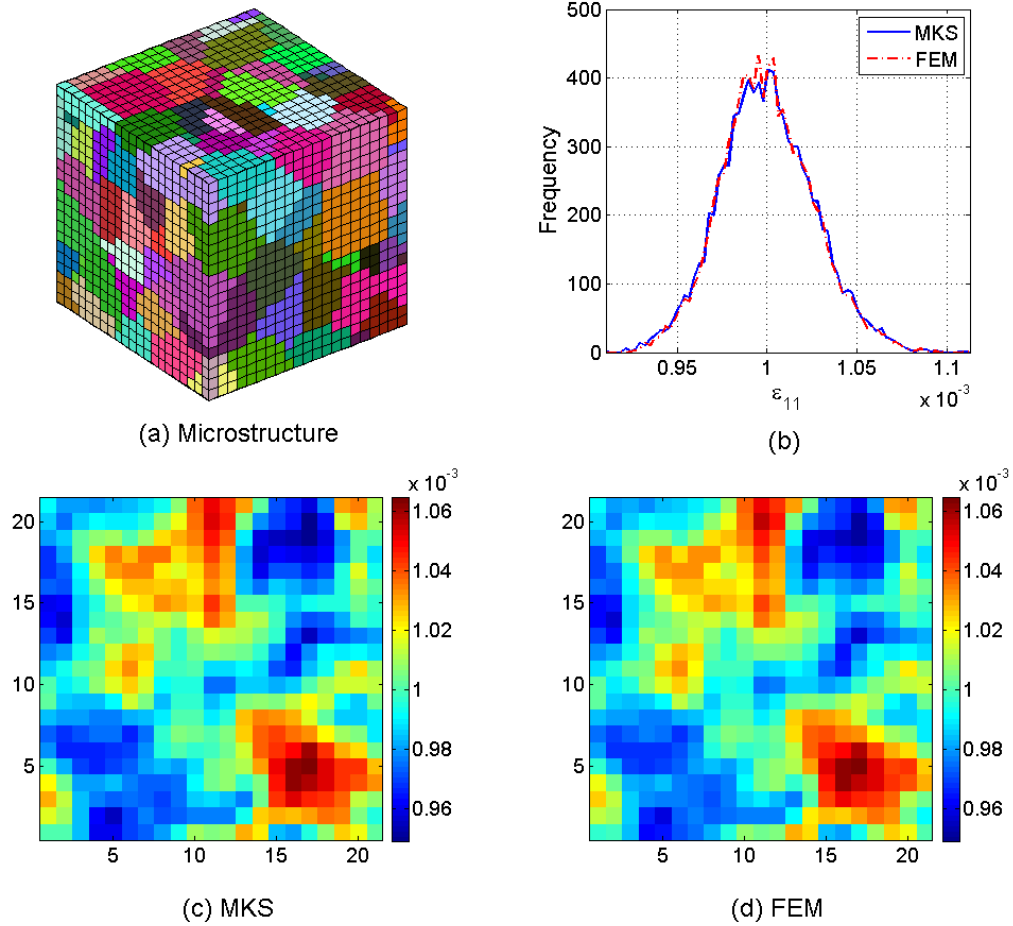
(d) FEM

Figure 26: Comparison of strain fields predicted with MKS and FEM approaches for a low elastic anisotropy cubic polycrystalline microstructure ($Z = 1.32$). a) $\mathbf{21 \times 21 \times 21}$ microstructure with each color representing a distinct orientation selected randomly from the complete cubic-triclinic fundamental zone. b) Comparison of MKS and FEM predictions as a frequency plot of $\boldsymbol{\varepsilon_{11}}$. Red dashed line shows the distribution of strains from FEM predictions, while the blue solid line shows the distribution of strains from MKS predictions. c) and d) show middle slices of strain fields predicted by MKS and FEM approaches, respectively

For cubic polycrystals with higher levels of anisotropy corresponding to $Z = 0.54$ and $Z = 1.94$, the MKS predictions are compared with the corresponding FEM results in Figure 27. Even though the values of the average error have increased somewhat (0.62% for the case with $Z = 1.94$, and 0.59% for the case with $Z = 0.54$), the accuracy of the localization linkages established in this work is remarkable. This is particularly impressive

when one keeps in mind the tremendous compaction achieved in the description of the

influence functions over extremely large continuous local state spaces. Other than the

accuracy of MKS, the computational efficiency of MKS should also be emphasized. The

FEM prediction of the microstructure in Figure 7(a) took 24 seconds with 2 processors

(each 3.0 GHz) on a supercomputer, while prediction with MKS took only 2 seconds with

only 1 processor (3.0 GHz) on a standard desktop computer.
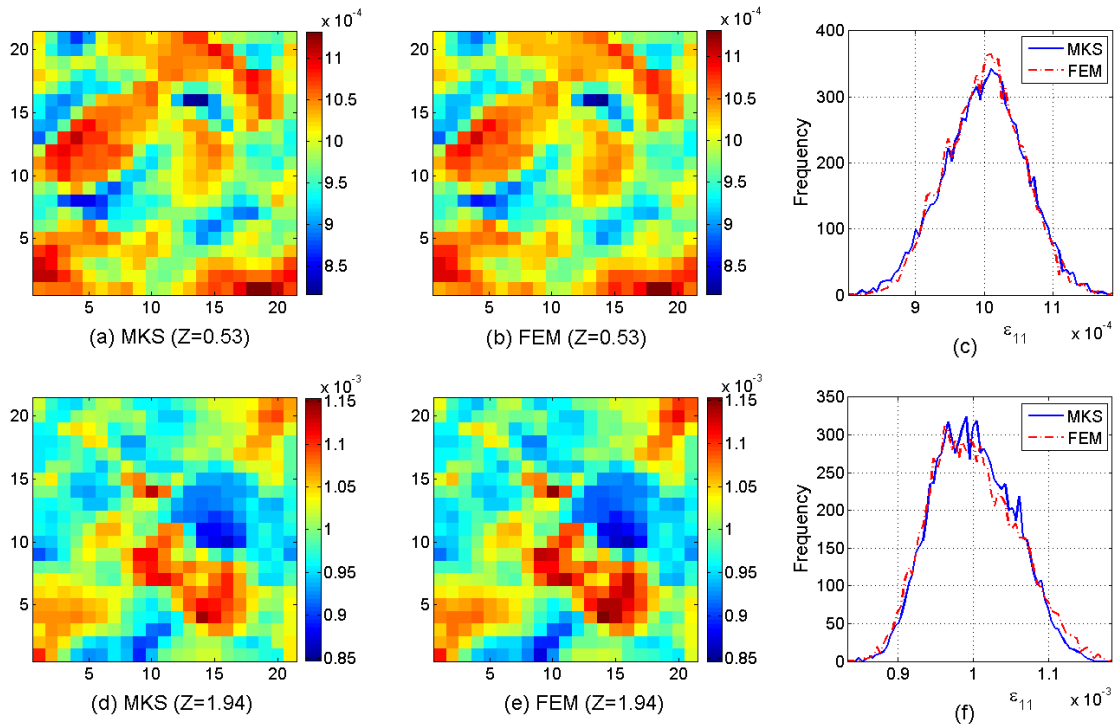
Figure 27: Comparison of MKS and FEM predictions for moderate levels of cubic elastic anisotropy included in this study. (a) and (b) shows the strain field distributions predicted by the MKS and FEM approaches on a middle slice of a MVE with an anisotropy ratio of $Z = 1.94$. (c) is the frequency plot of the strains from the same predictions. (d), (e), and (f) repeat the comparisons for a MVE with a cubic anisotropy ratio of $Z = 0.54$

The influence functions are analogous to Green's functions and show a decaying

characteristic with increasing size of t vector. It was previously shown that the influence

functions obtained from smaller domains can be extended to larger domains by padding

with zeros [18-20, 25]. This is done to facilitate the applications of the influence functions

to arbitrary-sized MVEs (or RVEs) without much additional work (i.e., without the need to recalibrate the localization linkages). In an effort to demonstrate the scalability of influence functions, the Fourier coefficients of the influence functions obtained from the $21 \times 21 \times 21$ domain are extended to the larger domain of $45 \times 45 \times 45$ by zero-padding. For validation of the scalability of influence functions for cubic polycrystalline aggregates, a $45 \times 45 \times 45$ equiaxed microstructure with 1257 distinct orientations from the entire cubic-triclinic FZ was generated. Assigning a set of cubic elastic stiffness parameters with $Z = 1.32$ to the microstructure, the FEM and MKS predictions were obtained and shown in Figure 28. There is an excellent agreement between the MKS and FEM predictions, attesting the scalability of the influence functions established in MKS framework. It should be noted that the computational efficiency is much more impressive with larger size microstructures. FEM simulation of $45 \times 45 \times 45$ microstructure took 3 minutes with 16 processors (each 3.0 GHz) on a supercomputer, while MKS prediction took only 24 seconds with only 1 processor (3.0 GHz) on a standard computer.
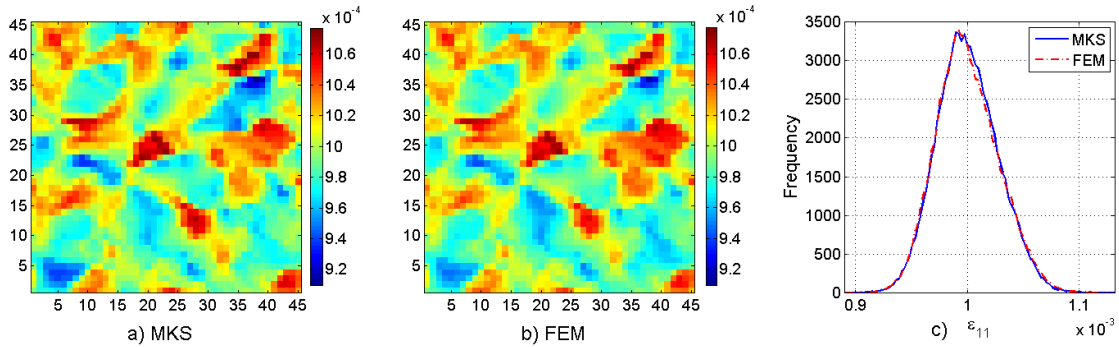
Figure 28: Comparison of the strain field ε_{11} for a middle slice predicted with (a) MKS and (b) FEM approaches for a $\mathbf{45 \times 45 \times 45}$ MVE with a cubic anisotropy factor of $\mathbf{Z = 1.32}$. (c) Comparison of the MKS and FEM strain predictions presented as frequency plots. Red dashed line shows the distribution of strain from FEM results, while the blue solid line shows the distribution of strain from MKS predictions

In this new MKS framework for a family of single phase cubic polycrystalline aggregates, it is once again observed that the first set of terms are adequate in predicting the response field of interest for low to moderate contrast material systems. However from our previous experiences [18], it is crucial that the higher order terms are included in the local state description for higher anisotropy levels (produces higher contrast). Especially in applications where higher accuracy in prediction of response field is required on the spatial locations where failure is likely to occur (high cycle fatigue, etc.), the higher order terms along with much more sophisticated error measures will be required.

CHAPTER 6

LOCALIZATION RELATIONSHIPS FOR MULTIPHASE

POLYCRYSTALLINE MATERIALS

As a last case study, MKS framework is extended to multiphase polycrystalline material. Multiphase polycrystalline material can be considered as a material system with more than one phase, where each phase is heterogeneous within itself due to crystal lattice orientation. In multiphase polycrystals, contrast between the microscale constituents is described by the elastic stiffness constants and crystal lattice orientation. The localization relationships on a continuous local state space can be written as:

$$\boldsymbol{p}_s = \sum_L \sum_t \frac{\Delta}{N_L} \boldsymbol{A}_t^L M_{s+t}^L = \sum_t \sum_c \int_{FZ_c} \boldsymbol{\alpha}_t^c(g) f_{s+t}^c(g) dg \tag{142}$$

where $c = 1, 2, \dots, C$ enumerates the material phase in the volume. $\alpha_t^c(g)$ and $f_{s+t}^c(g)$ are influence functions and orientation distribution functions for material phase c respectively. As stated in Chapter 4 and 5, the numerical evaluation of integral in Eq. (142) is now even more difficult than its analogue for the single phase polycrystalline aggregates [20, 27], if one considers the primitive binning of fundamental zones of all crystal systems defined in the localization relationships. The computations in Eq. (142) are better addressed with Generalized Spherical Harmonics (GSH) functions [73]. The influence functions, $\alpha_t^c(g)$ and the orientation distribution function, $f_{s+t}^c(g)$ can be defined with GSH functions as:

$$f_s^c(g) = \sum_L F_s^{L_c} \dot{T}^{L_c}(g) \tag{143}$$

$$\boldsymbol{\alpha}_t^c(g) = \sum_{L_c} A_t^{L_c} \dot{T}^{L_c}(g) \tag{144}$$

where L_c enumerates each distinct combination of (μ_c, n_c, l_c) in GSH series expansion of the material system c in multiphase polycrystalline microstructure. Same approach used in derivation of localization series can be followed here as well. If we plug Eq. (143) and (144) in Eq. (142), the new MKS series expansion can be reformulated as:

$$\boldsymbol{p}_s = \sum_t \sum_c \sum_{L_c} \frac{1}{(2l_c + 1)} \boldsymbol{A}_t^{L_c} M_{s+t}^{L_c*} \tag{145}$$

This new formulation does not only capture the interactions between the different crystal lattice orientations of the same material phase but also captures the interactions between the crystal lattice orientations of constituent material phases of multiphase polycrystalline aggregate. In other words, MKS linkages obtained from localization relationships in Eq. (145) provides the ability to predict the response field of microstructure with multiple material systems as well as the microstructures with single material system defined in the localization relationship. It should also be recalled that the calibration of MKS linkages is a one-time computational cost and the linkages obtained from this calibration can be utilized for any microstructure with any number of material systems defined in the localization relationships with minimum computational effort.

To clarify the advantage of casting the localization relationships in Fourier basis, the localization relationships in Eq. (145) can be further simplified as:

$$p_s = \sum_t \sum_L \frac{1}{(2l_c + 1)} A_t^L M_{s+t}^{L*} \qquad (146)$$

where L enumerates the terms in GSH expansions for constituent phases in the multiphase polycrystalline aggregate. In previous case studies [17, 20], it was shown that only the terms corresponding up to $l = 4$ in the spectral representation of influence functions had significant effect on the accuracy of MKS. For example, if a multiphase polycrystal consists of two material systems with cubic-triclinic and hexagonal-triclinic symmetries, the expected number of Fourier coefficients for the spectral representation of the MKS linkages is only $L = 25$ ($L = 1,2, \dots ,25$ consists of $L_c = 1, \dots ,10$ which results from $l = 0,4$ for cubic-triclinic and $L_c = 1, \dots ,15$ which results from $l = 0,2,4$ for hexagonal-triclinic). The compact representation of functions in orientation space through GSH becomes even more significant in terms of computational efficiency when one considers the abovementioned case of multiphase polycrystals. It is reminded here that the reduction in the representation of the functions is a result of employing GSH functions in the localization relationships.

For the demonstration of MKS approach for low contrast multiphase polycrystalline aggregates, α-β-Ti material system is used. 300 random microstructures [20] with volume fractions of β phase ranging from 0 to 100% were generated for calibration. For validation of localization linkages, a set of 600 equiaxed polycrystalline microstructures were generated and the grains are randomly assigned to be α or β phase in such a way that the entire ensemble had datasets with α phase volume fraction ranging from approximately 0 to approximately 100 percent. In Figure 29, the results of MASE for both validation and calibration data sets can be seen. The entire ensemble is divided into

10 bins for α phase volume fractions. The red part of each bin shows the distribution of average error for the validation datasets falling into that volume fraction bin of α phase, while the blue part shows the distribution of average error for the corresponding calibration datasets. It can be seen that localization linkages calibrated to physics based models can accurately predict the elastic response fields of multiphase polycrystalline aggregates with any volume fraction of constituent phases and arbitrary orientation distributions.
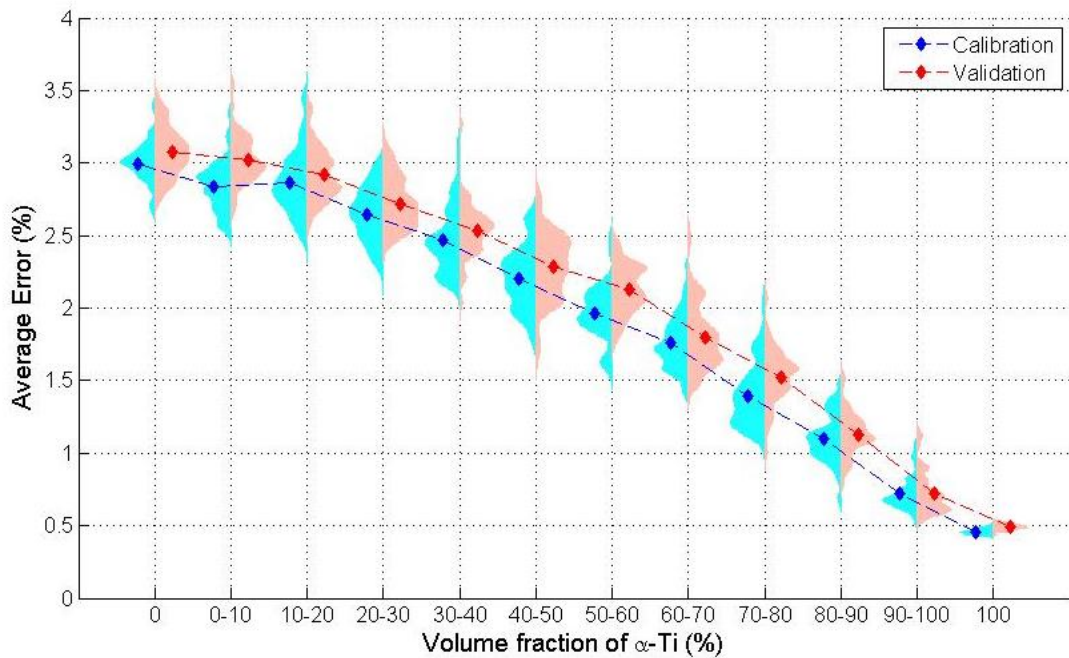
Figure 29: Violin plot of average error in calibration and validation datasets for different α phase volume fractions

Figure 30 presents the case study for demonstrating the predictive capability of the MKS approach for an MVE with a grid size of $21 \times 21 \times 21$. In part (a) shown the distribution of different grain which are colored distinctly (i.e. each color represents a distinct crystal lattice orientation). In part (b) is shown the distribution of α (black color) and β (white color) phases in the MVE. The frequency plot shown in part (c) has two distributions. The distribution shown with dashed lines are for β phase, while the

distribution with solid lines are for α phase. We can see that the strain distributions of both phases have a very good match between MKS (blue color) and FEM (red color) predictions. The same argument can also be made about comparisons at voxel level shown in parts (d) and (e). It is seen that the MKS approach provides excellent predictive capabilities for low contrast multiphase polycrystalline aggregates. The computational efficiency of MKS should be noted. The FEM prediction took 26 seconds with 2 processors (each 3.0 GHz) on a supercomputer, while MKS prediction of the same microstructure took only 2 seconds with only 1 processor (3.0 GHz) on a standard desktop computer.
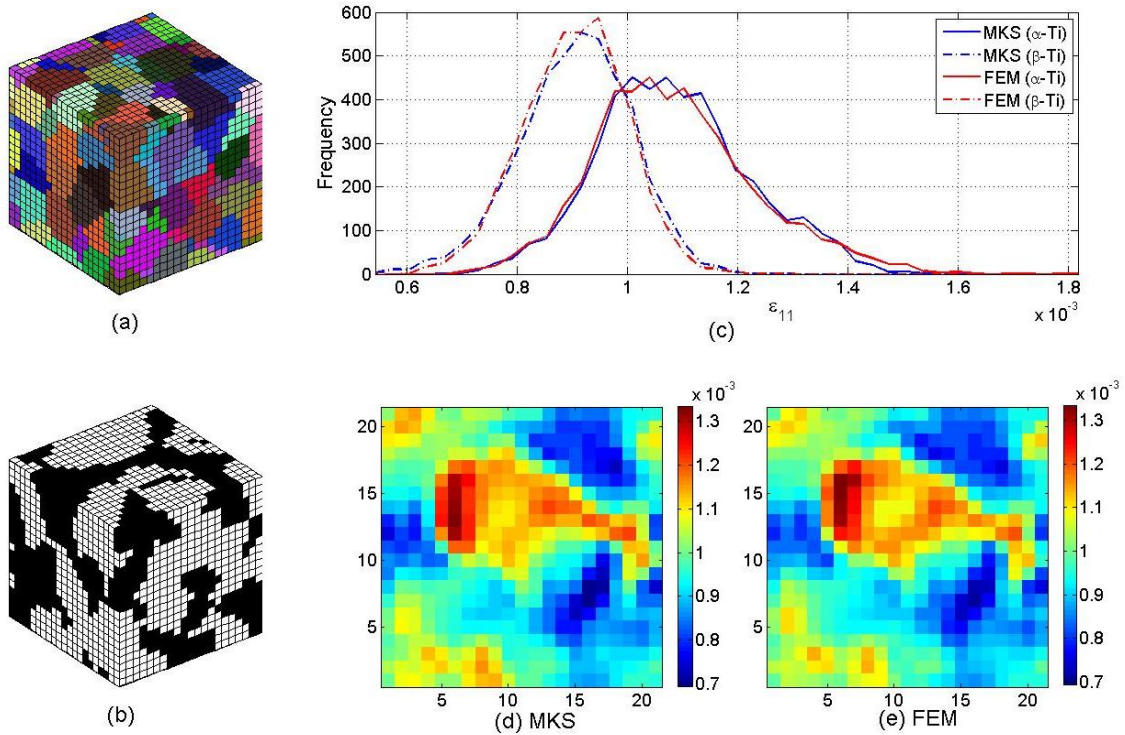
Figure 30: Comparison of strain fields predicted with MKS and FEM approaches for low contrast multiphase polycrystal α-β-Ti. (a) $21 \times 21 \times 21$ microstructure with each color representing a distinct orientation selected from the cubic and hexagonal fundamental zones randomly. (b) Distribution of α and β phases where black color represents α phase. (c) Red and blue lines show the distribution of strain field in FEM and MKS respectively (d) and (e) are the middle slices of strain fields predicted by MKS and FEM approaches, respectively

CHAPTER 7

CONCLUSIONS

In this dissertation, three main advancements were implemented in the localization part of hierarchical multiscale modeling. In prior work of MKS, the local microstructure was described with finite number of local states (i.e. two or three finite discrete local states). The discrete binning of the local state space is not a computationally efficient way of establishing localization linkages. MKS formulation developed in prior work would not be feasible for both discrete and continuous local state spaces (i.e. crystal lattice orientation for polycrystalline materials). First advancement is the formulation of a new generalized MKS framework for localization relationships. This new formulation was based on Fourier representations of the local microstructure descriptor and influence functions that constitute MKS. It was shown that the new generalized MKS framework is very versatile and flexible that it can be extended to any number of phases with complex tensorial local states as well as discrete local state spaces used in prior work. This argument was proven with 3 case studies where the generalized framework was extended to single phase polycrystalline material systems, a broad class of single phase polycrystalline systems and multiphase polycrystalline systems.

The second important advancement is the compact representation of the local microstructure descriptor through Fourier basis functions. The main local state we were interested in this dissertation was crystal lattice orientation. As mentioned before, the number of local states that were handled in prior MKS framework included only two or

three finite discrete local states. The local state space for a polycrystalline material is the fundamental zone (FZ) that contains all unique crystal lattice orientations. Since each orientation that we can extract from FZ results in a different material property in sample frame, the number of discrete local states that can be defined in this local state space is essentially infinite. Hence, a novel, compact and accurate representation of the functions that are defined in the crystal orientation space was required. For this manner, GSH functions were employed for the inclusion of crystal lattice orientation in the new generalized MKS framework. GSH functions form an orthonormal basis in the FZ of the crystal system selected and it was shown that the continuous crystal orientations space can be included in MKS formulation with more compact forms than we can with binning it. The physics phenomena we were interested in was linear elastic deformation. It was found out that the number of coefficients that were required to represent the local microstructure and influence functions were reduced to only 10 and 15 for cubic and hexagonal materials, respectively, by employing GSH basis functions. This was a dramatic reduction from possibly hundreds of discrete local states if we preferred to discretize FZ for the selected crystal system.

The third and most important advancement was in the computational efficiency achieved for the prediction of local response field for the linear elastic deformation of material systems presented in this dissertation. As mentioned before, the FEM has a complexity of S^3, while DFT operation has a complexity of $S \log S$. The gains in computational efficiency in MKS are due to the convolution property of DFT operation. Since each term in MKS expansion is a convolution of local microstructure descriptor and influence function, it takes only a few seconds to predict the local response in DFT space.

The computational gains are even more significant as the size of the RVE gets larger. MKS predicts the response field of a selected RVE often times several order magnitudes faster than FEM. This is especially crucial when the number of RVEs to be evaluated for their local response field.

CHAPTER 8

FUTURE WORK

Even though the versatility and flexibility of MKS approach to localization relationships have been proven with both prior work and the case studies in this dissertation, there are some certain aspects of MKS that has to be explored to make the approach more desirable from many different disciplines of science.

The selection of calibration MVEs play an important role in the performance of localization linkages. In prior work, it was shown that two delta microstructures for a two-phase material system was adequate to obtain high accuracy in the prediction of local fields. However, the number of possible delta microstructures that we can generate for polycrystalline aggregates is essentially infinite. Hence, the calibration MVEs were assigned crystal lattice orientations randomly to the spatial voxels based on the topology. For instance, the MVEs with equiaxed topology have orientations assigned to the same color spatial voxels randomly. Indeed, not every combination of two orientations have the same contrast. Some combination of orientations (or some textures) have more observations in the ensemble than others. Even though this definitely affects the performance of localization linkages, the effects were negligible for the low to moderate contrast polycrystalline material systems studied in this dissertation. However, for high contrast material systems, a strategy that involves a more systematic calibration MVE generation should be developed to cover all different contrasts resulting from different crystal lattice orientations.

In this dissertation, only the first order terms in the MKS series expansion were employed to predict the response field of polycrystalline materials with low to moderate contrasts. Since the focus on this dissertation was on extending the MKS approach to material systems with complex local states by using compact Fourier representations, the higher order terms were not included in the analysis. However, higher order terms are essential for the prediction of local response fields of material systems with higher contrast. The contrast is actually more significant in multiphase polycrystalline material systems. The α-β Ti system studied in Chapter 6 had low contrast between its microscale constituents. However, for multiphase polycrystalline material systems, contrast is defined by both the crystal lattice orientation and the magnitudes of the elastic stiffness constants. Hence, the higher order terms need to be employed for high contrast multiphase polycrystalline material systems.

The phenomena explored in this dissertation was linear elastic deformation. The linkages that are developed here can be used in applications where elastic deformations carry utmost importance. One important example is the high cycle fatigue, where the deformations are mostly elastic (or very small plastic strains). High cycle fatigue testing usually involves very large number of cycles (usually 10^4 or more). The simulations that require to simulate this kind of testing might need to solve elastic governing field equations. This would require incredible amount of computational effort due to the nature of high cycle fatigue testing. Data-driven MKS approach would decrease the computational requirements dramatically based on the performance of linkages for elastic deformation of polycrystalline materials shown in the case studies of this dissertation.

APPENDIX

This dissertation is heavily based on two journal articles published in Acta Materialia in December 2014 and August 2015. Several paragraphs, excerpts and figures have been copied from these publications with permissions obtained from the publisher to use specifically in this dissertation. URL links to the publications in publisher's website and the copyright licenses obtained from the publisher are given below.

Yabansu, Y.C., D.K. Patel, and S.R. Kalidindi, *Calibrated localization relationships for elastic response of polycrystalline aggregates.* Acta Materialia, 2014. **81**: p. 151-160.

http://www.sciencedirect.com/science/article/pii/S1359645414006235

License Number	4045531316695
Licensed Content Publisher	Elsevier
Licensed Content Publication	Acta Materialia
Licensed Content Title	Calibrated localization relationships for elastic response of polycrystalline aggregates
Licensed Content Author	Yuksel C. Yabansu,Dipen K. Patel,Surya R. Kalidindi
Licensed Content Date	December 2014
Licensed Content Volume	81
Licensed Content Issue	n/a
Licensed Content Pages	10
Start Page	151
End Page	160
Type of Use	reuse in a thesis/dissertation
Portion	full article
Format	electronic
Title of your thesis/dissertation	Calibrated Localization Relationships For Elastic Polycrystalline Aggregates
Expected completion date	May 2017

Yabansu, Y.C. and S.R. Kalidindi, *Representation and calibration of elastic localization kernels for a broad class of cubic polycrystals.* Acta Materialia, 2015. **94**: p. 26-35.

http://www.sciencedirect.com/science/article/pii/S1359645415003018

REFERENCES

1. OSTP, *Materials genome initiative for global competitiveness*, in *National Science and Technology Council OSTP. Washington, USA*. 2011.

2. Engineering, N.R.C.C.o.I.C.M., *Integrated computational materials engineering: a transformational discipline for improved competitiveness and national security*. 2008: National Academies Press.

3. Kalidindi, S.R., *Hierarchical Materials Informatics: Novel Analytics for Materials Data*. 2015: Elsevier.

4. Olson, G.B., *Computational design of hierarchically structured materials.* Science, 1997. **277**(5330): p. 1237-1242.

5. Steinmetz, P., Y.C. Yabansu, J. Hötzer, M. Jainta, B. Nestler, and S.R. Kalidindi, *Analytics for microstructure datasets produced by phase-field simulations.* Acta Materialia, 2016. **103**: p. 192-203.

6. Choudhury, A., Y.C. Yabansu, S.R. Kalidindi, and A. Dennstedt, *Quantification and classification of microstructures in ternary eutectic alloys using 2-point spatial correlations and principal component analyses.* Acta Materialia, 2016. **110**: p. 131-141.

7. Yabansu, Y.C., P. Steinmetz, J. Hötzer, S.R. Kalidindi, and B. Nestler, *Extraction of reduced-order process-structure linkages from phase-field simulations.* Acta Materialia, 2017. **124**: p. 182-194.

8. Choi, H., D.L. McDowell, J.K. Allen, D. Rosen, and F. Mistree, *An inductive design exploration method for robust multiscale materials design.* Journal of Mechanical Design, 2008. **130**(3): p. 031402.

9. McDowell, D.L., J. Panchal, H.-J. Choi, C. Seepersad, J. Allen, and F. Mistree, *Integrated design of multiscale, multifunctional materials and products*. 2009: Butterworth-Heinemann.

10. Panchal, J.H., S.R. Kalidindi, and D.L. McDowell, *Key computational modeling issues in integrated computational materials engineering.* Computer-Aided Design, 2013. **45**(1): p. 4-25.

11. Fullwood, D.T., S.R. Niezgoda, B.L. Adams, and S.R. Kalidindi, *Microstructure sensitive design for performance optimization.* Progress in Materials Science, 2010. **55**(6): p. 477-562.

12. Luscher, D.J., D.L. McDowell, and C.A. Bronkhorst, *A second gradient theoretical framework for hierarchical multiscale modeling of materials.* International Journal of Plasticity, 2010. **26**(8): p. 1248-1275.

13. Cruzado, A., B. Gan, M. Jiménez, D. Barba, K. Ostolaza, A. Linaza, J. Molina-Aldareguia, J. Llorca, and J. Segurado, *Multiscale modeling of the mechanical behavior*

of IN718 superalloy based on micropillar compression and computational homogenization. Acta Materialia, 2015. **98**: p. 242-253.

14. Nguyen, S., A. Tran-Le, M. Vu, Q. To, O. Douzane, and T. Langlet, *Modeling thermal conductivity of hemp insulation material: A multi-scale homogenization approach.* Building and Environment, 2016. **107**: p. 127-134.

15. Zhou, X.Y., P.D. Gosling, C.J. Pearce, Z. Ullah, and L. Kaczmarczyk, *Perturbation-based stochastic multi-scale computational homogenization method for woven textile composites.* International Journal of Solids and Structures, 2016. **80**: p. 368-380.

16. Guo, N. and J. Zhao, *3D multiscale modeling of strain localization in granular media.* Computers and Geotechnics, 2016.

17. Yabansu, Y.C. and S.R. Kalidindi, *Representation and calibration of elastic localization kernels for a broad class of cubic polycrystals.* Acta Materialia, 2015. **94**: p. 26-35.

18. Fast, T. and S.R. Kalidindi, *Formulation and calibration of higher-order elastic localization relationships using the MKS approach.* Acta Materialia, 2011. **59**(11): p. 4595-4605.

19. Fast, T., S.R. Niezgoda, and S.R. Kalidindi, *A new framework for computationally efficient structure–structure evolution linkages to facilitate high-fidelity scale bridging in multi-scale materials models.* Acta Materialia, 2011. **59**(2): p. 699-707.

20. Yabansu, Y.C., D.K. Patel, and S.R. Kalidindi, *Calibrated localization relationships for elastic response of polycrystalline aggregates.* Acta Materialia, 2014. **81**: p. 151-160.

21. Liu, R., Y.C. Yabansu, A. Agrawal, S.R. Kalidindi, and A.N. Choudhary, *Machine learning approaches for elastic localization linkages in high-contrast composite materials.* Integrating Materials and Manufacturing Innovation, 2015. **4**(1): p. 1.

22. Al-Harbi, H.F., G. Landi, and S.R. Kalidindi, *Multi-scale modeling of the elastic response of a structural component made from a composite material using the materials knowledge system.* Modelling and Simulation in Materials Science and Engineering, 2012. **20**(5): p. 055001.

23. Kalidindi, S.R., S.R. Niezgoda, G. Landi, S. Vachhani, and T. Fast, *A novel framework for building materials knowledge systems.* Computers, Materials, & Continua, 2010. **17**(2): p. 103-125.

24. Landi, G. and S.R. Kalidindi, *Thermo-elastic localization relationships for multi-phase composites.* Computers, Materials, & Continua, 2010. **16**(3): p. 273-293.

25. Landi, G., S.R. Niezgoda, and S.R. Kalidindi, *Multi-scale modeling of elastic response of three-dimensional voxel-based microstructure datasets using novel DFT-based knowledge systems.* Acta Materialia, 2010. **58**(7): p. 2716-2725.

26. Niezgoda, S.R., Y.C. Yabansu, and S.R. Kalidindi, *Understanding and visualizing microstructure and microstructure variance as a stochastic process.* Acta Materialia, 2011. **59**(16): p. 6387-6400.

27. Kalidindi, S.R., *Computationally Efficient, Fully Coupled Multiscale Modeling of Materials Phenomena Using Calibrated Localization Linkages.* ISRN Materials Science, 2012. **2012**: p. 13.

28. Kröner, E., *Statistical Modelling*, in *Modelling Small Deformations of Polycrystals*, J. Gittus and J. Zarka, Editors. 1986, Springer Netherlands. p. 229-291.

29. Kröner, E., *Bounds for effective elastic moduli of disordered materials.* Journal of the Mechanics and Physics of Solids, 1977. **25**(2): p. 137-155.

30. Kalidindi, S.R., H.K. Duvvuru, and M. Knezevic, *Spectral calibration of crystal plasticity models.* Acta Materialia, 2006. **54**(7): p. 1795-1804.

31. Proust, G. and S.R. Kalidindi, *Procedures for construction of anisotropic elastic–plastic property closures for face-centered cubic polycrystals using first-order bounding relations.* Journal of the Mechanics and Physics of Solids, 2006. **54**(8): p. 1744-1762.

32. Knezevic, M. and S.R. Kalidindi, *Fast computation of first-order elastic-plastic closures for polycrystalline cubic-orthorhombic microstructures.* Computational Materials Science, 2007. **39**(3): p. 643-648.

33. Shaffer, J.B., M. Knezevic, and S.R. Kalidindi, *Building texture evolution networks for deformation processing of polycrystalline fcc metals using spectral approaches: Applications to process design for targeted performance.* International Journal of Plasticity, 2010. **26**(8): p. 1183-1194.

34. Bunge, H.J. and H.R. Wenk, *Three-dimensional texture analysis of three quartzites (trigonal crystal and triclinic specimen symmetry).* Tectonophysics, 1977. **40**(3–4): p. 257-285.

35. Field, D.P. and B.L. Adams, *Interface cavitation damage in polycrystalline copper.* Acta Metallurgica et Materialia, 1992. **40**(6): p. 1145-1157.

36. Inoue, H., N. Miwa, and N. Inakazu, *Texture and shape memory strain in TiNi alloy sheets.* Acta Materialia, 1996. **44**(12): p. 4825-4834.

37. Li, D.S., H. Garmestani, and B.L. Adams, *A texture evolution model in cubic-orthotropic polycrystalline system.* International Journal of Plasticity, 2005. **21**(8): p. 1591-1617.

38. Morris, P.R., *Elastic constants of polycrystals.* International Journal of Engineering Science, 1970. **8**(1): p. 49-61.

39. Sayers, C.M., *The elastic anisotropy of polycrystalline aggregates of zirconium and its alloys.* Journal of Nuclear Materials, 1987. **144**(3): p. 211-213.

40. Adams, B.L., S.R. Kalidindi, and D.T. Fullwood, *Microstructure Sensitive Design for Performance Optimization*. 2012: Elsevier Science.

41. Houskamp, J.R., G. Proust, and S.R. Kalidindi, *Integration of microstructure-sensitive design with finite element methods: Elastic-plastic case studies in FCC polycrystals.* International Journal for Multiscale Computational Engineering, 2007. **5**(3-4): p. 261-272.

42. Kalidindi, S.R., J.R. Houskamp, M. Lyons, and B.L. Adams, *Microstructure sensitive design of an orthotropic plate subjected to tensile load.* International Journal of Plasticity, 2004. **20**(8–9): p. 1561-1575.

43. Fast, T., M. Knezevic, and S.R. Kalidindi, *Application of microstructure sensitive design to structural components produced from hexagonal polycrystalline metals.* Computational Materials Science, 2008. **43**(2): p. 374-383.

44. Wu, X., G. Proust, M. Knezevic, and S.R. Kalidindi, *Elastic–plastic property closures for hexagonal close-packed polycrystalline metals using first-order bounding theories.* Acta Materialia, 2007. **55**(8): p. 2729-2737.

45. Arfken, G.B., *Mathematical methods for physicists*. 2013: Academic press.

46. Bishop, C.M., *Pattern recognition and machine learning*. Vol. 1. 2006: springer New York.

47. Friedman, J., T. Hastie, and R. Tibshirani, *The elements of statistical learning*. Vol. 1. 2001: Springer series in statistics Springer, Berlin.

48. Rabiner, L.R. and B. Gold, *Theory and application of digital signal processing.* Englewood Cliffs, NJ, Prentice-Hall, Inc., 1975. 777 p., 1975. **1**.

49. Kreyszig, E. and E.J. Norminton, *Advanced engineering mathematics*. Vol. 1002. 1993: Wiley New York etc.

50. Montgomery, D.C. and G.C. Runger, *Applied statistics and probability for engineers*. 2010: John Wiley & Sons.

51. Bertsekas, D.P., *Constrained optimization and Lagrange multiplier methods*. 2014: Academic press.

52. Bates, D.M. and D.G. Watts, *Nonlinear regression: iterative estimation and linear approximations*. 1988: Wiley Online Library.

53. Torquato, S., *Effective stiffness tensor of composite media—I. Exact series expansions.* Journal of the Mechanics and Physics of Solids, 1997. **45**(9): p. 1421-1448.

54. Torquato, S., *Random heterogeneous materials: microstructure and macroscopic properties*. Vol. 16. 2002: Springer.

55. Shou, W., D. Yi, H. Liu, C. Tang, F. Shen, and B. Wang, *Effect of grain size on the fatigue crack growth behavior of 2524-T3 aluminum alloy.* Archives of Civil and Mechanical Engineering, 2016. **16**(3): p. 304-312.

56. Sanei, S.H.R. and R.S. Fertig, *Uncorrelated volume element for stochastic modeling of microstructures based on local fiber volume fraction variation.* Composites Science and Technology, 2015. **117**: p. 191-198.

57. Tewari, A. and A. Gokhale, *Nearest-neighbor distributions in thin films, sheets, and plates.* Acta materialia, 2006. **54**(7): p. 1957-1963.

58. Adams, B.L. and T. Olson, *The mesostructure—properties linkage in polycrystals.* Progress in Materials Science, 1998. **43**(1): p. 1-87.

59. Beran, M., T. Mason, B. Adams, and T. Olsen, *Bounding elastic constants of an orthotropic polycrystal using measurements of the microstructure.* Journal of the Mechanics and Physics of Solids, 1996. **44**(9): p. 1543-1563.

60. Milton, G.W., *The theory of composites.* Vol. 6. 2002: Cambridge University Press.

61. Beran, M.J. and A. Pytte, *Statistical continuum theories.* American Journal of Physics, 1968. **36**(10): p. 923-923.

62. Michel, J., H. Moulinec, and P. Suquet, *Effective properties of composite materials with periodic microstructure: a computational approach.* Computer methods in applied mechanics and engineering, 1999. **172**(1): p. 109-143.

63. Moulinec, H. and P. Suquet, *A numerical method for computing the overall response of nonlinear composites with complex microstructure.* Computer methods in applied mechanics and engineering, 1998. **157**(1): p. 69-94.

64. Lin, S. and H. Garmestani, *Statistical continuum mechanics analysis of an elastic two-isotropic-phase composite material.* Composites Part B: Engineering, 2000. **31**(1): p. 39-46.

65. Garmestani, H., S. Lin, B. Adams, and S. Ahzi, *Statistical continuum theory for large plastic deformation of polycrystalline materials.* Journal of the Mechanics and Physics of Solids, 2001. **49**(3): p. 589-607.

66. Mason, T.A. and B.L. Adams, *Use of microstructural statistics in predicting polycrystalline material properties.* Metallurgical and Materials transactions A, 1999. **30**(4): p. 969-979.

67. Michel, J., H. Moulinec, and P. Suquet, *A computational scheme for linear and non-linear composites with arbitrary phase contrast.* International Journal for Numerical Methods in Engineering, 2001. **52**(1-2): p. 139-160.

68. Song, Y.S. and J.R. Youn, *Evaluation of effective thermal conductivity for carbon nanotube/polymer composites using control volume finite element method.* Carbon, 2006. **44**(4): p. 710-717.

69. Jang, S.-H., D.P. Hochstein, S. Kawashima, and H. Yin, *Experiments and micromechanical modeling of electrical conductivity of carbon nanotube/cement composites with moisture.* Cement and Concrete Composites, 2017. **77**: p. 49-59.

70. Li, X., Y. Xu, and S. Chen, *Computational homogenization of effective permeability in three-phase mesoscale concrete.* Construction and Building Materials, 2016. **121**: p. 100-111.

71. Adams, B.L., X. Gao, and S.R. Kalidindi, *Finite approximations to the second-order properties closure in single phase polycrystals.* Acta Materialia, 2005. **53**(13): p. 3563-3577.

72. Brough, D.B., D. Wheeler, J.A. Warren, and S.R. Kalidindi, *Microstructure-based knowledge systems for capturing process-structure evolution linkages.* Current Opinion in Solid State and Materials Science, 2016.

73. Bunge, H.J., *Texture analysis in materials science: mathematical methods*. 1982: Butterworths.

74. Kalidindi, S.R., M. Binci, D. Fullwood, and B.L. Adams, *Elastic properties closures using second-order homogenization theories: Case studies in composites of two isotropic constituents.* Acta Materialia, 2006. **54**(11): p. 3117-3126.

75. Fullwood, D.T., S.R. Niezgoda, and S.R. Kalidindi, *Microstructure reconstructions from 2-point statistics using phase-recovery algorithms.* Acta Materialia, 2008. **56**(5): p. 942-948.

76. Binci, M., D. Fullwood, and S.R. Kalidindi, *A new spectral framework for establishing localization relationships for elastic behavior of composites and their calibration to finite-element models.* Acta Materialia, 2008. **56**(10): p. 2272-2282.

77. Duvvuru, H.K., X. Wu, and S.R. Kalidindi, *Calibration of elastic localization tensors to finite element models: Application to cubic polycrystals.* Computational Materials Science, 2007. **41**(2): p. 138-144.

78. Vilenkin, N.I., *Special functions and the theory of group representations*. Vol. 22. 1978: American Mathematical Soc.

79. Kalidindi, S.R., G. Landi, and D.T. Fullwood, *Spectral representation of higher-order localization relationships for elastic behavior of polycrystalline cubic materials.* Acta Materialia, 2008. **56**(15): p. 3843-3853.

80. Adams, B.L., A. Henrie, B. Henrie, M. Lyon, S.R. Kalidindi, and H. Garmestani, *Microstructure-sensitive design of a compliant beam.* Journal of the Mechanics and Physics of Solids, 2001. **49**(8): p. 1639-1663.

81. Niezgoda, S., A. Kanjarla, and S. Kalidindi, *Novel microstructure quantification framework for databasing, visualization, and analysis of microstructure data.* Integrating Materials and Manufacturing Innovation, 2013. **2**(1): p. 1-27.

82. Hibbit, Karlsson, and Sorensen, *ABAQUS/Standard Analysis User's Manual*. 2007: Hibbit, Karlsson, Sorensen Inc.

83. Meyers, M.A. and K.K. Chawla, *Mechanical Behavior of Materials*. 2009: Cambridge University Press.

84. Welsch, G., R. Boyer, and E.W. Collings, *Materials Properties Handbook: Titanium Alloys*. 1993: ASM International.

85. Hastie, T., R. Tibshirani, and J.J.H. Friedman, *The elements of statistical learning*. Vol. 1. 2001: Springer New York.

86. Proust, G. and S.R. Kalidindi, *Procedures for construction of anisotropic elastic-plastic property closures for face-centered cubic polycrystals using first-order bounding relations.* Journal of the Mechanics and Physics of Solids, 2006. **54**(8): p. 1744-1762.